Ph.D. in Bioengineering, Cycle XXXI

Final Dissertation

Fluorescent transcription factors as tools to evaluate the influence of mechanical stimuli on nuclear import

Lucia Boeri

Advisor:
Prof. Manuela Teresa Raimondi

Co-Advisors:
Dr. Diego Albani
Dr. Emanuela Jacchetti

Coordinator of the Research Doctorate Course:
Prof. Andrea Aliverti

Tutor:
Prof. Sara Mantero

2015 - 2018

“The wise man doesn’t give the right answers,
he poses the right questions.”
Claude Levi-Strauss

Table of Contents

List of abbreviations

2D	Two-dimensional
3D	Three-dimensional
CKM	Creatine Kinase, M-type
ECM	Extra Cellular Matrix
EGFP	Enhanced Green Fluorescent Protein
Em	Emission wavelength
Ex	Excitation wavelength
FP	Fluorescent Proteins
FRAP	Fluorescence Recovery After Photobleaching
GFP	Green Fluorescent Protein
MD	Molecular Dynamics
MSCs	Mesenchymal Stem Cells
Myog	Myogenin
NE	Nuclear Envelope
NPC	Nuclear Pore Complex
PTD	Protein Transduction Domain
TF	Transcription Factor
YFP	Yellow Fluorescent Protein

Abstract

Mesenchymal stem cell (MSCs)-based therapy is a promising strategy to regenerate injured tissues and regulate immune responses. The challenges concerning the clinical application of MSCs injection are mainly related to the reduced post-transplantation cell survival and the low control of MSC fate. Recent advancements focused on MSC response by studying their mechanotransduction, that is the mechanism by which MSCs transduce environmental mechanical inputs into chemical signals. The NICHOID project started in 2015 with the goal to verify the hypothesis that MSC key mechanisms, such as differentiation, are regulated by stretched-dependent nuclear import of specific transcription factors. According to this hypothesis the nuclear pores are mechanically sensitive elements and respond to cell stretching with nuclear pore enlarging and increased nuclear import of transcription factors. The experimental validation of the NICHOID hypothesis is based on the nuclear import rate measurement of transcription factors able to promote MSC differentiation. The aim of my Ph.D. thesis was to engineer transcription factors to achieve fluorescent tools to allow the nuclear import rate assessment in different MSC stretching conditions.

To reach my goal, I designed, purified and validated five fluorescent transcription factor variants. The transcription factor experimentally selected was a promoter of myogenesis, MyoD (Myoblast determination protein). Five variants of MyoD were purified, each fused to a different fluorescent protein (probe): Tat-GFP, (-30)GFP, PAGFP, PAmCherry, mEOS3.2. Each variant of MyoD presented a peculiar characteristic: Tat-GFP-MyoD and (-30)GFP-MyoD followed specific protein transduction-based delivery procedures while MyoD-PAGFP, MyoD-PAmCherry and MyoD-mEos3.2 were sensible to

photoactivation or photoconversion. The validation of the fluorescent molecules required analysis of protein localization by fluorescence confocal microscopy, nucleocytoplasmic transport measurement by fluorescence recovery after photobleaching (FRAP) method and transcription promoting activity assay by real-time PCR. The results showed that the fluorescent variant of MyoD best representing the physiology of the native MyoD is the MyoD-PAGFP. (-30)GFP-MyoD resulted a suitable tool for nucleocytoplasmic transport measurement but real-time PCR results highlighted an inhibitory effect on MyoD functionality.

Key experimental evidence of the fluorescent transcription factors was deepened with computational investigations. In particular, I used molecular dynamics (MD) to assess the (-30)GFP inhibition effect observed during the transcription promoting activity analysis. I used MyoD-PAGFP as negative control in MD simulation. (-30)GFP and PAGFP 3D models were generated by homology modeling, while in the case of MyoD protein, the 3D structure of the basic helix loop helix (BHLH) DNA binding domain was the only available. The goal of MD analyses was to verify if the presence of the peculiar major negative surface charge of (-30)GFP could interact with BHLH domain of MyoD, thus altering its functionality. Considering the bias of the lacking part of the MyoD structure, I generated four different configurations by positioning the BHLH domain of MyoD in different positions in respect to the fluorescent protein, so that the interface between the two molecules was different in every simulation. When analyzing root mean square deviation (RMSD) data and non-bonded interaction energies, results showed that (-30)GFP interacted more strongly with the monomer of MyoD in comparison to PAGFP. Furthermore, structural analyses showed that the interactions between (-30)GFP and MyoD were mainly mediated by negative and positive residues, respectively.

In conclusion, in this Ph.D. thesis, I developed and assessed several potential tools for nucleocytoplasmic transport measurement. Among the fluorescent variants of MyoD, the photoactivatable MyoD-PAGFP is the tool that best resembles the properties of the native transcription factor and it is suitable for further nuclear import measurement. Otherwise, (-30)GFP-MyoD showed great properties in terms of protein delivery and nucleo-cytoplasmic shuttling. In this variant, MD simulations suggested an interference mechanism based on a strong interaction between MyoD and (-30)GFP that could explain the inhibition of MyoD activity.

Overall, my work demonstrated that, the design and the development of the fluorescent probes in an intracellular dynamics study are fundamental steps to deeply understand their possible applications.

CHAPTER 1: Introduction

This Chapter introduces mesenchymal stem cells (MSCs) as one of the main promising tools used for cell-based therapy. Thanks to their multiple features, such as differentiation potential and immune modulatory properties, they can be used for several clinical application. Unfortunately, MSC therapy still presents different challenges related to post-transplant cell death, low control of immune-modulatory effect and sporadic trans-differentiation.

All this concerns stimulated the scientists to find a way to better control and manipulate MSCs. For many decades researchers studied stemness and differentiation response regulating the MSC environment from a chemical point of view. Recent advancements changed the perspective and focused on the reproduction of the physiological mechanical environment in order to understand the influence and the importance of the mechanical component in the control of stemness and MSC functionality.

By examining the state of the art, I will deepen the effects of the external mechanical inputs starting from a cellular level to a detailed molecular stage. The aim of this deepening is to guide through the complex mechanotransduction mechanism and to introduce the NICHOID project which is the context in which my Ph.D project developed. The challenging approach considered in the NICHOID project is to use a bioengineered synthetic stem niche to study nuclear import fluxes of transcription factors. The main objective is to demonstrate that nuclear pore complexes and nuclear envelope are key mechanically-sensitive elements in MSC fate determination.

At the end of this chapter, I will conclude with the objective of my Ph.D. project that is to engineer fluorescent transcription factors in order to

achieve a suitable tool to evaluate the influence of mechanical stimuli on nuclear import rate in MSCs.

Mesenchymal stem cells: overview

MSCs are adult multipotent stem cells able to self-renew. In 2006 the International Society of Cellular Therapy (ISCT) published a position paper in which proposed three minimal criteria to define MSCs (Table 1.1) [1]. First, MSCs must adhere to plastic when maintained in standard culture condition using tissue culture flasks. Second, MSCs must express the specific surface antigens CD105, CD73 and CD90 (≥ 95% of MSC population), and additionally cells must lack expression of specific markers of hematopoietic cell lineage: CD45, CD34, CD14 or CD11b, CD79α or CD19 and HLA class II. Third MSCs must differentiate to mesodermal lineage cell types (osteoblasts, chondroblasts and adipocytes) using standard *in vitro* tissue culture-differentiating conditions. Actually, many studies demonstrated the MSC ability to differentiate into other mesodermal lineage cells (myoblasts and tenocytes) and also into cells derived from ectoderma (neurons) and endoderma (hepatocytes) [26-28].

1 Adherence to plastic in standard culture conditions		
2 Phenotype	Positive (≥ 95%) CD105 CD73 CD90	Negative (≤ 2%) CD45 CD34 CD14 or CD11b CD79a or CD19 HLA-DR
3 *In vitro* differentiation: osteoblasts, adipocytes, chondroblasts (demonstrated by staining of *in vitro* cell culture)		

Table 1.1 Summary of criteria to identify MSCs [1]

Over ten years, MSCs have been considered as suitable and promising cells for cell-based therapy applications. The reasons of this increasing interest are mainly related to their unique properties and multiple clinical benefits (Fig. 1.1).

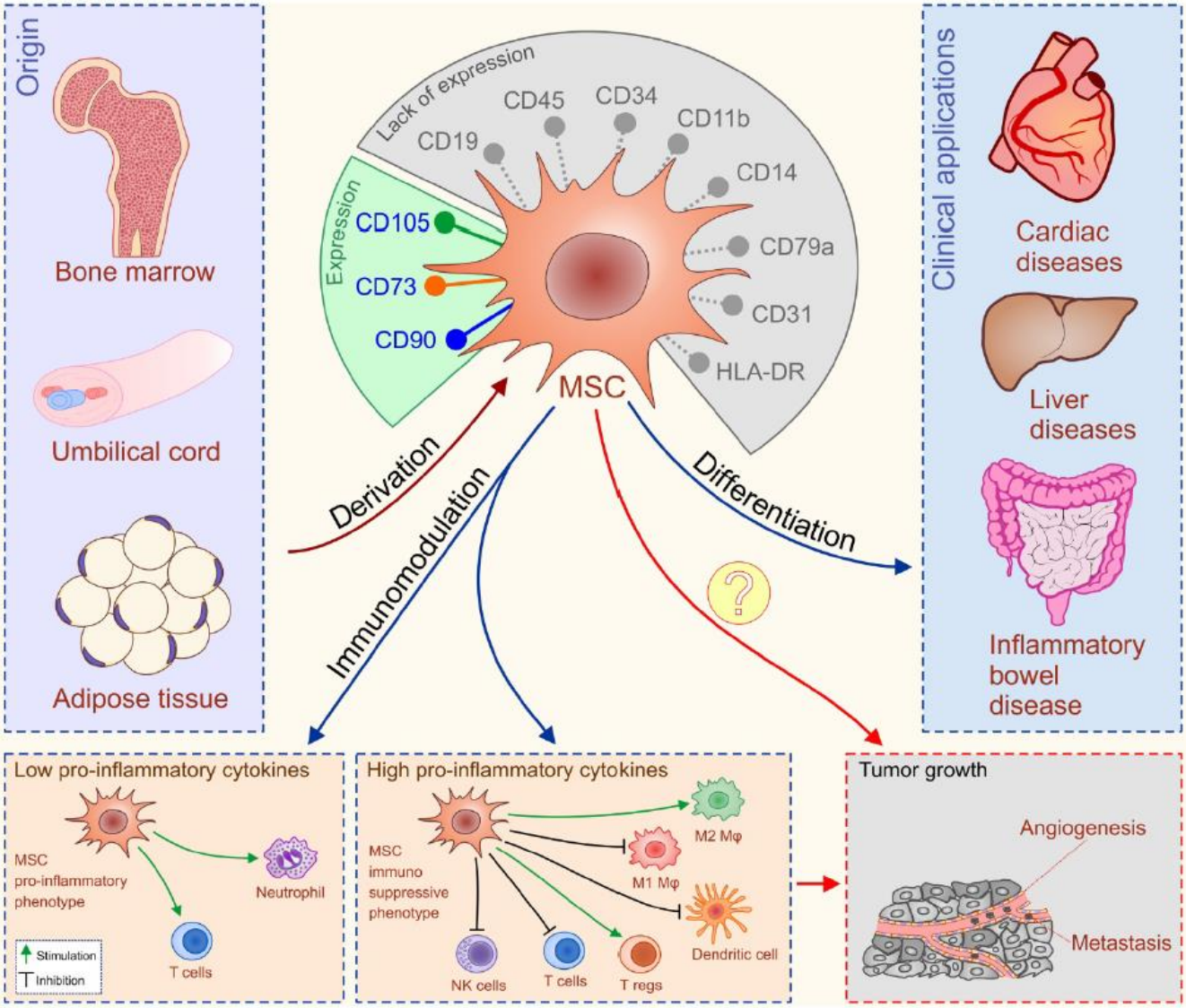

Fig. 1.1 Properties of MSCs. MSCs are mainly isolated from bone marrow, umbilical cord and adipose tissue and characterized by the expression or lack of expression of specific surface antigens. Encouraging results arouse from MSC clinical application with different pathological cases, such as inflammatory bowel disease, liver disorders and cardiac diseases. MSCs possess broad spectrum of immuno-modulatory capacities suppressing or promoting inflammation in dependence of inflammatory environment to which they are exposed to. The

undesired possible side-effects MSC-based therapy are unwanted differentiation of the transplanted MSCs and promotion of tumor growth and metastasis [3].

MSCs can be harvested from different mesenchymal tissues that are bone marrow (BM-MSCs), adipose tissue (AT-MSCs), umbilical cord (UC-MSCs) and dermis. The cell collection is a very simple procedure based on the isolation of a heterogeneous population of plastic-adherent cells screened by surface antigens expression, as ISCT defined [2]. As MSCs are adult stem cells and can be harvested from tissues, which do not involve the sacrifice of a living being, the use of MSCs in clinical trials avoids many ethical issues that otherwise raises with the clinical application of the embryonic stem cells [3]. Another advantage derived by the use of adult stem cells is that they show a low risk of tumorigenicity [4], especially compared to embryonic stem cells. In addition to the properties described above, MSCs possess broad spectrum of immune regulatory and tissue organ repairing ability. Within the innate immune system, MSCs are able to inhibit the activation of pro-inflammatory macrophages and monocytes and promote their anti-immunosuppressive function [5-6]. Considering the adaptive immune system, MSCs regulate activation and proliferation of T-cells trough cell-to-cell contact and the secretion of various soluble factors, such as prostaglandin E2 (PGE2), transforming growth factor-β (TGF-β), hepatocyte growth factor (HGF), nitric oxide (NO), indoleamine 2, 3-dioxygenase (IDO) [7-9]. Taking advantage from this immune-modulatory properties, MSCs were used for some preclinical studies of different autoimmune diseases, such as inflammatory bowel's disease (IBD) [10], systemic lupus erythematosus (SLE) [11], rheumatoid arthritis (RA) [12]. What arouse from all these cases is that MSCs showed great benefits on clinical and biochemical markers but highly dependent on the environmental inflammatory state. Due to their regenerative and tissue repairing properties, MSCs have been also

considered for cell-therapy against several other pathologies, such as myocardial infarction [13], stroke [14], liver disease [15], and pancreatitis [16].

Clinical failure and future challenges

Despite the significant progress that has been made in the development of MSC therapy for different diseases, several studies have highlighted different concerns about therapeutic efficacy. The first main problem is related to the massive transplanted MSC death caused by: (1) anoikis, due to the loss of cellular tensional integrity that is critical for anchorage-dependent cells; (2) mechanical stress of the implantation procedure; (3) low oxygen and nutrient levels of the host environment; (4) host immune response [24]. In the case of immune-mediated diseases the great limitation of MSC therapy is mainly related to the degree of inflammation showing an effective benefit just in acute inflammatory state and in presence of acute inflammatory molecules, such as INF-γ and TNF-β [17,18]. Another concerning aspect of MSC therapy is that their immune-modulatory characteristics can transform into unwanted properties when in the presence of a growing tumor [19-20]. In fact, MSCs suppress anti-tumor immune response and promote metastasis by the production of pro-angiogenic factors [21]. In addition to these concerns, another alarming issue of MSC therapy, even if more sporadic, is related to the possibility of MSCs to differentiate into an undesired tissue cell type [3, 22].

These results highlighted all the challenges that still remain in this clinical cell-application. Currently, the approaches to face these problems are mainly three: (1) the replacement of transplanted cells by their secreted factors and exosomes (secretome), avoiding all the problems about the unwanted differentiation but arising a challenge

related to the need of producing large quantities of factors and thus, MSCs [23]; (2) the manipulation of all the chemical and mechanical properties of the *ex vivo* MSC culture environment and local engraftment site in order to reduce the transplantation stress and increase cell survival [24]; (3) the use of biomaterials and 3D (three-dimensional) scaffolds to efficiently guide MSC proliferation and differentiation in *ex vivo* pre-transplantation steps [25].

Mechanical regulation of MSC differentiation

A better control and manipulation of stem cell fate represent the main challenge in MSC therapy. Until some decades ago, the only way used to guide MSC differentiation and behavior involved the addition of exogenous chemical molecules to cell culture. Recent promising strategies, instead, focused on mimicking the entire bio-chemo-mechanical environment highlighting the importance of understanding the mechanical influence of the environment on MSCs.

Cell growth, *in vitro* or *in vivo,* is clearly influenced by both matrix microenvironment (composition, stiffness, architecture) and external mechanical stimuli. Several studies demonstrated the influence of the substrate and matrix stiffness in regulating cell properties, such as proliferation, differentiation and cell shape [29]. For example (1) soft substrates, that are more similar to the mechanical properties of brain tissue, were found to be neurogenic; (2) an intermediate stiffness instead was myogenic; (3) relatively stiff substrates were found to be promoters of osteogenesis [30]. At the same way, the application of external mechanical signals reproducing the physiological mechanics to which MSCs are subjected when in the niche causes biological and structural cell rearrangements. The main external mechanical cues are resumed in figure 1.2.

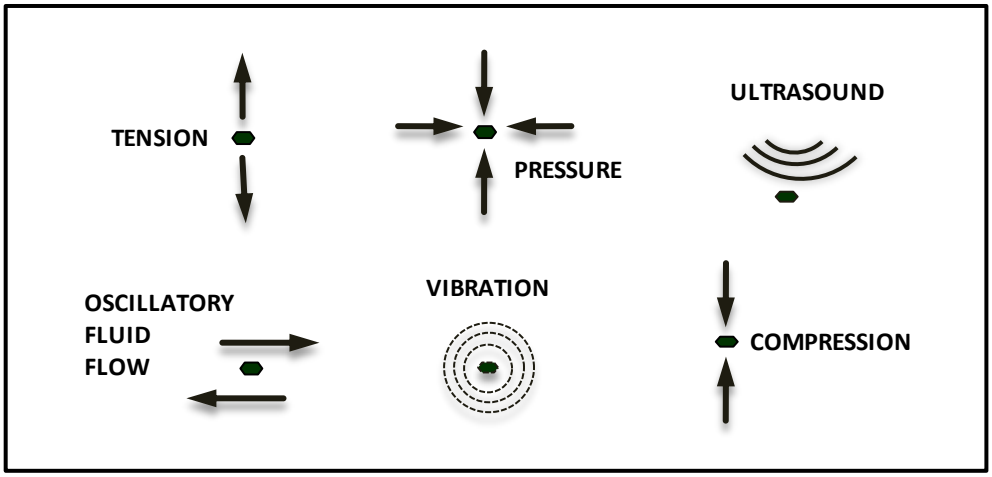

Fig. 1.2 Mechanical stimuli characterizing physiological MSC environment: hydrostatic pressure, tensile stress, fluid flow, compression, vibration, ultrasound.

Mechanical stimulation of MSCs *in vitro* has shown that, for example, tensile strain promotes osteogenesis and tenogenesis but inhibits adipogenesis, hydrostatic pressure and compressive loading induces chondrogenesis, oscillary fluid flow induces osteogenesis and myogenesis [31].

Mechanotransduction

In order to investigate the biological mechanisms involved in the mechanotransduction pathways that control MSC differentiation in these previous examples, researchers focused on how mechanical forces are transduced into biochemical signals. From a physical point of view, for instance, cells can respond to mechanical signals playing elastic forces depending on the stiffness of the substrate. The range of picoNewton (pN) molecular forces is sufficient to mechanically influence protein affinity and thus, functionality [32]. From a chemical point of view, it has been demonstrated that mechanical signals can trigger the activation of several signaling pathways such as those characterized by Ras/MAPK, PI3K/Akt, TGF-β and RhoA/ROCK.

Researchers also highlighted an interesting phenomenon related to the migration of transcription factors involved in key cellular mechanisms. In a famous study, Sirio Dupont showed how two mechanotransduction mediators YAP (Yes-associated protein)/TAZ (transcriptional coactivator with PDZ-binding motif) localization is strictly related to the rigidity and cell shape (Fig. 1.3) [33].

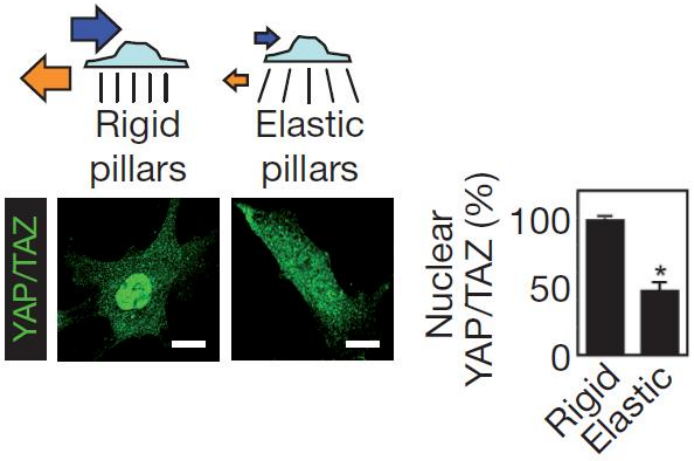

Fig. 1.3 YAP/TAZ localization in MSCs plated on micropillars arrays of different rigidity [33]. Nuclear YAP/TAZ(%) is higher when MSCs are plated on rigid microprillars with rather than elastic ones. Black lines represent rigid micropillars; blue arrows represent cytoskeletal tension; orange arrows show the pull against the ECM; the dimension of the arrow indicate the degree of mechanical forces.

Anyway, the knowledge of the mechanical mechanisms that trigger or facilitate this rapid factor re-localization, depending on the mechanical influence, is still challenging. Deepening the mechanotransduction event from a molecular point of view, the involved characters include any kind of element: membrane receptors, cytoskeletal proteins, DNA, and so on (Fig. 1.4) [35].

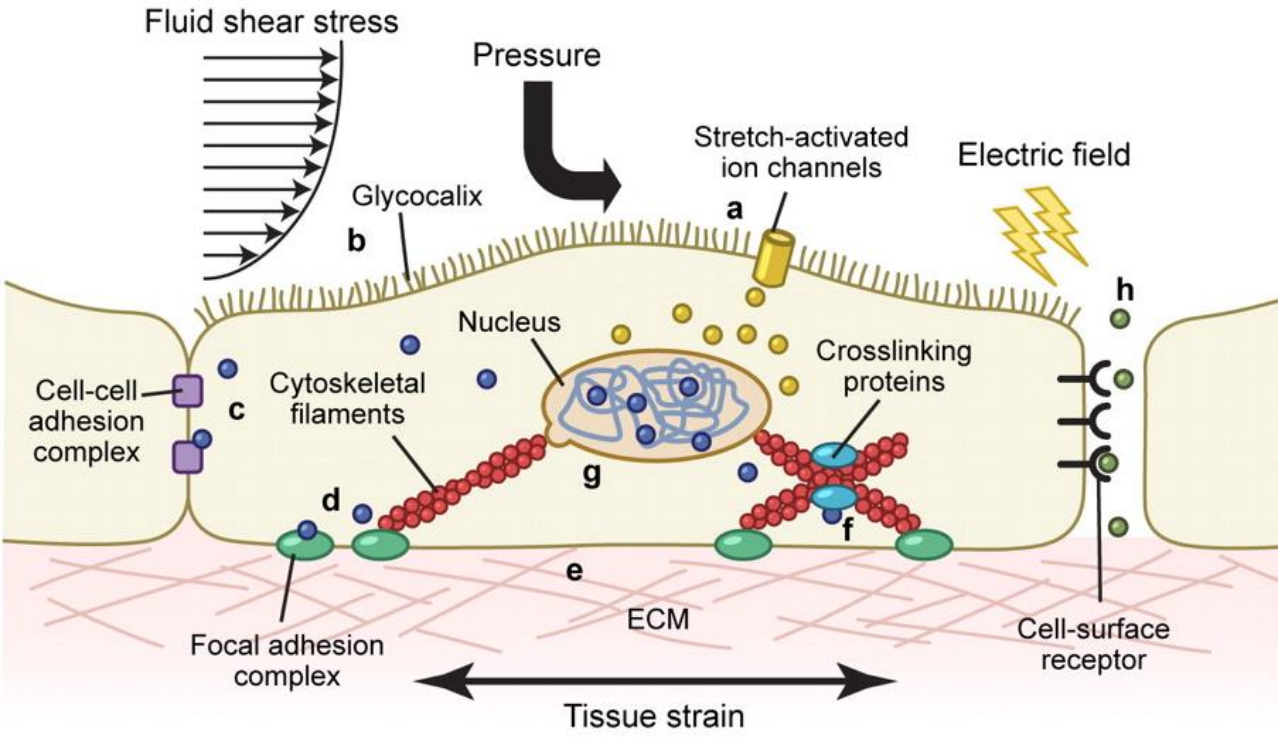

Fig. 1.4 Schematic representation of machanotransduction [35]. MSCs response to external mechanical stimuli, such as fluid shear stress, pressure, electric fields and tissue strain, with several biological mechanosensors: **a**. Stretch-activated ion channels. **b.** Single cilia or the glycocalix. **c, d.** Cell-cell junctional receptors or extracellular matrix (ECM)-cell focal adhesions. **e.** Force-induced unfolding of ECM proteins. **f.** Cytoskeletal elements, e.g. filaments, crosslinkers or motor proteins. **g.** The nucleus. Chromatin conformation alteration can modulate access to transcription factors or transcriptional complex. **h.** External mechanical stimuli can compress intercellular space and alter the passage of autocrine and paracrine signaling molecules.

The first actor of this signaling mechanism is the extracellular matrix (ECM) which is subjected to the external perturbations and undergoes protein unfolding when it is mechanically extended. Some cell membrane components function as “antennas”, capturing chemical and mechanical signals from ECM and extracellular environment and transducing them into a message to the nucleus. These elements are cilia, integrins, cadherins and ion channels. Integrins represent the direct linkage between ECM and intracellular environment, binding cytoskeleton through focal adhesions. In this way an external signal

transmitted through the ECM will be translated in a rearrangement of cytoskeletal elements. The communication between integrins and the nucleus is mediated by intermediate filaments extended from plasmatic membrane to nuclear membrane. Cadherins are mediators of cell-cell interactions. The involvement of cadherins in mechanotransduction is due to their dependence to calcium. When intracellular calcium concentration changes, cadherin is thought to a conformational change that leads to cytoskeleton rearrangements and the release of the signaling molecule β–catenin [36]. Mechanical stimuli are found to be transduced also through ionic concentrations changes since mechanical stretch leads to modifications to ion channel activity [37]. As focal adhesions connect ECM to the cytoskeleton, LINCs (linker of nucleoskeleton and cytoskeleton) interact with cytoskeleton in the cytoplasmatic area and with lamin in the nuclear environment, contributing to the arrival of the external mechanical signal to the nucleus. The LINC components are composed by emerin, lamin A/C, SUN1, SUN2 and nesprins. In the lamin skeleton, lamin A is the element which more stabilizes the nucleus against mechanical stress acting positively also on chromatin [38]. Together with the LINC complexes, the other potential linkage between cytoplasm and nucleus for mechanotransduction event is the nuclear pore complex (NPC) (Fig. 1.5). Recent evidences have demonstrated as LINC complexes and NPC directly interact and influence each other [39]. Unfortunately the total knowledge of NPC real involvement in mechanotransduction still remains a challenge. It should be proven whether cell mechanical forces could alter the NPC and thus the properties of the pore and the nuclear environment.

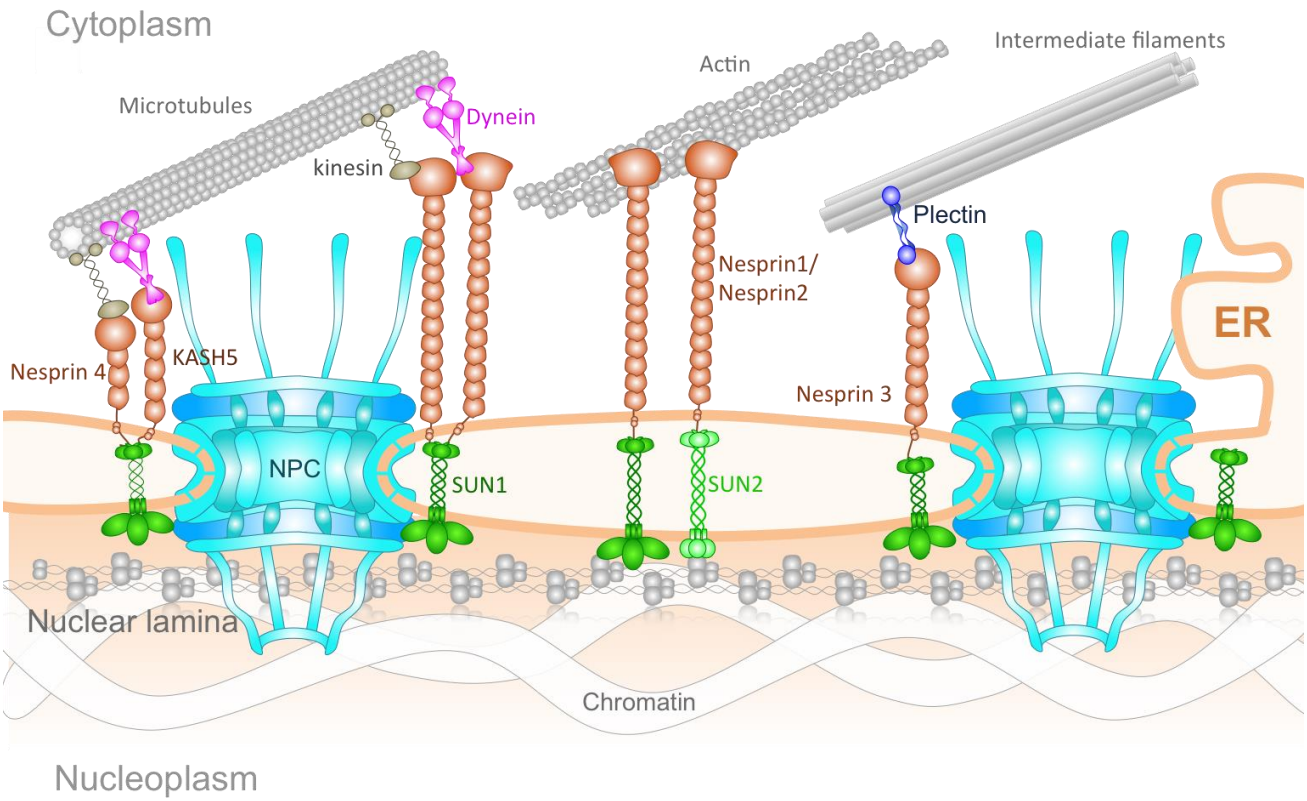

Fig. 1.5 Schematic representation of connections between nucleus and cytoplasm [39]. In the cytoplasm, both NPC and LINC complexes interact with microtubules through dynein and kinesis motor proteins. LINC complexes also associate directly with actin and with intermediate filaments through plectins. In the nuclear compartment, both NPCs and LINC complexes interact with lamina and chromatin.

The transmission of the mechanical loading by LINC complex and NPC to the nucleocytoskeleton alters the lamin structure and, as consequence, the chromatin organization, leading to the exposure of specific binding sites to the transcription machinery. This structural rearrangement of the nucleus is demonstrated also by some studies in which it has been measured the nuclear aspect ratio (NAR) to evaluate the influence of growing cells on 3D scaffolds. NAR is found to change depending on the type of substrate on which cells grow. In fact cells cultured in 3D scaffold show a higher NAR value than control cells, resulting in a more elongated nuclear structure following the direction of the scaffold [40].

NICHOID: a challenging project

In 2015, the NICHOID project started taking together all the current challenging issues of MSC therapy. This project is headed by Manuela T. Raimondi and is funded by the European Research Council under the European Union's Horizon 2020 research and innovation program (G.A. No. 646990 – NICHOID). The focus of the project is on the mechanobiology of nuclear import of transcription factors modeled within a bioengineered stem cell niche. The main hypothesis underlying the project is that the nucleus and the nuclear pores are mechanically sensitive elements and respond to cell stretching with nuclear envelope surface increasing and nuclear pore enlarging. This mechanism, together with a potential increase of NPC number on a longer time scale [41], would promptly increase the permeability of the nuclear envelope and the inner flux of the transcription factors involved into differentiation (e.g. Osx, MyoD, Sox9) or mechanotransduction (e.g. YAP/TAZ). The validation of this hypothesis would explain events, such that observed by Dupont and colleagues [33], but also would put light on the black box represented by the real involvement of the NPC in mechanotransduction. NPC represents the last and the effective barrier which can regulate the inner flux of transcription factors whose activity leads to the effective cellular fate alteration. The comprehension of the nuclear mechanics would contribute to better control MSC proliferation and differentiation, and thus MSC therapy.

Preliminary studies on MSCs cultured on a 3D cell culture substrate provided interesting results on mechanical responses of MSCs. The 3D scaffold, the nichoid, was formed in a polymeric photoresist, named SZ2080, by two photon-laser polymerization (2PP). Most traditional scaffolds offered cell adhesion surfaces far from physiological 3D

environment. Induced cell spreading on artificial surfaces altered stem cell differentiation and behavior [42]. To avoid cell spreading, a step forward was to use separated micropillars or microwells that confine cell into microaggregates [33, 43]. However, these 3D culture systems excluded all the 3D structural interactions that stimulate cells in a physiological environment. The nichoid scaffold filled this gap offering a synthetic environment in which stem cells could freely adhere in three dimensions mimicking, at a single cell level, the native extracellular structural interactions [44] (Fig. 1.6).

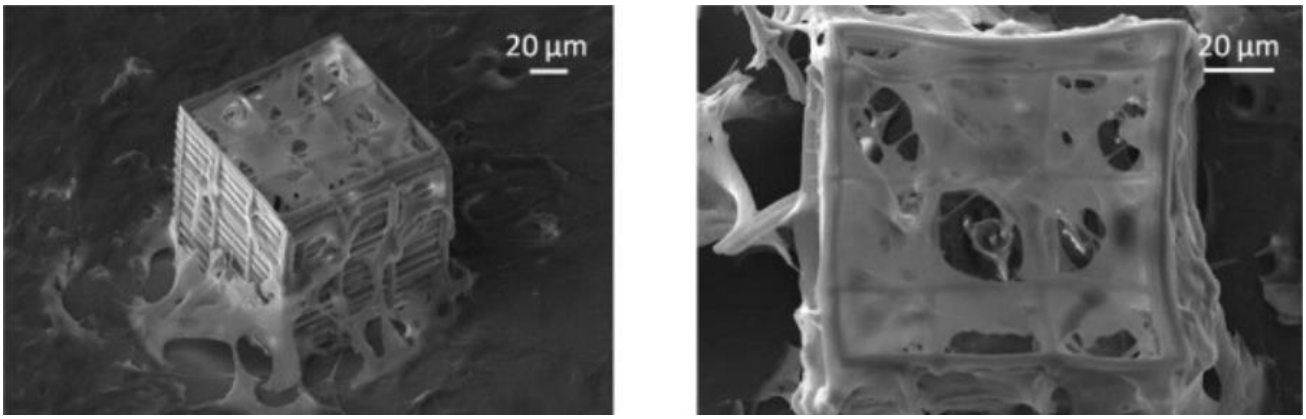

Fig. 1.6 Scanning electron microscope (SEM) image of MG63 osteosarcoma cells cultured in the 2PP-engineered nichoid (30 × 90 µm) [44].

The name “nichoid” was given to this 3D scaffold because of its properties. In fact, it reproduced a synthetic stem cell niche by directing stem cell homing and hematopoietic colony formation without the addition of any chemical substances [44]. Furthermore, it was able to maintain stemness by pluripotency gene expression upregulation and differentiation gene expression downregulation [45]. From a cell morphology point of view, stem cells grown into the nichoid showed an isotropic cell adhesion and a consequent roundish nuclear shape with respect to 2D cultured cells that showed more stretched nuclei (Fig. 1.7) [46].

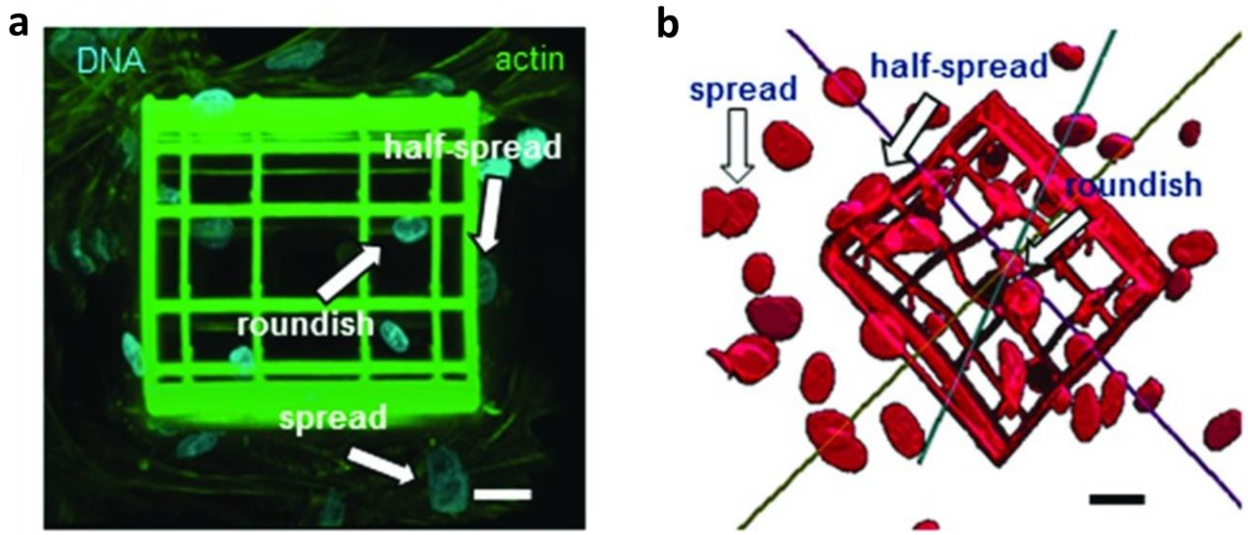

Fig. 1.7 Nichoid structure induces different nuclear spreading level depending on MSC localization. (a) 3D confocal projection of niche-cultured MSCs. DNA is stained in blue (DAPI); actin filaments are immune-stained in green. (b) Fully 3D reconstruction of the niche cellularised sample. Scale bar: 20μm [46].

These observations led to the consideration by which isotropic forces and cell adhesion could influence nuclear shape and stem cell fate and in particular to a direct correlation between nuclear morphology and stemness state. From these findings, arouse the main hypothesis of the ERC project by which the connection between the nuclear morphology and the stemness state is specifically given by the mechanical alteration of the NPC structure and nuclear permeability.
The research activity focused on verifying the main hypothesis of the project and are mainly three: first, an experimental part should include the development of fluorescent transcription factors and the measurement of their nuclear import flow; second, a multiscale computational modeling section should simulate a numerical prediction of the transcription factor flow in a stretched nucleus with respect to a roundish nucleus; third, the final integration of the measured flows with the computational predictions will verify or contradict the hypothesis

that nuclear strain states regulate nuclear permeability and thus cellular mechano-response.

Measurement of nuclear import

In eukaryotic cells, NPC are embedded in a double lipid membrane, the nuclear envelope (NE). The NPC allow the passage of several molecules of various dimension and nature, from ions to RNAs and ribonucleoproteins. At a molecular level, the NPC is composed by about 30 different proteins, namely nucleoporins (Nups), and has a total molecular weight of about 125 MDa (Fig.1.8).The dimension of the inner pore is about 40 nm. In according to the hypothesis of the NICHOID project, during a mechanical stress the nuclear pore could rearrange the structure and alter the flux through the pore. In a recent study Garcia-Gonzaléz and colleagues demonstrated that MSCs cultured in the nichoid (roundish nuclei) showed a slower nuclear import of diffusive molecules compared to spread cells (deformed nuclei) [46, 47]. It still remains to demonstrate if the more complex active import of transcription factors follow the same mechano-regulation.

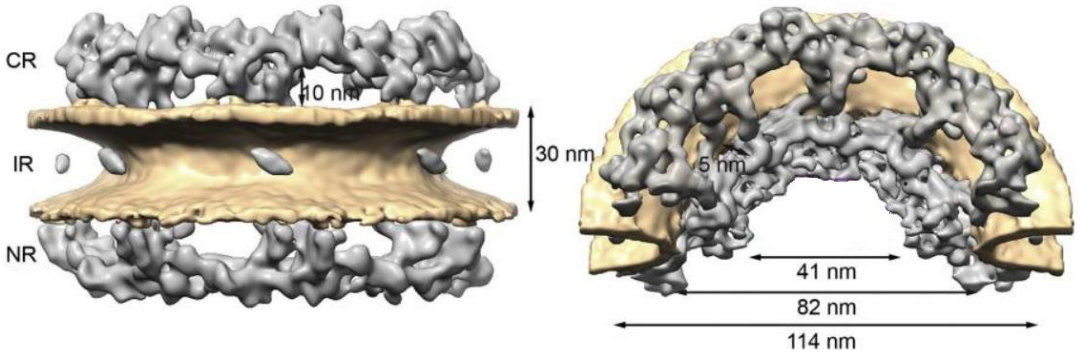

Fig. 1.8 Isosurface rendering of the structure of the human NPC resolved to 33 Å seen from front (left), cut in half and tilted (right). CR: cytoplasmic ring; IR: inner ring; NR: nucleoplasmic ring. Adapted from Ref. [48].

F. Cardarelli in a recent review gave an overview of the current approaches for measuring nucleocytoplasmic transport and thus, the fluxes trough the nuclear pores [49]. He divided the strategies in three classes of methods. The first included perturbation-based techniques. By these methods, it is possible to calculate the characteristic time of molecular transport of many molecules across many pores in the NE. The main characteristic of these techniques is that they are based on the alteration of the optical properties of the fluorescent molecules maintaining their functionality. This class includes photobleaching methods (e.g. FRAP), photoactivation (when non-fluorescent molecules become fluorescent after specific irradiation), photoconversion (when a molecule switches its fluorescent state to another fluorescent state after illumination at a selected wavelength), photoswitching (when the fluorescence can be switched on and off at selected wavelength irradiation). Among the perturbation-based strategies, Fluorescence Recovery After Photobleaching (FRAP), is the most used method in nucleocytoplasmic transport measurement. Basically, as shown in the figure 1.9, an intense light pulse is used to photobleach the fluorescence of molecules into a specific region of interest (ROI). The fluorescence recovery given by the import rate of the fluorescent molecules from the outside to the inside of the ROI, provides some output data as the characteristic time of molecular transport and thus, the time required to the recovery of the equilibrium state. In the NICHOID project specific case the ROI should be defined by the nuclear section and the outside environment by the cytoplasm.
Recent advancements in molecular engineering developed different fluorescent labels that improved perturbation-based strategies. The most used fluorescent probes are all based on the original structure of the green fluorescent protein (GFP) extracted by the jellyfish *Aequorea*

victoria [50]. From that native peptide were developed several variants with different fluorescence properties, altering the fluorescence emission spectrum (e.g. mCherry, Yellow Fluorescent Protein) or the photosensitivity properties (photoactivation, photoswitching, photoconversion) or the intracellular delivery method (e.g. protein transduction technology).

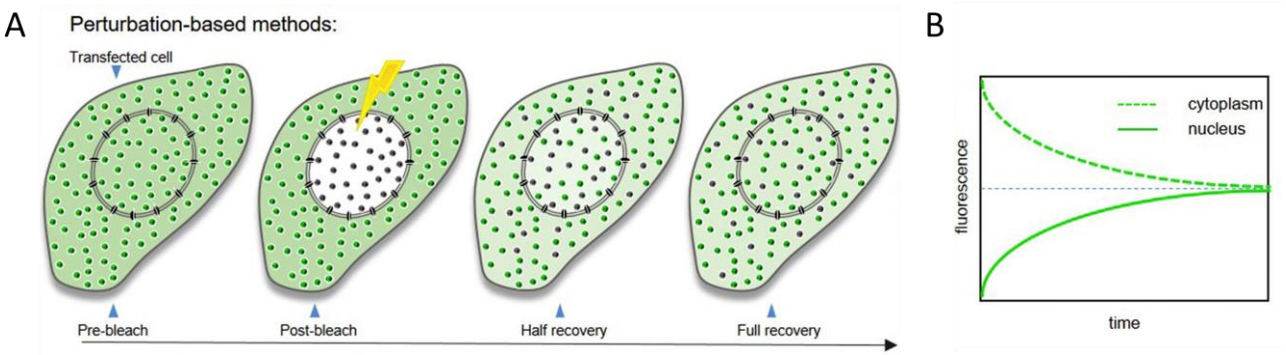

Fig. 1.9 Schematic representation of the FRAP method, a photo-perturbation-based approach to nucleocytoplasm transport measurement. (A) In the first frame the cell appears totally fluorescent. In the successive step, the nucleus is photobleached to then follow the recovery of the fluorescence given by the import of fluorescent molecule from the cytoplasm to the nucleus. (B) A typical output graph is characterized by a plot of decreasing fluorescence in the cytoplasm and one of exponential fluorescence recovery in the nucleus. Adapted from Ref. [49].

The second class of methods used to measure nucleocytoplasmic transport comprises localization-based single particle tracking (SPT) methods. SPT requires an expertise both in sample preparation (molecule must be purified, labeled and microinjected or cell permeabilized) and in tracking acquisition.

The third class includes fluctuation-based methods that rely on the rapid acquisition of fluorescence signal fluctuations left at equilibrium steady state. It provides information almost at the level of single molecule but in presence of many similarly labelled molecules and in live, unperturbed cells.

Recently, Elosegui-Artola and colleagues published a very interesting study on the influence of force transmission to nuclear import of YAP, a transcriptional activator involved in mechanotransduction. They used mouse embryonic fibroblasts to evaluate the nuclear import of the factor by fusing YAP to an enhanced form of GFP and measuring its shuttling by FRAP technique. Even if the cell model and mechanical conditioning was completely different, their results were very encouraging in the perspective of the NICHOID hypothesis validation. They demonstrated that force transmission leads to nuclear flattening, reducing the nuclear mechanical resistance to molecular transport and thus, increasing nuclear permeability to YAP import [51].

Motivation and thesis objective

My Ph.D. thesis developed in the context of the NICHOID project and in particular in the experimental validation of its main hypothesis, which is that during a mechanical cell stress event, the nucleus and the nuclear pore complexes, as mechanically sensitive elements, respond through nuclear pore structure rearrangement and nuclear permeability alteration. In order to experimentally validate this hypothesis, we had to measure the nuclear import flow of molecules in different cell stretching conditions: stretched cells cultured on a flat substrate and unstretched cells cultured into the 3D synthetic stem niche, the nichoid.
In more details, my goal was to engineer transcription factors, promoters of MSC differentiation, in order to achieve suitable fluorescent tools for the measurement of their nuclear import rate. This objective included specific requirements that I had to consider in the transcription factors engineering:

(1) Nuclear localization. The final fluorescent tools should physiologically be imported into the nucleus.
(2) Fluorescence Properties. Engineered factors should exhibit fluorescence properties suitable for the selected nucleocytoplasmic transport measurement techniques.
(3) Dimension. The fluorescent probe has to be the smallest as possible in order to minimize the alteration of the dynamics of the native protein, considering also the nuclear pore structures sizes (Fig. 1.8).
(4) Functionality. Engineered proteins should maintain the transcriptional promoting activity of the native factor. The maintenance of the functionality would ensure a correct intracellular dynamics of the recombinant factor (Fig. 1.10) and

could allow further biochemical investigations based on their biological properties of the transcription factors.

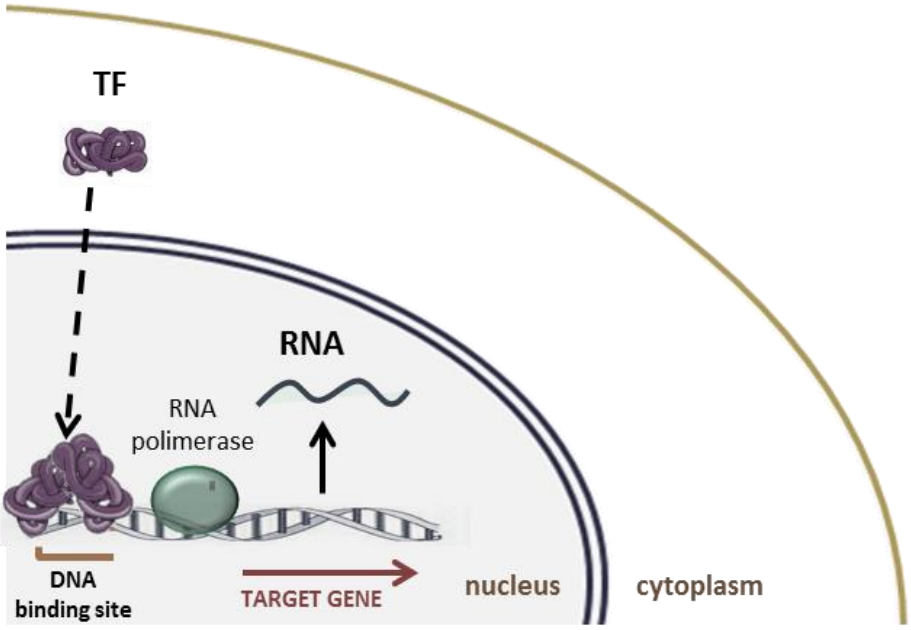

Fig 1.10 Graphical representation of the intracellular path of a transcription factor. The transcription factor is translated in the cytoplasm where it remains until its activation. Then it is imported into the nucleus where it binds to DNA in monomeric or multimeric form. Once it binds to the DNA, it promotes the transcription of specific target genes whose protein products trigger specific signaling mechanisms.

References

1. Dominici M, Le Blanc K, Mueller I, Slaper-Cortenbach I, Marini F, Krause D, Deans R, Keating A, Prockop Dj, Horwitz E. Minimal criteria for defining multipotent mesenchymal stromal cells. The International Society for Cellular Therapy position statement. Cytotherapy. 2006;8(4):315-7.

2. Barry FP, Murphy JM. Mesenchymal stem cells: clinical applications and biological characterization. Int J Biochem Cell Biol. 2004 Apr;36(4):568-84.

3. Volarevic V, Markovic BS, Gazdic M, Volarevic A, Jovicic N, Arsenijevic N, Armstrong L, Djonov V, Lako M, Stojkovic M. Ethical and Safety Issues of Stem Cell-Based Therapy. Int J Med Sci. 2018 Jan 1;15(1):36-45.

4. Meier RP, Müller YD, Morel P, Gonelle-Gispert C, Bühler LH. Transplantation of mesenchymal stem cells for the treatment of liver diseases, is there enough evidence? Stem Cell Res. 2013 Nov;11(3):1348-64.

5. Németh K, Leelahavanichkul A, Yuen PS, Mayer B, Parmelee A, Doi K, Robey PG, Leelahavanichkul K, Koller BH, Brown JM, Hu X, Jelinek I, Star RA, Mezey E. Bone marrow stromal cells attenuate sepsis via prostaglandin E(2)-dependent reprogramming of host macrophages to increase their interleukin-10 production. Nat Med. 2009 Jan;15(1):42-9.

6. Choi H, Lee RH, Bazhanov N, Oh JY, Prockop DJ. Anti-inflammatory protein TSG-6 secreted by activated MSCs attenuates zymosan-induced mouse peritonitis by decreasing TLR2/NF-κB signaling in resident macrophages. Blood. 2011 Jul 14;118(2):330-8.

7. English K, Ryan JM, Tobin L, Murphy MJ, Barry FP, Mahon BP. Cell contact, prostaglandin E(2) and transforming growth factor beta 1 play non-redundant roles in human mesenchymal stem cell induction of CD4+CD25(High) forkhead box P3+ regulatory T cells. Clin Exp Immunol. 2009 Apr;156(1):149-60.

8. Ren G, Zhang L, Zhao X, Xu G, Zhang Y, Roberts AI, Zhao RC, Shi Y. Mesenchymal stem cell-mediated immunosuppression occurs via concerted action of chemokines and nitric oxide. Cell Stem Cell. 2008 Feb 7;2(2):141-50.
9. Spaggiari GM, Capobianco A, Abdelrazik H, Becchetti F, Mingari MC, Moretta L. Mesenchymal stem cells inhibit natural killer-cell proliferation, cytotoxicity, and cytokine production: role of indoleamine 2,3-dioxygenase and prostaglandin E2. Blood. 2008 Feb 1;111(3):1327-33.
10. He XW, He XS, Lian L, Wu XJ, Lan P. Systemic infusion of bone marrow-derived mesenchymal stem cells for treatment of experimental colitis in mice. Dig Dis Sci. 2012 Dec;57(12):3136-44.
11. Phillips CD, Wongsaisri P, Htut T, Grossman T. Purified umbilical cord derived mesenchymal stem cell treatment in a case of systemic lupus erythematosus. Clin Transl Med. 2017 Dec;6(1):31.
12. Abd Elhalem SS, Haggag NZ, El-Shinnawy NA. Bone marrow mesenchymal stem cells suppress IL-9 in adjuvant-induced arthritis. Autoimmunity. 2018 Feb;51(1):25-34.
13. Madigan M, Atoui R. Therapeutic Use of Stem Cells for Myocardial Infarction. Bioengineering (Basel). 2018 Apr 6;5(2).
14. Bang OY, Kim EH, Cha JM, Moon GJ. Adult Stem Cell Therapy for Stroke: Challenges and Progress. J Stroke. 2016 Sep;18(3):256-266.
15. Zhao L, Chen S, Shi X, Cao H, Li L. A pooled analysis of mesenchymal stem cell-based therapy for liver disease. Stem Cell Res Ther. 2018 Mar 21;9(1):72.
16. Ahmed SM, Morsi M, Ghoneim NI, Abdel-Daim MM, El-Badri N. Mesenchymal Stromal Cell Therapy for Pancreatitis: A Systematic Review. Oxid Med Cell Longev. 2018 Mar 18;2018:3250864.
17. Marigo I, Dazzi F. The immunomodulatory properties of mesenchymal stem cells. Semin Immunopathol. 2011 Nov;33(6):593-602.
18. Li C, Fu Y, Wang Y, Kong Y, Li M, Ma D, Zhai W, Wang H, Lin Y, Liu S, Ren F, Li J, Wang Y. Mesenchymal stromal cells ameliorate acute allergic rhinitis in rats. Cell Biochem Funct. 2017 Oct;35(7):420-425.

19. Patel SA, Meyer JR, Greco SJ, Corcoran KE, Bryan M, Rameshwar P. Mesenchymal stem cells protect breast cancer cells through regulatory T cells: role of mesenchymal stem cell-derived TGF-beta. J Immunol. 2010 May 15;184(10):5885-94.
20. Lazennec G, Jorgensen C. Concise review: adult multipotent stromal cells and cancer: risk or benefit? Stem Cells. 2008 Jun;26(6):1387-94.
21. Robering JW, Weigand A, Pfuhlmann R, Horch RE, Beier JP, Boos AM. Mesenchymal stem cells promote lymphangiogenic properties of lymphatic endothelial cells. J Cell Mol Med. 2018 May 11. doi: 10.1111/jcmm.13590.
22. Di Bonzo LV, Ferrero I, Cravanzola C, Mareschi K, Rustichell D, Novo E, Sanavio F, Cannito S, Zamara E, Bertero M, Davit A, Francica S, Novelli F, Colombatto S, Fagioli F, Parola M. Human mesenchymal stem cells as a two-edged sword in hepatic regenerative medicine: engraftment and hepatocyte differentiation versus profibrogenic potential. Gut. 2008 Feb;57(2):223-31.
23. Abbasi-Malati Z, Roushandeh AM, Kuwahara Y, Roudkenar MH. Mesenchymal Stem Cells on Horizon: A New Arsenal of Therapeutic Agents. Stem Cell Rev. 2018 Apr 23.
24. Baldari S, Di Rocco G, Piccoli M, Pozzobon M, Muraca M, Toietta G. Challenges and Strategies for Improving the Regenerative Effects of Mesenchymal Stromal Cell-Based Therapies. Int J Mol Sci. 2017 Oct 2;18(10).
25. Hiew VV, Simat SFB, Teoh PL. The Advancement of Biomaterials in Regulating Stem Cell Fate. Stem Cell Rev. 2018 Feb;14(1):43-57.
26. Moon MY, Kim HJ, Choi BY, Sohn M, Chung TN, Suh SW. Zinc Promotes Adipose-Derived Mesenchymal Stem Cell Proliferation and Differentiation towards a Neuronal Fate. Stem Cells Int. 2018 Apr 18;2018:5736535.
27. Le W, Yao J. The Effect of Myostatin (GDF-8) on Proliferation and Tenocyte Differentiation of Rat Bone Marrow-Derived Mesenchymal Stem Cells. J Hand Surg Asian Pac Vol. 2017 Jun;22(2):200-207.

28. Bana N, Sanooghi D, Soleimani M, Hayati Roodbari N, Alavi Moghaddam S, Joghataei MT, Sayahpour FA, Faghihi F. A Comparative Study to Evaluate Myogenic Differentiation Potential of Human Chorion versus Umbilical Cord Blood-derived Mesenchymal Stem Cells. Tissue Cell. 2017 Aug;49(4):495-502.
29. Sun M, Chi G, Li P, Lv S, Xu J, Xu Z, Xia Y, Tan Y, Xu J, Li L, Li Y. Effects of Matrix Stiffness on the Morphology, Adhesion, Proliferation and Osteogenic Differentiation of Mesenchymal Stem Cells. Int J Med Sci. 2018 Jan 15;15(3):257-268.
30. Guilak F, Cohen DM, Estes BT, Gimble JM, Liedtke W, Chen CS. Control of stem cell fate by physical interactions with the extracellular matrix. Cell Stem Cell. 2009 Jul 2;5(1):17-26.
31. Delaine-Smith RM, Reilly GC. Mesenchymal stem cell responses to mechanical stimuli. Muscles Ligaments Tendons J. 2012 Oct 16;2(3):169-80.
32. Mechanotransduction: use the force(s). Ewa K. Paluch, Celeste M. Nelson, Nicolas Biais, Ben Fabry, Jens Moeller, Beth L. Pruitt, Carina Wollnik, Galina Kudryasheva, Florian Rehfeldt, Walter Federle BMC Biol. 2015; 13: 47. Published online 2015 Jul 4.
33. Dupont S, Morsut L, Aragona M, Enzo E, Giulitti S, Cordenonsi M, Zanconato F, Le Digabel J, Forcato M, Bicciato S, Elvassore N, Piccolo S. Role of YAP/TAZ in mechanotransduction. Nature. 2011 Jun 8;474(7350):179-83.
34. Steward AJ, Kelly DJ. Mechanical regulation of mesenchymal stem cell differentiation. J Anat. 2015 Dec;227(6):717-31. doi: 10.1111/joa.12243
35. Bonnet N, Ferrari SL. Exercise and the skeleton: How it works and what it really does. IBMS BoneKEy (2010) 7, 235–248.
36. Arnsdorf EJ, Tummala P, Jacobs CR. Non-canonical Wnt signaling and N-cadherin related beta-catenin signaling play a role in mechanically induced osteogenic cell fate. PLoS One. 2009;4(4):e5388.

37. Campbell JJ, Bader DL, Lee DA. Mechanical loading modulates intracellular calcium signaling in human mesenchymal stem cells. J Appl Biomater Biomech. 2008 Jan-Apr;6(1):9-15.
38. Swift J, Ivanovska IL, Buxboim A, Harada T, Dingal PC, Pinter J, Pajerowski JD, Spinler KR, Shin JW, Tewari M, Rehfeldt F, Speicher DW, Discher DE. Nuclear lamin-A scales with tissue stiffness and enhances matrix-directed differentiation. Science. 2013 Aug 30;341(6149):1240104.
39. Jahed Z, Soheilypour M, Peyro M, Mofrad MR. The LINC and NPC relationship -it's complicated! J Cell Sci. 2016 Sep 1;129(17):3219-29.
40. Nathan AS, Baker BM, Nerurkar NL, Mauck RL. Mechano-topographic modulation of stem cell nuclear shape on nanofibrous scaffolds. Acta Biomater. 2011 Jan;7(1):57-66.
41. Richard MN, Deniset JF, Kneesh AL, Blackwood D, Pierce GN. Mechanical stretching stimulates smooth muscle cell growth, nuclear protein import, and nuclear pore expression through mitogen-activated protein kinase activation. J Biol Chem. 2007 Aug 10;282(32):23081-8.
42. Nelson WJ. Adaptation of core mechanisms to generate cell polarity. Nature. 2003 Apr 17;422(6933):766-74.
43. Gobaa S, Hoehnel S, Roccio M, Negro A, Kobel S, Lutolf MP. Artificial niche microarrays for probing single stem cell fate in high throughput. Nat Methods. 2011 Oct 9;8(11):949-55.
44. Raimondi MT, Eaton SM, Laganà M, Aprile V, Nava MM, Cerullo G, Osellame R. Three-dimensional structural niches engineered via two-photon laser polymerization promote stem cell homing. Acta Biomater. 2013 Jan;9(1):4579-84.
45. Nava MM, Piuma A, Figliuzzi M, Cattaneo I, Bonandrini B, Zandrini T, Cerullo G, Osellame R, Remuzzi A, Raimondi MT. Two-photon polymerized "nichoid" substrates maintain function of pluripotent stem cells when expanded under feeder-free conditions. Stem Cell Res Ther. 2016 Sep 9;7(1):132.

46. Nava MM, Fedele R, Raimondi MT. Computational prediction of strain-dependent diffusion of transcription factors through the cell nucleus. Biomech Model Mechanobiol. 2016 Aug;15(4):983-93.
47. García-González A, Jacchetti E, Marotta R, Tunesi M, Rodríguez Matas JF, Raimondi MT. The Effect of Cell Morphology on the Permeability of the Nuclear Envelope to Diffusive Factors. Front Physiol. 2018 Jul 13;9:925.
48. Garcia A, Rodriguez Matas JF, Raimondi MT. Modeling of the mechano-chemical behaviour of the nuclear pore complex: current research and perspectives. Integr Biol (Camb). 2016 Oct 10;8(10):1011-1021.
49. Von Appen A, Beck M. Structure Determination of the Nuclear Pore Complex with Three-Dimensional Cryo electron Microscopy. J Mol Biol. 2016 May 22;428(10 Pt A):2001-10.
50. Cardarelli F. Time-resolved biophysical approaches to nucleocytoplasmic transport. Comput Struct Biotechnol J. 2017 Apr 4;15:299-306.
51. Shimomura O, Johnson FH, Saiga Y. Extraction, purification and properties of aequorin, a bioluminescent protein from the luminous hydromedusan, *Aequorea*. J Cell Comp Physiol. 1962 Jun.
52. Elosegui-Artola A, Andreu I, Beedle AEM, Lezamiz A, Uroz M, Kosmalska AJ, Oria R, Kechagia JZ, Rico-Lastres P, Le Roux AL, Shanahan CM, Trepat X, Navajas D, Garcia-Manyes S, Roca-Cusachs P. Force Triggers YAP Nuclear Entry by Regulating Transport across Nuclear Pores. Cell. 2017 Nov 30;171(6):1397-1410.

CHAPTER 2: Development of fluorescent transcription factors

This chapter will present two approaches to engineer a fluorescent transcription factor (TF). The first work will present the advantages and limitations of protein transduction-based fluorescent TFs able to pass the plasmatic membrane and reach the nucleus within few hours. The second work will present the evaluation of photosensitive TFs able to change their optical properties in response to specific light irradiation.
The common part in the design of the different fluorescent tools is the fusion of (1) the label to make it detectable by the fluorescence microscopy and (2) the protein of interest (POI). According to NICHOID hypothesis and my Ph.D aim, the POI had to be a cell protein that in response to mechanical input migrates to the nucleus to trigger key cellular mechanisms. The factors that fit this last description are transcription factors that in response to specific mechanical signals migrate from the cytoplasm to the nucleus in order to bind the DNA to promote the transcription of target genes and the activation of specific cell signaling pathways, such as MSC differentiation.

Mechanotranscription for MSC differentiation

Mechanotranscription is defined as the mechanism where a mechanical input is transduced into a chemical signal leading to gene transcription. Mechanotranscription in the context of MSC differentiation is still a not well-defined mechanism. Among all the transcription factors involved in MSC differentiation pathways, few factors have been characterized for mechanotranscription (Table 2.1).

Differentiation pathways	Factors	Type	Molecular weight (kDa)	Ref.
osteogenesis	**Runx2 (Cbfa1)**	Runt-related TF	18.8	1,2,3,6
	Osterix	Zinc Finger TF	44.9	1,6
	Dlx Family	Homeobox TF	Dlx3: 31.7 Dlx5: 31.5 Dlx6: 32.5	1,6
adipogenesis	**PPARγ**	Nuclear Receptor	54.7	1,2,4,5,6
	C/EBPS	Basic Leucine Zipper Domain TF	α: 35.9 β: 36.1 γ: 28.4	4,6
	SREBP1/ADD1	Sterol Regulatory Element-Binding TF	~49	6
chondrogenesis	**Sox9**	SRY-Related High Mobility Group-Box TF	56.1	1, 3, 6
	Sox5		84	1, 6
	Sox6		91.9	1, 6
	Runx2 (*Cbfa-1*)	Runt-Related TF	18.8	1,2,3,6
myogenesis	**Myod**	Basic Helix Loop Helix TF	34.5	1,7
	Myogenin		25	7
	Myf5		28.3	7
	Myf6 (MRF4)		26.9	7
tenogenesis	**Scleraxis**	Basic Helix Loop Helix TF	21.6	8
	Mohawk	Homeobox TF	39.4	9
	Egr1	C_2H_2-Type Zinc Finger TF	57.5	10
neurogenesis	**Ascl1**	Basic Helix Loop Helix TF	25.5	11
	Neurogenin		25.7	11,12
	Foxa2	Forkhead Box Transcription Protein	48.9	13

Table 2.1. Transcription factors (TFs) promoting MSC differentiation. Characteristics of the main factors responsible for earlier stages of MSC differentiation. TFs found to be connected into the mechanotranscription mechanism are highlighted in yellow.

One of the first pioneering work was published by Yanigasawa and colleagues in 2007. The aim of the authors was to determine the effects of the mechanical loading on a cell line, C2C12 cells (progenitor cells of myoblasts), originated from undifferentiated mesenchymal cells maintaining the capacity of differentiating into the mesodermal lineages. They assayed the mechanical effect by analyzing the gene expression level of specific mRNAs [1]. In this study they observed that depending on the magnitude of the compressive force applied to cell culture, gene expression levels of several TFs changed in a mechanical stress-dependent way. They analyzed the gene expression of TFs leading to chondrogenesis (Sox5, Sox9, PPARγ), osteogenesis (Runx2, Msx2, Dlx5, Osterix, AJ18) and myogenesis (MyoD). Recently other research groups investigated the effect of different mechanical stimuli on stem cell fate. R. Li and colleagues observed an anti-adipogenic effect of mechanical stretching stimulus applied on MSCs [4]. L. Bjerre cultured MSCs on silicate-substituted tricalcium phosphate (Si-TCP) scaffolds under flow perfusion conditions. Cells showed improved proliferation and osteogenic differentiation [14]. C. Yang and colleagues demonstrated that MSCs possess mechanical memory able to collect information about environment such as the stiffness of culture substrates. [2].

In table 2.1 I resumed the main TFs promoters of the earlier stages of MSC differentiation. In yellow are highlighted the factors that have been studied in association with mechanical signals and thus, in the context of mechanotranscription. As this table clearly shows, the pathways investigated so far are those characterizing the three mesodermal cell lineages that International Society of Cellular Therapy (ISCT) defined for the determination of MSC population: osteogenesis, adipogenesis and chondrogenesis.

Further research in mechanotranscription will improve the comprehension of the phenomenon and will help to unfold challenging questions about mechanotransduction and MSC functionality. The knowledge of which factors is involved in mechanotranscription would help in choosing specific molecules linked to mechanical signals.

References

1. Yanagisawa M, Suzuki N, Mitsui N, Koyama Y, Otsuka K, Shimizu N. Effects of compressive force on the differentiation of pluripotent mesenchymal cells. Life Sci. 2007 Jul 12;81(5):405-12.

2. Yang C, Tibbitt MW, Basta L, Anseth KS. Mechanical memory and dosing influence stem cell fate. Nat Mater. 2014 Jun;13(6):645-52. doi: 10.1038/nmat3889. Epub 2014 Mar 16.

3. Murphy CM, Matsiko A, Haugh MG, Gleeson JP, O'Brien FJ. Mesenchymal stem cell fate is regulated by the composition and mechanical properties of collagen-glycosaminoglycan scaffolds. J Mech Behav Biomed Mater. 2012 Jul;11:53-62.

4. Li R, Liang L, Dou Y, Huang Z, Mo H, Wang Y, Yu B. Mechanical stretch inhibits mesenchymal stem cell adipogenic differentiation through TGFβ1/Smad2 signaling. J Biomech. 2015 Oct 15;48(13):3665-71.

5. Case N, Thomas J, Xie Z, Sen B, Styner M, Rowe D, Rubin J. Mechanical input restrains PPARγ2 expression and action to preserve mesenchymal stem cell multipotentiality. Bone. 2013 Jan;52(1):454-64.

6. Hime G and Abud H (eds.), Transcriptional and Translational Regulation of Stem Cells, Advances in Experimental Medicine and Biology 786, DOI 10.1007/978-94-007-6621-1_12, © Springer Science+Business Media Dordrecht 2013: pag. 213-219.

7. Pownall ME, Gustafsson MK, Emerson CP Jr. Myogenic regulatory factors and the specification of muscle progenitors in vertebrate embryos. Annu Rev Cell Dev Biol. 2002;18:747-83.

8. Li Y, Ramcharan M, Zhou Z, Leong DJ, Akinbiyi T, Majeska RJ, Sun HB. The Role of Scleraxis in Fate Determination of Mesenchymal Stem Cells for Tenocyte Differentiation. Sci Rep. 2015 Aug 20;5:13149.
9. Liu H, Zhang C, Zhu S, Lu P, Zhu T, Gong X, Zhang Z, Hu J, Yin Z, Heng BC, Chen X, Ouyang HW. Mohawk promotes the tenogenesis of mesenchymal stem cells through activation of the TGFβ signaling pathway. Stem Cells. 2015 Feb;33(2):443-55.
10. Guerquin MJ, Charvet B, Nourissat G, Havis E, Ronsin O, Bonnin MA, Ruggiu M, Olivera-Martinez I, Robert N, Lu Y, Kadler KE, Baumberger T, Doursounian L, Berenbaum F, Duprez D. Transcription factor EGR1 directs tendon differentiation and promotes tendon repair. J Clin Invest. 2013 Aug;123(8):3564-76. doi: 10.1172/JCI67521. Epub 2013 Jul 25.
11. Araújo JAM, Hilscher MM, Marques-Coelho D, Golbert DCF, Cornelio DA, Batistuzzo de Medeiros SR, Leão RN, Costa MR. Direct Reprogramming of Adult Human Somatic Stem Cells Into Functional Neurons Using Sox2, Ascl1, and Neurog2. Front Cell Neurosci. 2018 Jun 8;12:155.
12. Schäck L, Budde S, Lenarz T, Krettek C, Gross G, Windhagen H, Hoffmann A, Warnecke A. Induction of neuronal-like phenotype in human mesenchymal stem cells by overexpression of Neurogenin1 and treatment with neurotrophins. Tissue Cell. 2016 Oct;48(5):524-32.
13. Marrelli M, Paduano F, Tatullo M. Human periapical cyst-mesenchymal stem cells differentiate into neuronal cells. J Dent Res. 2015 Jun;94(6):843-52.
14. Bjerre L, Bünger CE, Kassem M, Mygind T. Flow perfusion culture of human mesenchymal stem cells on silicate-substituted tricalcium phosphate scaffolds. Biomaterials. 2008 Jun;29(17):2616-27.

CHAPTER 2.1: Purified fluorescent proteins as tools for nuclear import dynamics measure

Summary

Among the intracellular dynamics, the nuclecytoplasmic transport remains a challenging phenomenon very difficult to quantify and thus, to completely understand. With the purpose to engineer a fluorescent tool to measure the nuclear import rate in different MSC mechanical stress conditions, I generated two fluorescent variants of a myogenic transcription factor, MyoD, able to be delivered as biologically active proteins. Thus, I fused MyoD to the Tat-GFP, able to freely pass the plasmatic membrane, or to the (-30)GFP that can be cell internalized when complexed with cationic lipids. I finally purified the recombinant proteins Tat-GFP-MyoD and (-30)GFP-MyoD.

Fluorescence confocal microscopy showed that Tat-GFP-MyoD failed to reach nuclear localization while (-30)GFP-MyoD resulted highly transduced into the nucleus. Analyses of fluorescence recovery after photobleaching (FRAP) kinetics confirmed that (-30)GFP-MyoD is suitable for nucleocytoplasmic shuttling and protein mobility measurement. In order to quantify (-30)GFP-MyoD activity, we performed analyses of real time-PCR gene expression of target genes of MyoD. Genetic assays showed an inhibitory effect of (-30)GFP on MyoD transcription promoting activity.

Summarizing our results, we found that (-30)GFP-MyoD was a good fluorescent tool for nucleocytoplasmic transport assessment but with evident limitations related to the influence of the (-30)GFP on MyoD functionality.

Introduction

The choice of the correct fluorescent label in a study of intracellular dynamics is critical. In the case of nuclear import flux study, the TF has to be fused to a fluorescent marker to make it detectable. The inner ring of the nuclear pore is about 40 nm in unstretched conditions and constitutes a barrier for diffusion of molecules bigger than 40-60kDa. In order to avoid alteration of TF nucleocytoplasmic transport, the choice of the fusion probe has to take into account not just the fluorophore optical properties but specially its physical dimension. For these reasons, the most used fluorescent tails in nucleocytoplasmic transport research are based on the structure of the original GFP (purified from *Aequorea victoria*). The native structure has a molecular weight of about 26.9 kDa and is composed of 238 amino acids. It is a small protein and it protects the chromophore in the inner part (Fig. 2.1.1).

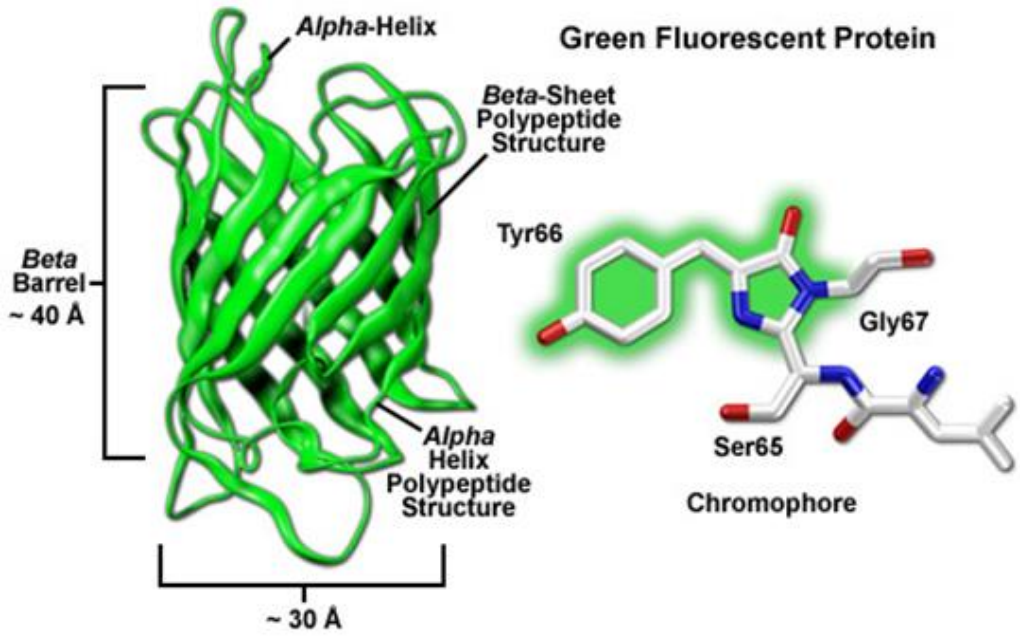

Fig 2.1.1 Graphical representation of the 3D jellyfish green fluorescent protein. Alpha-Helix and Beta Barrel are the secondary structures characterizing the 3D structure. The chromophore is the specific group of atoms responsible of the light absorption, and the

consequent electron excitation and fluorescence emission. Source: http://zeiss-campus.magnet.fsu.edu/articles/probes/fpintroduction.html

The chromophore in the GFP is a tripeptide (serine, tyrosine, and glycine at positions 65-67) and it is responsible of fluorescence, defined as emission of photons, caused by absorption of light, for which the average lifetime of the excited atoms or molecules is less than about 10^{-8} seconds. The best quality of this protein is that it is very easy to engineer changing its optical and functional properties.
While most of the GFP mutants are modified in the chromophore tripeptide in order to alter the optical properties (e.g. yellow fluorescent protein), a recent mutant variant showed a functional variation to the intracellular delivery method [1].
The most common way to introduce an exogenous recombinant protein into the cell is DNA transfection method (Fig 2.1.3A). This strategy requires the internalization of a plasmid containing the DNA sequence codifying for the recombinant protein. Once delivered in the cell, the DNA sequence is recognized by the cell transcription and translation machinery which produces and folds the recombinant protein within 24-48 hours. However, in the last decades it has been developed a technology that reduces the time required to achieve the recombinant protein into cells and improves the control on the amount of the delivered protein. This technique is called protein transduction and includes all the methods by which proteins can penetrate into cells [1-5]. By this strategy it is possible to detect the protein within few hours into the physiological localization. For instance, to let a protein pass the plasmatic membrane it could be fused to a protein transduction domain (PTDs), such as HIV-1 Tat, pAntp43-58, and polyarginine (R11) [2-4]. All these peptides are characterized by the presence of positively charged amino acids which can interact with the negative charges characterizing the plasmatic membrane. This

interaction stimulates the macropinocytosis mechanism and the entrapping of the recombinant protein into an endosomal vesicle (Fig. 2.1.3B). The most used protein transduction domain is the HIV-1 Tat peptide, composed by 12 amino acids (GRKKRRQRRRPQ).

A recent GFP mutant that actually captured our attention is a negatively supercharged GFP, (-30)GFP [1,5]. The (-30)GFP has been created from a starting GFP (stGFP) in which Lawrence and colleagues substituted 15 surface amino acids with 15 negatively charged residues (Glutamate and Aspartate) (Fig. 2.1.2).

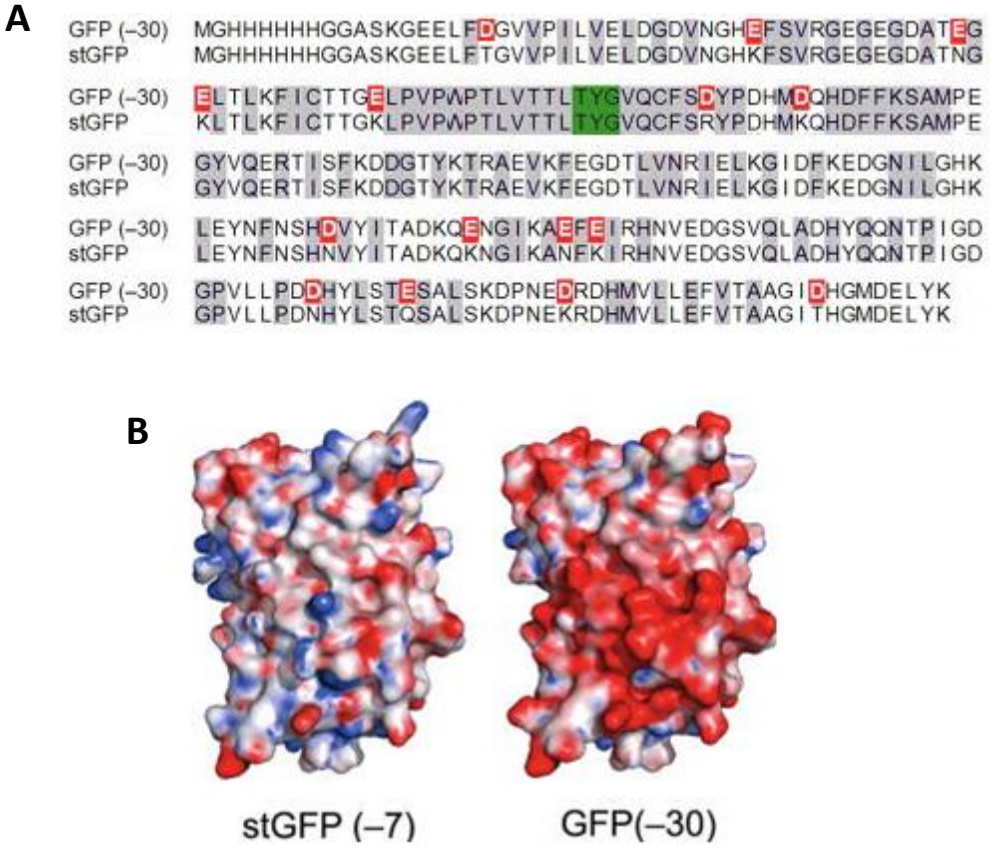

Fig. 2.1.2 Negatively supercharged GFP. (A) aminoacidic sequences of GFP variants. Modified negative residues are highlighted in red and chromophore tripeptide is highlighted in green; (B) electrostatic surface potential of starting GFP (-7) and negatively supercharged GFP (-30). Adapted from ref. [1].

Their hypothesis was that highly anionic proteins could be intracellular delivered by the same electrostatics-driven complexation of cations, analogous to nucleic acids delivery. They demonstrated that (-30)GFP also fused to other proteins (e.g. CRE, Cas9) could be delivered after complexation with reagents commonly used for DNA or RNA transfection (e.g. lipofectamines) (Fig. 2.1.3C). This form of GFP could be transduced in *in vitro* and *in vivo* models with good transduction efficiency, fluorescence properties maintenance and control of the delivered protein amount.

Protein transduction technologies have not been used to engineer probes for nucleocytoplasmic transport measurement. In this work I selected two forms of GFP belonging to the protein transduction technology group ((-30)GFP and GFP fused to HIV-1 Tat peptide) as labels to measure nuclear import rate of TFs.
I screened different MSCs relevant TFs (Osterix, MyoD, Scleraxis, Ascl1) in order to select the best for our purpose. I chose MyoD to engineer for further experiments and I proceeded fusing it to the two forms of GFP. I evaluated protein transduction efficiency and nuclear localization by fluorescence confocal microscopy. Nucleocytoplasmic shuttling was assessed by FRAP measurement. I finally assessed the functionality of the recombinant proteins by analyzing real-time PCR target gene expression levels.

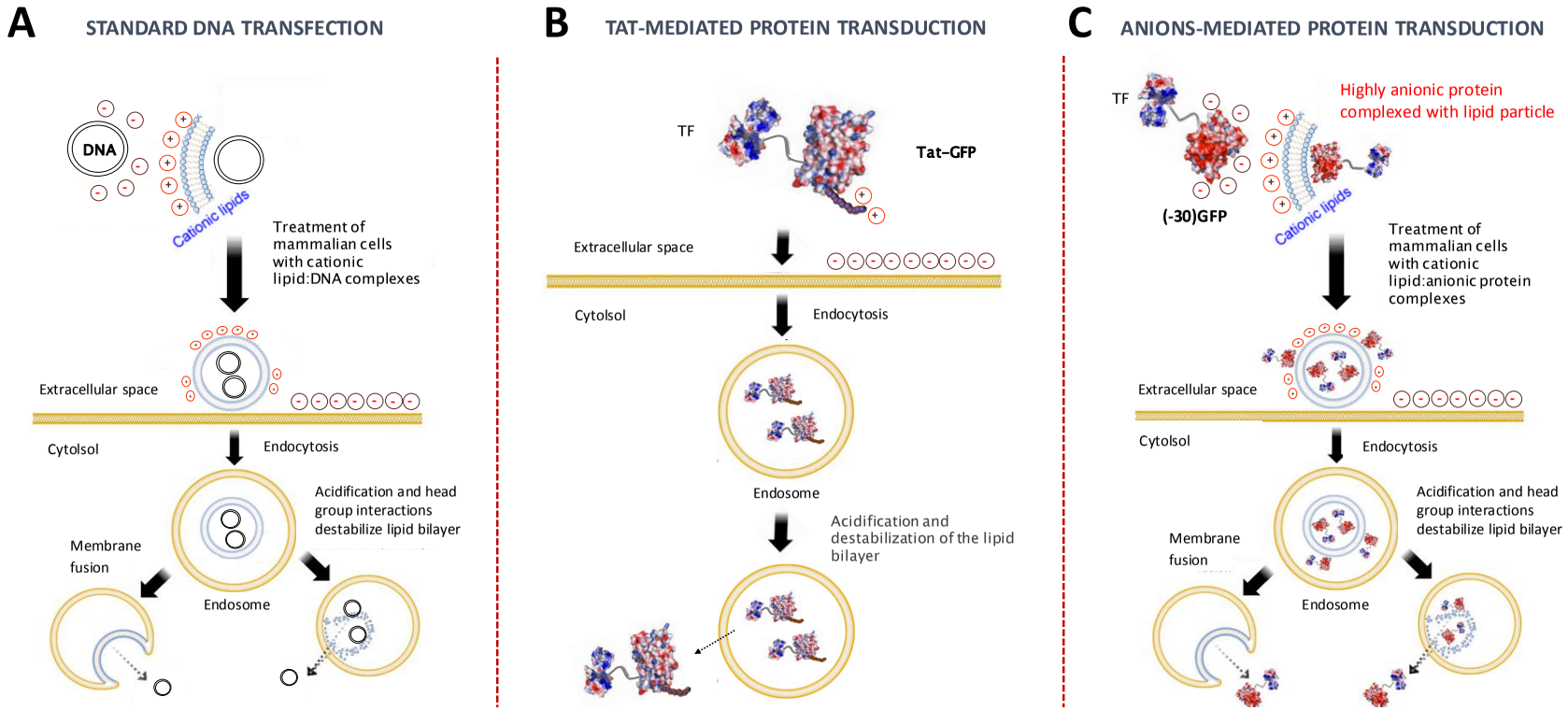

Fig 2.1.3 Molecular intracellular delivery. (A) standard cationic lipids-mediated DNA transfection of a recombinant plasmid codifying for GFP-TF. (B) intracellular delivery mediated by the Tat peptide fused to the GFP-TF; (C) intracellular delivery mediated by the complexation of the (-30)GFP-TF with cationic molecules. TF: transcription factor. Adapted from [5].

Results

Engineering and expression of constructs

In order to choose which factor among the promoters of the differentiation pathways was best to engineer, I selected four transcription factors involved in the earlier stages of different MSC differentiation fate (Table 2.1.1). The preliminary selection was based on the biological and biochemical properties, such as dimension and molecular weight. MyoD is one of the first factor activated during myogenesis, Ascl1 is involved in triggering neurogenesis, scleraxis (Scx) in tenogenesis and osterix (Osx) is one of the main promoters of the osteogenic differentiation. Comparing tables 2.1 and 2.1.1, we can see that MyoD and Osx are two selected factors already assessed for mechanotranscription mechanism while Ascl1 and Scx have not been studied in this context.

Transcription Factors	Differentiation pathways	Dimension	Molecular weight (MW)
MyoD	myogenesis	318 aa	34 kDa
Ascl1	neurogenesis	231 aa	25 kDa
Scleraxis	tenogenesis	207 aa	22 kDa
Osterix	osteogenesis	428 aa	45 kDa

Table 2.1.1. Transcription factors selected for their biochemical and structural properties.

In order to select the best factor for further experiments, I fused the supernegative GFP, (-30)GFP, to each factor and I subcloned the recombinant constructs in the bacterial pRSET A plasmid (Suppl. Fig.

2.1.1). The expression of the recombinant proteins were optimized in BL21(DE3)pLysS *E.coli* cells and the protein purification was based on the presence of the N-terminal His-Tag (nickel affinity chromatography, as detailed in “Methods”, “Protein purification” section). To evaluate the quality of the purified proteins, purification products were separated by SDS-PAGE Gel Electrophoresis. The protein separation pattern should show the characterizing band of the recombinant protein at the specific molecular weight. Non-specific bands could represent degradation fragments of the protein of interest or *E. coli* contaminants. In our experiment the expected characterizing bands were about: 64.3 kDa for (-30)GFP-MyoD, 59.9 kDa for (-30)GFP-Ascl1, 56.9 kDa for (-30)GFP-Scx and 74.9 kDa (-30)GFP-Osx. As shown in Fig. 2.1.4 (-30)GFP-MyoD resulted well expressed with a low level of degradation. The band corresponding to the (-30)GFP-MyoD is slightly higher than the correspondent molecular weight marker reference. (-30)GFP-Ascl1 showed a very weak signal corresponding to the correct band at about 60 kDa. (-30)GFP-Scx resulted partially degraded generating fragments with a lower molecular weight respect to the expected. (-30)GFP-Osx showed different level of degradation with a net scission between (-30)GFP and Osx confirmed by the two biggest bands corresponding to the two molecular weight of the molecules, 34.9 kDa (because of the presence of N-Terminal His-Tag) and 45 kDa respectively.

At the end of different steps of expression optimization and observing protein separation patterns, I selected MyoD as the best factors to be engineered for our purposes.

In order to evaluate another form of protein transduction-based fluorescent transcription factor, I fused MyoD to another GFP variant bound to the Tat-peptide and the N-terminal His-Tag (Suppl. Fig. 2.1.1). As in the case of (-30)GFP-MyoD I subcloned Tat-GFP-MyoD

(MW=67.3 kDa) into the pRSET A plasmid in order to express the recombinant protein into bacteria and purify the protein product.

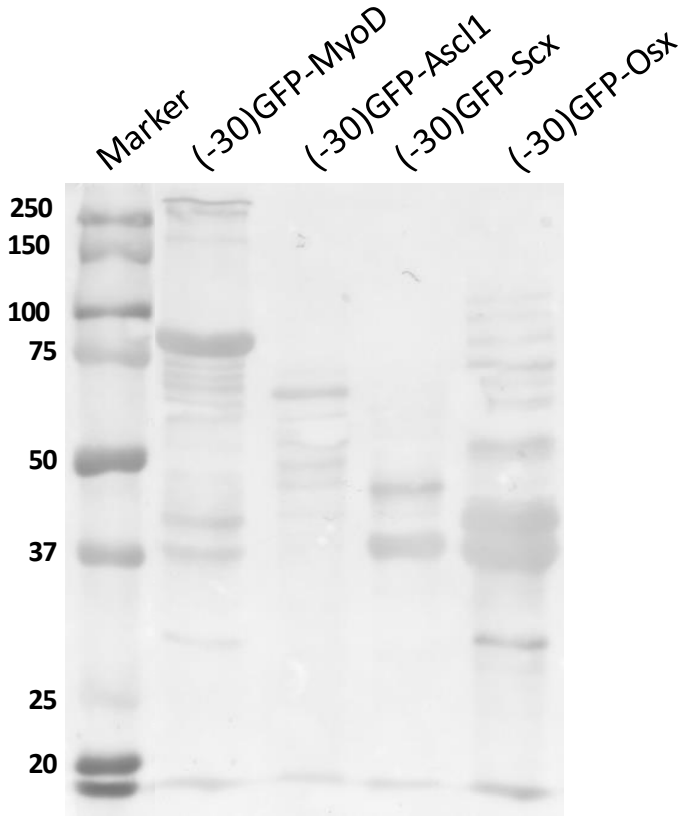

Fig. 2.1.4 SDS-PAGE Gel electrophoresis and Ponceau red staining of purified recombinant (-30)GFP-MyoD (MW=64.3 kDa), (-30)GFP-Ascl1 (MW=59.9 kDa), (-30)GFP-Scleraxis (MW=56.9 kDa), (-30)GFP-Osterix (MW=74.9 kDa).

Protein transduction efficiency and construct localization

To evaluate the intracellular localization of Tat-GFP-MyoD and (-30)GFP-MyoD in living MSCs, I first assessed protein transduction efficiency by fluorescence confocal microscopy.

While in the case of Tat-based proteins the delivery procedure is standardized, (-30)GFP-MyoD required an optimization of the procedure. Since the supernegative GFP penetrates the plasmatic membrane when complexed with cationic molecules, I tested four

different transfection reagents, two lipid-based (Lipofectamine MessengerMAX and Lipofectamine 3000) and two non-liposomal reagents (jetPRIME and FugeneHD) (Suppl. Table 2.1.1). Independently from the type of reagents, the common procedure steps involved a first passage of serum-free cell conditioning, followed by the addition of the chemical cocktail containing the protein complexed to the transfection reagents (Suppl. Table 2.1.2). The medium was replaced after 3 hours and the optimal fluorescence detection was reached between 3-4 hours from the addition of the protein. I analyzed protein delivery by fluorescence confocal microscopy and I calculated protein transduction efficiency as the ratio of transduced nuclei on the total amount of nuclei stained with Hoechst dye (Fig. 2.1.5). As shown in Fig. 2.1.5B, the best protein transduction efficiency was reached by transduction with Lipofectamine MessengerMAX and jetPRIME that showed a comparable effect. The discriminating element in the choice between the two reagents was related to the protein aggregates amount that is appreciable in Fig. 2.1.5A. In the case of transduction with jetPRIME the use of the required specific buffer caused excessive protein aggregation worsening the quality of the fluorescence detection. For this reason the selected transfection reagent for further protein transduction of (-30)GFP-MyoD was Lipofectamine MessengerMAX.

Once set the condition for (-30)GFP-based transduction, I compared the protein transduction efficiency and the intracellular localization of (-30)GFP-MyoD and Tat-GFP-MyoD with respect to a standard GFP (pmaxGFP) transfected with classic DNA transfection procedure.

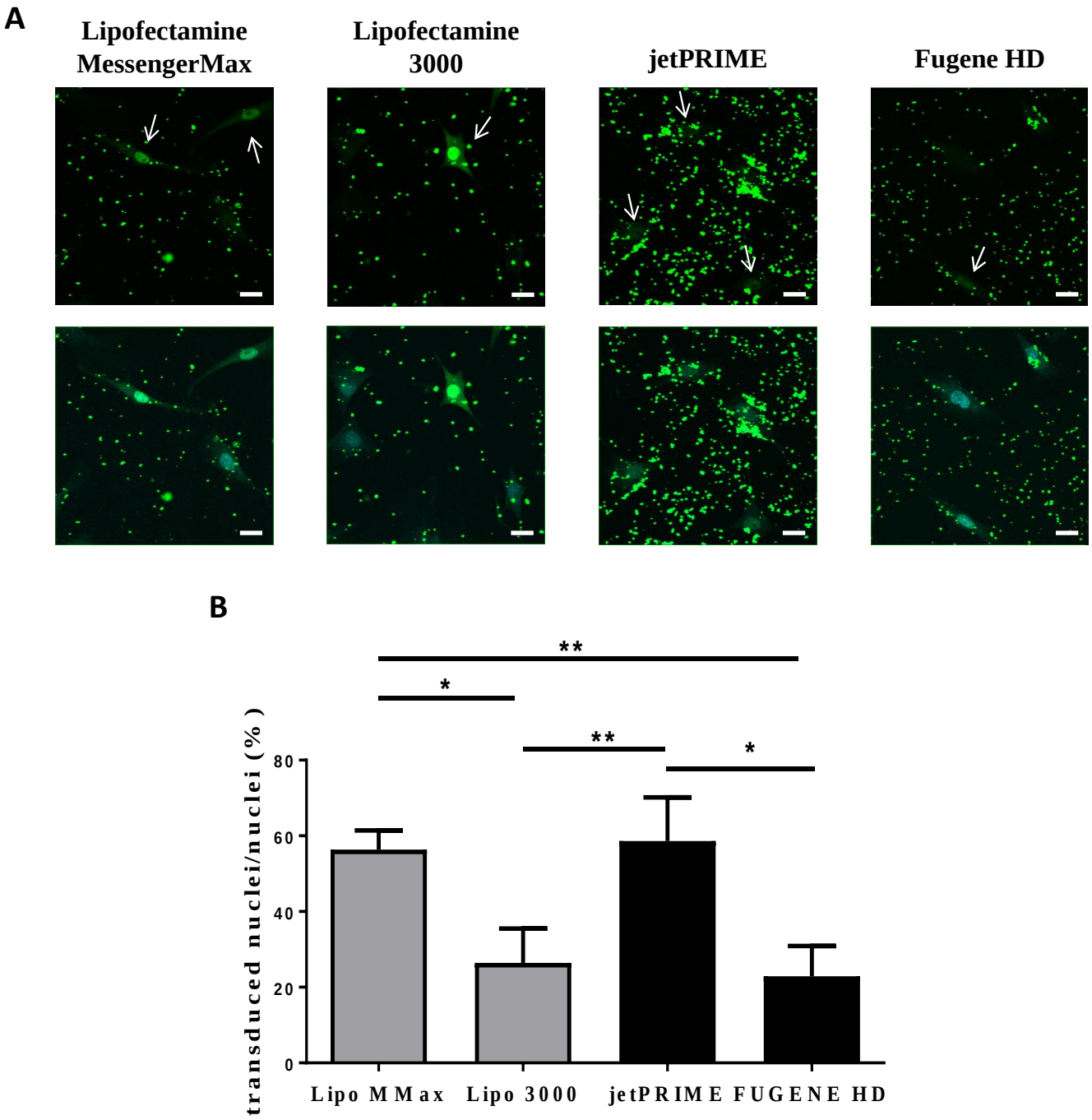

Fig. 2.1.5 Comparison of (-30)GFP-MyoD transduction efficiency using different transfection reagents. (A) Confocal images of transduced MSC nuclei highlighted by the white arrows (upper panels); the same images superimposed to Hoechst dye nuclear stain (lower panels). Scale bar: 20 μm. (B) Graphical representation of the comparison of the protein transduction efficiency. Data were analyzed by one way-ANOVA test followed by Tukey's multiple comparisons test. Data are expressed as mean ± SD.

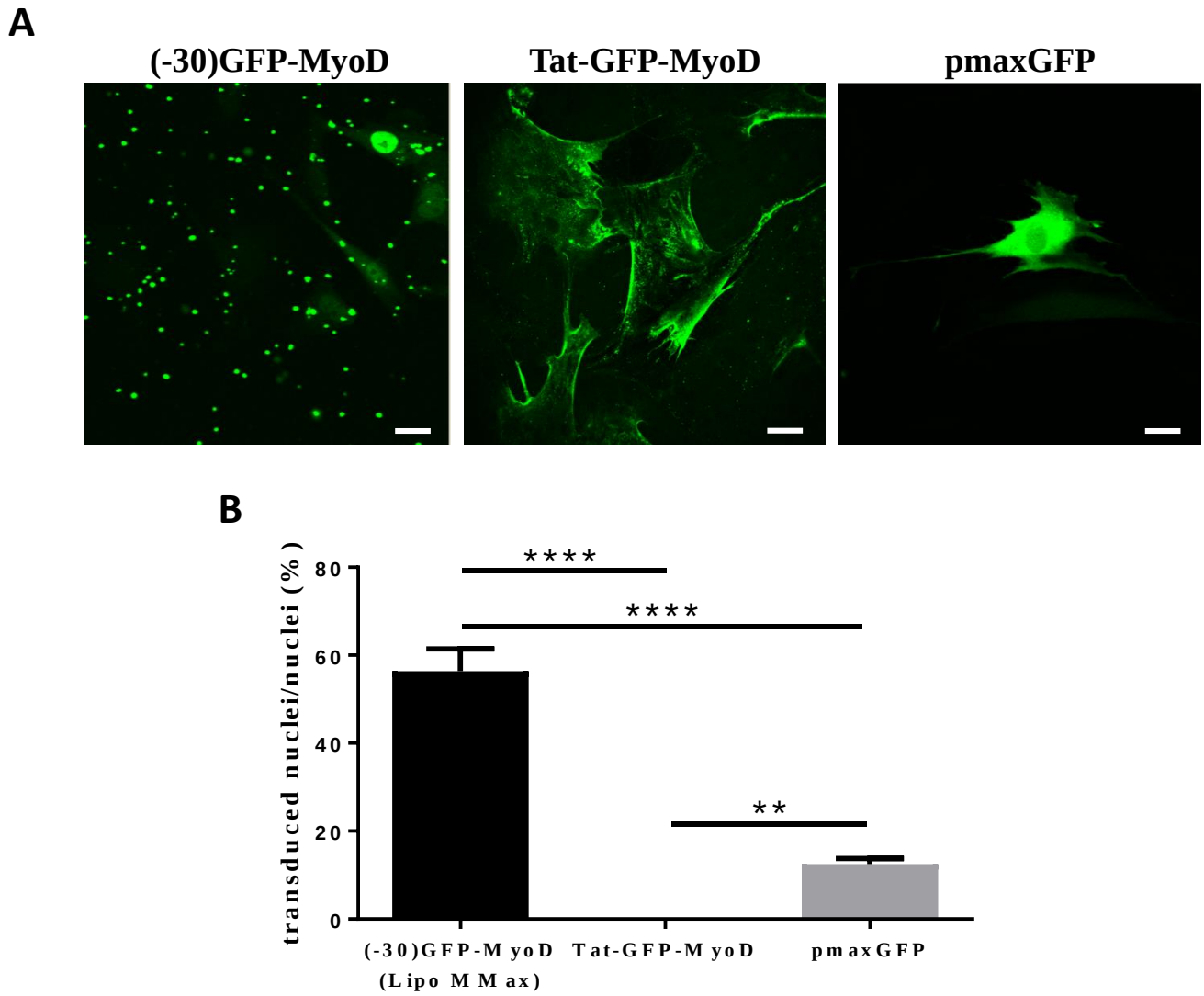

Fig. 2.1.6 Comparison of protein transduction of (-30)GFP-MyoD, Tat-GFP-MyoD and DNA transfection of pmaxGFP. (A) Confocal images of MSCs transduced (with (-30)GFP-MyoD or Tat-GFP-MyoD) or transfected with pmaxGFP . Scale bar: 20 μm. (B) Graphical representation of molecule internalization efficiency. Data were analyzed by one way-ANOVA test followed by Tukey's multiple comparisons test. Data are expressed as mean ± SD.

As shown in Fig. 2.1.6A, (-30)GFP-MyoD showed a predominant nuclear localization that corresponded to the physiological MyoD subcellular location. Tat-GFP-MyoD appeared to be stuck with the plasmatic membrane and failed to reach the nucleus.

As expected the intracellular localization of pmaxGFP is distributed throughout the whole cell with a predominance in the cytoplasm. The evaluation of molecule internalization efficiency (Fig. 2.1.6B) highlighted the great potential of the supernagative GFP-based protein transduction respect to both Tat-peptide based transduction and DNA transfection.
For intranuclear detection failure, I proceeded with the exclusion of the Tat-GFP-MyoD for further analyses and I continued with the protein transduction-based (-30)GFP-MyoD.

FRAP measurement

Once (-30)GFP-MyoD was validated for intracellular delivery and nuclear localization, it was then assessed for nucleocytoplasmic transport measurement. (-30)GFP-MyoD was used as tool for preliminary FRAP analyses of nuclear and cytoplasmic compartments. Since FRAP measurement requires great amount of intracellular fluorescent protein sufficiently distributed in both the cytosol and the nucleus, (-30)GFP-MyoD transduction was not optimal for this technique because it delivered a low concentration of protein that quickly localized to the nucleus. Therefore, I decided to transfect MSCs with an eukaryotic plasmid coding for the same (-30)GFP-MyoD (see Suppl. Fig. 2.1.2). This solution allowed a continuous production of the protein into the cytosol and a sufficient amount of fluorescent molecules to bleach and detect it. Since the aim of my Ph.D. project was to engineer a tool to study nuclear import fluxes into MSCs subjected to different mechanical conditions, we cultured MSCs in both 2D and 3D conditions. Thus, MSCs were growth into the nichoid cell culture scaffold (Suppl. Fig. 2.1.3) and on to standard 2D cell culture substrates. As described in Chapter 1, while 2D cell culture substrates

maximize cell adhesion and cell stretching, nichoid 3D scaffold promotes isotropic cell adhesion and nuclear roundish shape.

The fluorescence of the nuclear region (region of interest, ROI) of MSCs expressing (-30)GFP-MyoD was photobleached as described in “Methods”, “FRAP kinetics analysis” section. The fluorescence recovery was than recorded by time-lapse acquisitions and it corresponds to the inner flux of unbleached fluorescent molecules from the cytoplasm to the nuclear region, in equilibrium with the outer flux of the bleached molecules. Fig 2.1.7 shows the mono-exponential fit of the recovery curves of the two MSC populations: cells with spread or roundish nuclei. The characteristic time, τ value, of each curve is highlighted by a vertical line. It corresponds to the time necessary to reach the 66% of the maximum intensity, and it is the parameter that we used to evaluate the speed of the (-30)GFP-MyoD nuclear translocation process. Results from this preliminary study of nucleocytoplasmic transport were very encouraging. In fact τ value of MSCs cultured into the nichoid (roundish nuclei) was 23.5% higher than τ value of spread nuclei. This parameter indicated that fluorescent molecules in roundish nuclei required more time to reach the equilibrium between nuclear and cytoplasmic fluorescence. Then I used the τ value to define a new parameter (F) that is representative of the nuclear import rate. (See “Methods”, “FRAP kinetics analysis” section). This parameter reinforced and clarified the results suggesting that (-30)GFP-MyoD was imported into spread nuclei at an higher rate (+41.5%) respect to roundish nuclei. These data are perfectly in line with the hypothesis of the NICHOID project. In fact, these results suggested that stretched cells with spread nuclei imported factors at a higher rate than cells subjected to isotropic cell adhesion and with more roundish nuclei.

These preliminary data also indicated that (-30)GFP-MyoD is a recombinant protein suitable for nucleocytoplasmic shuttling measurements and NICHOID hypothesis validation.

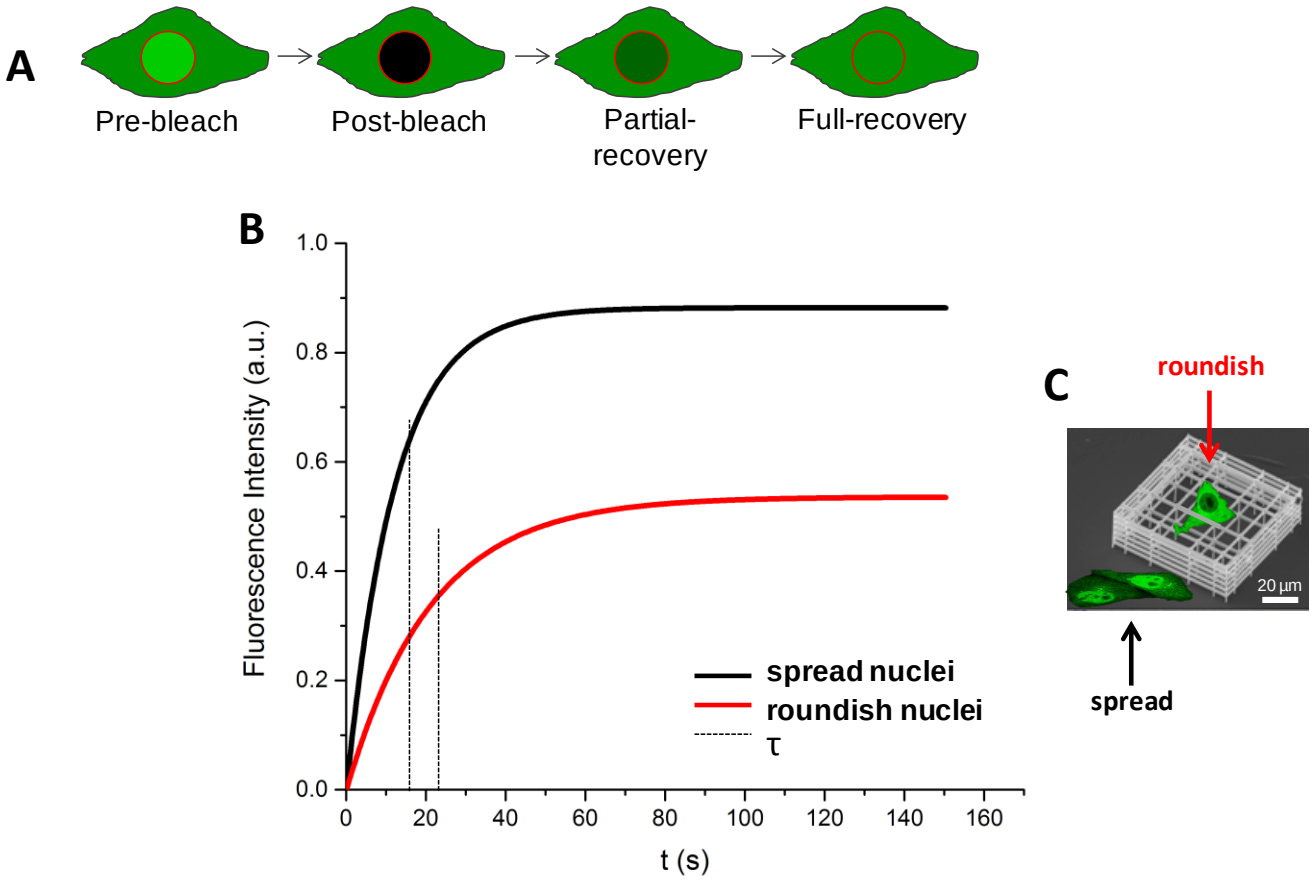

$\tau_{spread\ nuclei}$= 16.31 ± 0.56 s $F_{spread\ nuclei}$= 2.9 ± 1.3

$\tau_{roundish\ nuclei}$ =21.23 ± 1.57 s $F_{roundish\ nuclei}$ = 1.7 ± 0.6

Fig. 2.1.7 (A) Graphical representation of the fluorescence perturbation within the FRAP measurement. The ROI is highlighted in red and corresponds to the nuclear area. (B) FRAP analysis of MSCs expressing (-30)GFP-MyoD. n=10. (C) Graphical representation of MSC populations: MSCs cultured into 2D culture substrate showed more spread nuclei respect to MSC nuclei growth into nichoid scaffolds (roundish nuclei). τ value refers to the characteristic time and F index is representative of the nuclear import rate.

Transcription promoting activity assay

In order to verify if (-30)GFP-MyoD maintained the transcription promoting activity of MyoD, I investigated the mRNA expression levels of target genes of MyoD.

I started with the assay of the transcription promoting activity of the native MyoD without (-30)GFP. Because the native MyoD protein is not able to freely pass the plasmatic membrane, the common way to internalize the protein into the cell is by DNA transfection methods. Thus, I first subcloned the sequence coding for MyoD into an eukaryotic plasmid and transfected the recombinant vector into MSCs by standard DNA transfection procedures (Suppl. Fig. 2.1.2).

In order to analyze the MyoD activity, I selected four target genes whose transcription is promoted by MyoD: Myogenin (Myog), Creatin Kinase M-Type (CKM), Desmin and Cadherin 15 (Cdh15). I extracted total mRNA from MSCs overexpressing MyoD (MSC-MyoD) and untransfected MSCs (MSC, control group) at sequential time points after DNA transfection (24h, 48h, 72h, 96h). Finally, I assessed mRNA gene expression levels by relative quantitative real-time PCR. As shown in Fig. 2.1.8, MSC-MyoD showed higher mRNA levels of all target genes with respect to MSC basal gene expression levels. Myog and CKM are the target genes that were clearly expressed at higher level than control. In both cases the time point where the expression levels seemed to reach a stabilized expression was 72 h. Cdh15 and Desmin showed a reduced increase and a delayed response in time. For these reasons Myog and CKM were selected for further investigations.

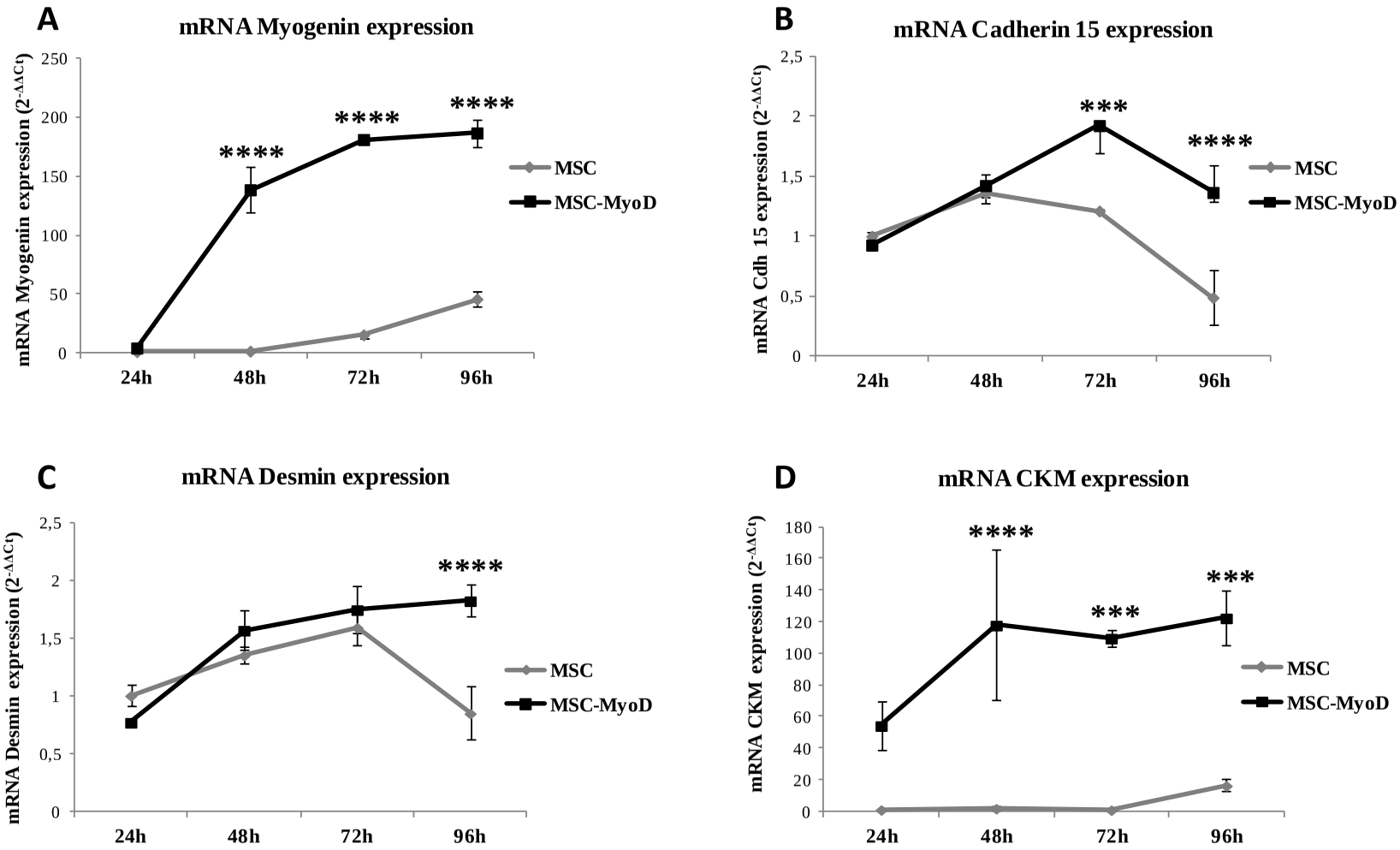

Fig 2.1.8 Gene expression real-time PCR of target genes promoted by MyoD activity at sequential time points. (A) Myogenin; (B) Cadherin 15; (C) Desmin; (C) Creatin Kinase, M-type (CKM). Untrasfected MSC (control group) were compared with MSC overexpressing MyoD at 24h, 48h, 72h and 96h. Data were analyzed by two way-ANOVA test followed by Tukey's multiple comparisons test. Data are expressed as mean ± SD. Significance symbols refer to comparison with the respective control.

In order to analyze (-30)GFP-MyoD activity I transduced MSCs with the supernegative transcription factor complexed with Lipofectamine messengerMAX. Following the literature [6], I extracted total mRNA 9 hours after protein addition, or, in other words 6 hours after optimal protein nuclear detection (activated state). As calibrator of (-30)GFP-MyoD, I transduced MSCs with a form of (-30)GFP without MyoD (Suppl.Fig. 2.1.1).

I used MSCs transiently transfected with the plasmid coding for the native MyoD (pMyoD) as positive control. As calibrator for pMyoD, I used a plasmid coding for a protein with a similar dimension but without a regulatory function, such as transcriptional activity. I chose a commonly used enhanced form of GFP (pEGFP) kindly provided by Professor Alessandro Negro (Dept. Biomedical Sciences, University of Padua).

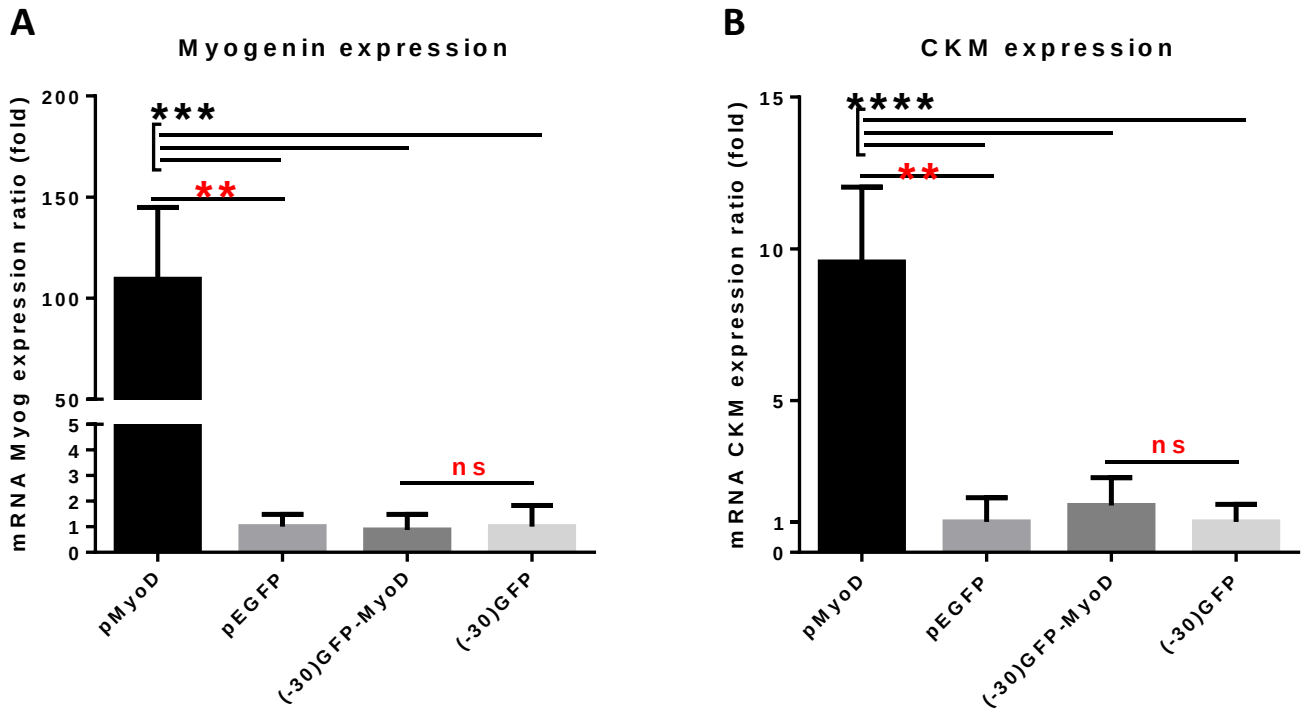

Fig. 2.1.9 (-30)GFP-MyoD transcription promoting activity. In both graphs of (A) mRNA Myog expression and (B) mRNA CKM expression, are represented two experimentally-paired

groups. pMyoD and pEGFP represent MSCs DNA transfected and lysed for RNA extraction at 72 hours. (-30)GFP-MyoD and (-30)GFP indicate MSCs transduced with anionic protein:cationic lipid complexes and lysed at 9 hours. Data were analyzed by one way-ANOVA test followed by Tukey's multiple comparisons test and by Student's t-test for comparison between two experimental-paired groups. Data are expressed as mean ± SD. Significance symbols highlighted in red refer to Student's t-test. Significance symbols in black refer to one way-ANOVA test.

As shown in Fig. 2.1.9 (A), the level of expression of mRNA Myog in MSCs transduced with (-30)GFP-MyoD is closely similar to MSCs transduced with (-30)GFP without MyoD. The higher signal of Myog expression in MSCs transfected with pMyoD excluded a technical problem. Fig. 2.1.9B shows mRNA CKM expression and reproduces the same scheme of results illustrated for Myog. Overall, Fig. 2.1.9 suggests an inhibitory effect of (-30)GFP on MyoD activity.

To deepen the last observations on the inhibition of the transcription promoting activity of MyoD, I decided to subclone (-30)GFP-MyoD and (-30)GFP sequences into an eukaryotic vector (Suppl. Fig. 2.1.2). Using plasmids coding for the supernegative proteins and DNA transfection instead of protein transduction would eliminated the experimental bias related to the impossibility to compare the functionality of the native MyoD and (-30)GFP-MyoD. Furthermore, I could verify if the inhibitory effect was intrinsically related to the protein structure or could be attributable to protein manipulation steps. Thus, I transfected MSCs with pMyoD, pEGFP (calibrator of pMyoD), p(-30)GFP-MyoD, p(-30)GFP (calibrator of (-30)GFP-MyoD). As shown in Fig. 2.1.10, the inhibitory effect of (-30)GFP on MyoD activity was confirmed and both gene expression levels of Myog and CKM were comparable to basal expression of MSCs not overexpressing MyoD (p(-30)GFP or pEGFP). These data suggested that the inhibitory effect

of (-30)GFP on MyoD activity was independent from the delivery method and specific to the protein construct.

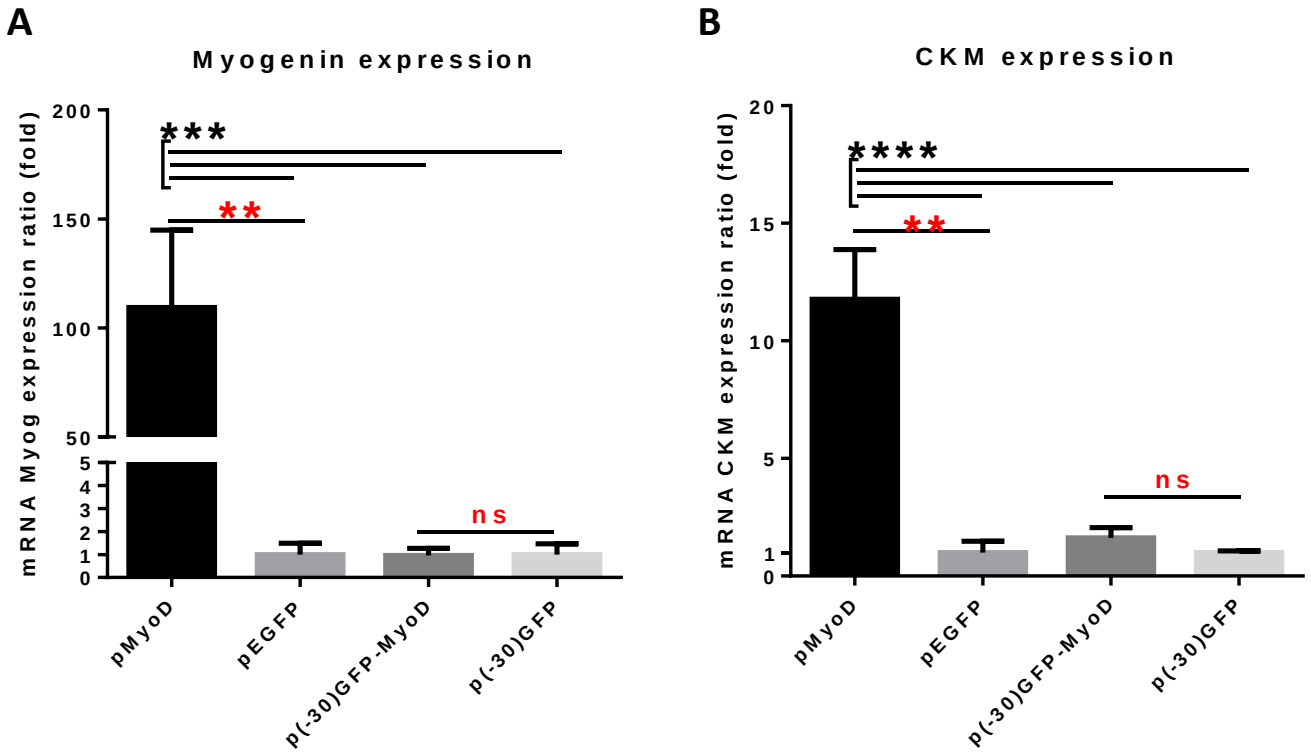

Fig. 2.1.10 (-30)GFP-MyoD transcription promoting activity. MSCs were transfected with DNA plasmids: pMyoD, pEGFP, p(-30)GFP-MyoD or p(30)GFP. Each MSC population was analyzed for (A) mRNA Myog expression (B) mRNA CKM expression. Data were assessed by one way-ANOVA test followed by Tukey's multiple comparisons test and by Student's t-test for comparison between two groups. Data are expressed as mean ± SD. Significance symbols highlighted in red refer to Student's t-test. Significance symbols in black refer to one way-ANOVA test.

The investigations on transcription promoting activity highlighted some limitations of (-30)GFP-MyoD. The supernegative version of MyoD resulted a suitable tool for nuclear import measurement in terms of protein transduction efficiency, nuclear localization and nucleocytoplasmic transport evaluation. The inhibitory effect resulted from real-time PCR assays showed a limitation concerning possible insights into downstream biochemical and cellular mechanisms.

Discussion

The discovery of peptides able to enter cells was first reported to late eighties with the demonstration that Tat protein could pass cell membrane to allow virus gene expression [8, 9]. In last three decades, the huge advancements in development of protein transduction domains stimulated researchers to apply protein transduction technologies, mainly Tat-based, to *in vivo* and *ex vivo* treatments [10-12]. Furthermore, great interest arouse also around Tat-based drug delivery systems [13]. Zuris and colleagues demonstrated that it exits another method for protein delivery and it is based on electrostatics-driven complexation. They created a supernegative (-30)GFP as new protein transduction element to mediate the internalization of other molecules [5]. Despite the PTDs and the system proposed by Zuris offer a reduced time of internalization and an increase of control in intracellular protein delivery, protein transduction technologies have not yet been used for nucleocytoplasmic transport measurement. Thus, I decided to test Tat-mediated transduction and supernegative GFP as delivery methods to internalize fluorescent tools and to measure real time nuclear import rate.

In our system, Tat-mediated transduction method failed because Tat-GFP-MyoD was not able to reach the nucleus. The reasons of this intracellular detection failure were not clear and should be further studied. It could be due to a specific structural problem of our construct that allows the interaction of the protein with the plasmatic membrane but does not make possible the process of entering the cell and thus, the nucleus. In addition to this hypothesis, a further negative influence to the intracellular uptake of the protein could be given by the

concentration-dependent properties of the Tat-mediated system. It has been demonstrated that the extracellular protein concentration regulates the intracellular equilibrium [17]. Changes in protein concentration, i.e. washing steps, could cause the delocalization of the protein and the exit from the cells. Fluorescence detection by confocal microscopy forcedly requires washing steps to remove exceeding fluorescent background. These washing steps could contribute to destabilize the intracellular protein localization. So far, the only method used to study the nucleocytoplasmic transport of Tat-based proteins was based on the transfection of Tat-fused molecules as DNA plasmid [14, 16] nullifying the advantages of protein transduction technology. In summary, Tat-GFP-MyoD could not be used for our nuclear import studies and I had to exclude it from our experiments.

The supernegative GFP fused to the transcription factor MyoD showed encouraging results but with some limitations. Fluorescence confocal microscopy showed that (-30)GFP-MyoD reached the optimal protein efficiency with cationic liposomes as demonstrated by Zuris and colleagues [5]. The fluorescent TF reached the physiological nuclear localization within 3 hours. Unfortunately, real-time PCR assay highlighted a specific inhibitory effect of (-30)GFP on MyoD activity. In the original work (-30)GFP was validated as fusion protein with Cre, Cas9 or Tale (Transcription activator-like effector). During the DNA vector design, I maintained the same structure and linker length of Zuris' work. Thus, the inhibitory effect could be related to the characteristic of MyoD and in particular to the domain characterizing the TF. An hypothesis is that the positive charges characterizing the DNA binding domain could interact with (-30)GFP and interfere with MyoD activity. Molecular dynamics simulations may be a tool to unfold this unclear aspect (see Chapter 3). Despite of negative genetic

results, FRAP measurement performed with overexpressed (-30)GFP-MyoD showed standard output exponential curves and confirmed that the protein is suitable for protein localization and nucleocytoplasmic transport detection. In order to measure the nuclear import of (-30)GFP-MyoD delivered as purified protein, fluorescence correlation spectroscopy is an example of technique that would allow the measurement of lower amount of protein by the analysis of fluorescence intensity fluctuation.

In conclusion, (-30)GFP-MyoD is a protein transduction-based tool that reached the nuclear localization in few hours at an excellent protein transduction efficiency (>50%). This system offered the possibility of fluorescence detection and nucleocytoplasmic measurement within 3-4 hours. The inhibitory effect on the TF activity showed evident limitations related to the use of the tool for further insights about MyoD activity-dependent mechanisms.

Methods

Gene cloning. (-30)GFP sequence was amplified from pET-(-30)GFP-9xGGS-Cre-6xHis (Addgene, plasmid #32372) inserting in the primers specific restriction enzyme sites: *XbaI* (TCTAGA) site at 5’ of the forward primer and *BamHI* (GGATCC) *and NheI* sites at 5’ of in the reverse primer. Thus, the amplified gene codifying for (-30)GFP was than subcloned into the procariotic vector pRSET A (carrying the resistance to ampicillin) using the *XbaI* and *BamHI* sites of the vector multiple cloning site. The presence of *NheI* site ate the 5’ of the Reverse primer in the amplification of the (-30)GFP facilitated the subcloning of the transcription factors (MyoD, Osterix, Scleraxis, AscII)

codifying sequences into the plasmid pRSET A-(-30)GFP using *NheI* and *HindIII* (AAGCTT) sites (see Suppl. Fig. 2.1.1).
To obtain Tat-sfGFP-MyoD, MyoD was amplified with primers containing *BglII* (AGATCT) and *SalI HF* (GTCGAC) at the 5' of the forward and the reverse sequences respectively. Thus, using the *BglII* and *SalI HF* sites, the sequence was than subcloned into a recombinant pRSET A containing a sequence codifying for the superfolder GFP fuse to the Tat transduction domain (the vector was kindly provided by Professor Alessandro Negro, Department of Biomedical Sciences, University of Padua) (see Suppl. Fig. 2.1.1).
The sequences codifying for MyoD, (-30)GFP, (-30)GFP-MyoD were inserted also into the eukaryotic vector pcDNA 3 (carrying the resistance to kanamycin instead of ampicillin) using *NheI* and *HindIII* sites, *NdeI* (GATATG) and *NheI* sites, *NdeI* and *HindIII* sites, respectively (see Suppl. Fig. 2.1.2).

Protein purification. Recombinant variants were expressed in the BL21(DE3)pLysS *E. coli* strain. Starter cultures were prepared by growing multiple colonies of *E. coli* cells carrying the recombinant plasmids in a 1L flask containing LB added with ampicillin and chloramphenicol (respectively 100 µg/mL and 33 µg/mL); *E. coli* cells were grown with shaking until reaching an OD600nm ~ 0.6, at which time 0.4 mM IPTG was added to induce protein expression. Cells expressing recombinant proteins were collected after 12 hours of growing with shaking at ~17-23 °C. Protein purification required a first step of centrifugation at 6500 rpm, 4 °C for 20 minutes. The pellet was resuspended in the lysis buffer (PBS-NaCl 2M). Cells were disrupted by sonication on ice, using a Branson Sonifier 450 (Branson Ultrasonics, Danbury,CT, USA). The lysate was cleared by centrifugation at 12500 rpm, 4 °C for 30 minutes. The recombinant

proteins were recovered from supernatant by chromatography using a HIS-Select® Nickel Affinity Gel (Sigma-Aldrich). After separation on the chromatographic column, the proteins were eluted (NaCl 2M, Imidazol 0.75M, pH 8) and dialyzed (NaCl 0.5M, PBS). Eluition products were analyzed at spectrophotofluorometer to evaluate the quality and quantity of the purified proteins.

Sodium dodecyl sulfate polyacrylamide gel electrophoresis (SDS-PAGE). Purified protein products were mixed with loading buffer (20% glycerol, 25 mM Tris-HCl, 2% SDS, 0.1% bromophenol blue) and 10% dithiothreitol, and heated for 5 minutes at 95 °C. The samples were then loaded into a 8% polyacrylamide gel and analyzed using SDS-PAGE. After gel electrophoresis, proteins were transferred onto nitrocellulose filters and stained with Ponceau S (Sigma Aldrich).

Fabrication and preparation of nichoid culture substrate The nichoids were fabricated by two-photon polymerization technique in the SZ2080 photoresist with 1% of Irg (Irgacure 369, 2-Benzyl-2-dimethylamino-1-(4-morpholinophenyl)-butanone-1) photoinitiator [7]. Each nichoid block was characterized by 5x5 repetitive units, each 30 μm high and 90 μm × 90 μm in transverse dimensions (Supp. Fig. 2.1.3). Four 2PP-engineered niches were written on a 8-well chambered Lab-Tek™ II (Thermo Scientific-Nunc™) (Supp. Fig. 2.1.3D). In order to prepare the scaffold for cell-seeding the nichoid was incubated first into deionized water for 20 minutes, and then into 70% ethanol for 90 minutes. The scaffold was than washed repeatedly in sterile deionized water, dried and UV sterilized.

Cell culture. Rat bone marrow mesenchymal stem cells (rBM-MSCs) were kindly provided by Professor Andrea Remuzzi (Dept. of

Bionengineering, Institute of Pharmacological Research Mario Negri, Bergamo, Italy). Cells were cultured using α-MEM supplemented with 20% fetal bovine serum (v/v) (Gibco), penicillin 100 IU/mL/ streptomycin 100 µg/mL (Invitrogen) and 0.5 mM L-glutamine (Invitrogen).

2D Cell Culture. Cells were seeded in a 6-well plate at a density of $35 \cdot 10^3$ cells/well for genetic assays. For fluorescence imaging analyses cells were seeded or in a 24-well plate at a density of $8.5 \cdot 10^3$ cells/well or into 8-well Nunc® Lab-Tek® at a density of $5 \cdot 10^3$ cells/well.

3D Cell Culture. Cells were plated into a 8-well Nunc® Lab-Tek® with four nichoids per well. Each nichoid substrate is 450µm x 450µm x 30µm. Cells were seeded at a density of $5 \cdot 10^3$ cells/well.

Protein Transduction. 24 hours before transduction, cells were plated into a 6-well plate to reach 50% confluency.

Tat-GFP-MyoD was pre-mixed in Optimem medium (Gibco) at concentration of 25 µg/ml. Cell medium was replaced with premixed protein preparation. After 3 hours, transduction medium was replaced with cell growth medium.

For transduction of (-30)GFP-MyoD the molecule internalization is mediated by cationic molecules. tested several transfection reagents, liposomes-based and non-liposomal reagents: Lipofectamine™ MessengerMAX™, Lipofectamine™ 3000™, JetPRIME™, Fugene HD® (see Suppl. Table 2.1.1). I set specific conditions starting from the manufacturer's instructions (see Suppl. Table 2.1.2). The common steps are the following:

- ✓ 1 hour serum-free conditioning with Optimem medium (Gibco)
- ✓ addition of anionic protein:cationic molecule complex
- ✓ after 3 hours from protein transduction, replacement of transduction medium with cell growth medium.

Protein transduction efficiency was measured after 4 hours from protein addition and was calculated as:

$$Protein\ transduction\ efficiency\ (\%) = \frac{transduced\ nuclei}{total\ amount\ of\ nuclei} \qquad (2.1)$$

Nuclei were considered transduced when at least a green fluorescent spot was detected.

DNA transfection. DNA vectors were transfected using FuGENE® HD transfection reagent (Promega Corporation) according to manufacturer's instructions. Cells were plated 24 hours before transfection into a 6-well plate at a density of $35 \cdot 10^3$/well. I selected 3:1=FuGENE:DNA as the optimal transfection ratio. After 3 hours from DNA transfection, the transfection medium was replaced with supplemented growth medium.

Nuclear staining. In order to evaluate the transduction or transfection efficiency, I stained nuclei with Hoechst 33342 (Thermo Fisher) that is a blue fluorescent stain specific for DNA. In preparation of the nuclear staining, cells were first seeded on glass coverslip. After 4h from protein transduction or 48h from DNA transfection, cells were incubated in growth medium supplemented with Hoechst (1μg/ml). After 10 minutes, cells were fixed with paraformaldheyde (PAF) 4% for 15 minutes.

Fluorescence microscopy and image analysis. Cell fluorescence was detected using a FluoView FV10i confocal laser scanning microscope (Olympus America). Live cell imaging was performed at 37 °C, 5% CO_2. The following collection ranges were adopted: 352-455

nm (Hoechst), 489–510 nm (GFP), 390–510 nm (superfolderGFP). Images were analyzed with ImageJ software.

FRAP kinetics analysis. FRAP measurements were performed with a confocal Laser Scanning microscopy Olympus FV3000 equipped with 8 laser diodes, a 60X UPLSAPO silicone oil-immersion objective (NA 1.4) and an incubator chamber. The region of interest (ROI) in a FRAP measurement is the section that is photobleached and monitored in the fluorescence recovery. The ROI has been recorded selecting the nuclear area previously stained with DRAQ5 dye. Photobleaching of nuclear (-30)GFP-MyoD was achieved scanning near the center of the nucleus with the 488 nm laser at full (100%) power. The time required to photobleach most of the nuclear fluorescence, minimizing the bleaching of cytosolic fluorescence, is 3–5 s in spread nuclei and 100 ms in cells grown into the nichoid. Fluorescence recovery was measured starting a time-lapse acquisition within few hundred milliseconds (200 ms) after the bleaching, acquiring 15 images every 118 ms and then 70 images every 5 s. Ten acquisitions were performed for both cells grown on flat surface (spread nuclei) and cells grown into the 3D scaffold (roundish nuclei). The recovery of the fluorescence was evaluated for about 6 minutes, time sufficient to reach a stable fluorescence intensity plateau. This plateau corresponds to an equilibrium in which the exchange of dark and bright proteins from the cytosol and the nucleus is indistinguishable. The curves of the image background was subtracted from each acquisition. Data were normalized with the total cell GFP-fluorescence intensity, by using a ROI drowned on the cell edge. Data were also normalized on the average value of the nuclear fluorescence intensity calculated on the last 30 seconds of the measure. Then the obtained curves are shifted to start at the origin of the graph.

The fluorescence signal was assumed proportional to the (-30)GFP-Myod concentration and described from the function 2.2:

$$F_{(t)} = F^{\infty}_{(t)} + (F^{0}_{(t)} - F^{\infty}_{(t)})^{\left(-\frac{t}{\tau}\right)} \quad (2.2)$$

This averaged and normalized fluorescence recovery into the cell nucleus of spread and roundish nuclei was calculated and it was fitted (Origin Pro software) to a single exponential function using the following equation 2.3:

$$I = I_0 + Ae^{-\frac{t}{\tau}} \quad (2.3)$$

where τ is the characteristic time (time constant) of the protein translocation from cytosol to the nucleus, A, that is the difference between the nuclear fluorescence after the bleaching and the nuclear fluorescence at the end of the recovery, correspond to the fraction of protein involved and I_0 is the fluorescence measured at the end of the recovery.

To better understand the transport process we also evaluated a parameter F defined as:

$$F \propto \frac{fluorescence\ intensity(\tau)\ \times nuclear\ area}{\tau} \quad (2.4)$$

It provides an indication of nuclear import rate based on the photobleached nuclear area, the characteristic time τ and the fluorescence intensity at τ time..

Gene expression analysis. In order to evaluate the gene expression levels of mRNA target genes of MyoD, MSC culture samples were lysed for RNA extraction after 9 hours from protein transduction or 72

hours from DNA transfection. RNA was extracted from the MSC culture samples using miRNeasy Mini Kit (Qiazol™) following manufacturer's instructions. The quantity and purity of extracted RNA was measured via spectrophotometry (ND-1000; NanoDrop™). cDNA was synthesized from total RNA using the High-Capacity cDNA Reverse Transcription Kit (Applied Biosystems™). Relative mRNA expression levels of myogenin (Myog), cadherin 15 (Cdh15), desmin (Des), Creatin Kinase M-Type (CKM) were measured via quantitative real-time polymerase chain reaction (qRT-PCR) using TaqMan™ Reagents (Applied Biosystems™) on an 7900HT Fast Real-Time PCR System (Applied Biosystems™). In quantitative real-time PCR reference genes are used to normalize the data and eliminate the errors related to differences in quantities of cDNA prepared in reaction. I use 18s rRNA as reference gene. To calculate the gene expression level, different methods can be used. I selected the widely used Livak method which calculate the normalized expression ratio respect to a calibrator. The calibrator is a negative control inserted in the experimental set-up. At the end of the real-time PCR reaction, the instrument returns Ct (Threshold Cycle) values in inverse proportion to initial cDNA amount. Considering *test* and *calibrator* the samples and *Ref* and *target* the genes, the calculation steps are the following:

$$\Delta C_{T(test)} = C_{T(Target,test)} - C_{T(Ref,test)} \quad (2.4)$$

$$\Delta C_{T(Cal)} = C_{T(Target,Calibrator)} - C_{T(Ref,Calibrator)} \quad (2.5)$$

$$\Delta\Delta C_T = \Delta C_{T(Test)} - \Delta C_{T(Cal)} \quad (2.6)$$

$$2^{-\Delta\Delta C_T} = normalized\ expression\ ratio \quad (2.7)$$

Statistical analyses. The experimental data were analyzed by one-way analysis of variance (ANOVA), two-way ANOVA and post hoc tests, or with Student's t-test for a direct comparison of two groups. Associations with P values < 0.05 were considered significant. ns P >0.05; * P <0.05; ** P <0.01; *** P <0.001; **** P <0.0001. Statistical tests were done using GraphPad Prism 7.0 software.

References

1. Lawrence MS, Phillips KJ, Liu DR. Supercharging proteins can impart unusual resilience. J Am Chem Soc. 2007 Aug 22;129(33):10110-2.

2. Nagahara H, Vocero-Akbani AM, Snyder EL, Ho A, Latham DG, Lissy NA, Becker-Hapak M, Ezhevsky SA, Dowdy SF. Transduction of full-length TAT fusion proteins into mammalian cells: TAT-p27Kip1 induces cell migration. Nat Med. 1998 Dec;4(12):1449-52.

3. Ogawa T, Ono S, Ichikawa T, Arimitsu S, Onoda K, Tokunaga K, Sugiu K, Tomizawa K, Matsui H, Date I. Novel protein transduction method by using 11R: an effective new drug delivery system for the treatment of cerebrovascular diseases. Stroke. 2007 Apr;38(4):1354-61.

4. Derossi D, Joliot AH, Chassaing G, Prochiantz A. The third helix of the Antennapedia homeodomain translocates through biological membranes. J Biol Chem. 1994 Apr 8;269(14):10444-50.

5. Zuris JA, Thompson DB, Shu Y, Guilinger JP, Bessen JL, Hu JH, Maeder ML, Joung JK, Chen ZY, Liu DR. Cationic lipid-mediated delivery of proteins enables efficient protein-based genome editing in vitro and in vivo. Nat Biotechnol. 2015 Jan;33(1):73-80.

6. Bergstrom DA, Penn BH, Strand A, Perry RL, Rudnicki MA, Tapscott SJ. Promoter-specific regulation of MyoD binding and signal transduction cooperate to pattern gene expression. Mol Cell. 2002 Mar;9(3):587-600.

7. Ricci D, Nava MM, Zandrini T, Cerullo G, Raimondi MT, Osellame R. Scaling-Up Techniques for the Nanofabrication of Cell Culture Substrates via Two-Photon Polymerization for Industrial-Scale Expansion of Stem Cells. Materials (Basel). 2017 Jan 13;10(1).
8. Frankel AD, Pabo CO. Cellular uptake of the tat protein from human immunodeficiency virus. Cell. 1988 Dec 23;55(6):1189-93.
9. Green M, Loewenstein PM. Autonomous functional domains of chemically synthesized human immunodeficiency virus tat trans-activator protein. Cell. 1988 Dec 23;55(6):1179-88.
10. Domashenko AD, Danet-Desnoyers G, Aron A, Carroll MP, Emerson SG. TAT-mediated transduction of NF-Ya peptide induces the ex vivo proliferation and engraftment potential of human hematopoietic progenitor cells. Blood. 2010 Oct 14;116(15):2676-83.
11. Wang Y, Fu L, Liu B, Wang X, Wang K, Ye M. Construction of human LRIG1-TAT fusions and TAT-mediated LRIG1 protein delivery. Biomed Pharmacother. 2015 Feb;69:396-401.
12. Sunavala-Dossabhoy G, Palaniyandi S, Richardson C, De Benedetti A, Schrott L, Caldito G. TAT-mediated delivery of Tousled protein to salivary glands protects against radiation-induced hypofunction. Int J Radiat Oncol Biol Phys. 2012 Sep 1;84(1):257-65.
13. Rapoport M, Lorberboum-Galski H. TAT-based drug delivery system—new directions in protein delivery for new hopes? Expert Opin Drug Deliv. 2009 May;6(5):453-63.
14. Cardarelli F, Serresi M, Bizzarri R, Beltram F. Tuning the transport properties of HIV-1 Tat arginine-rich motif in living cells. Traffic. 2008 Apr;9(4):528-39. doi: 10.1111/j.1600-0854.2007.00696.x. Epub 2007 Dec 21. Erratum in: Traffic. 2008 Dec;9(12):250.
15. Cardarelli F, Serresi M, Bizzarri R, Giacca M, Beltram F. In vivo study of HIV-1 Tat arginine-rich motif unveils its transport properties. Mol Ther. 2007 Jul;15(7):1313-22.

16. Molle D, Maiuri P, Boireau S, Bertrand E, Knezevich A, Marcello A, Basyuk E. A real-time view of the TAR:Tat:P-TEFb complex at HIV-1 transcription sites. Retrovirology. 2007 May 30;4:36.
17. Becker-Hapak M, McAllister SS, Dowdy SF. TAT-mediated protein transduction into mammalian cells. Methods. 2001 Jul;24(3):247-56.

Supplementary Figures

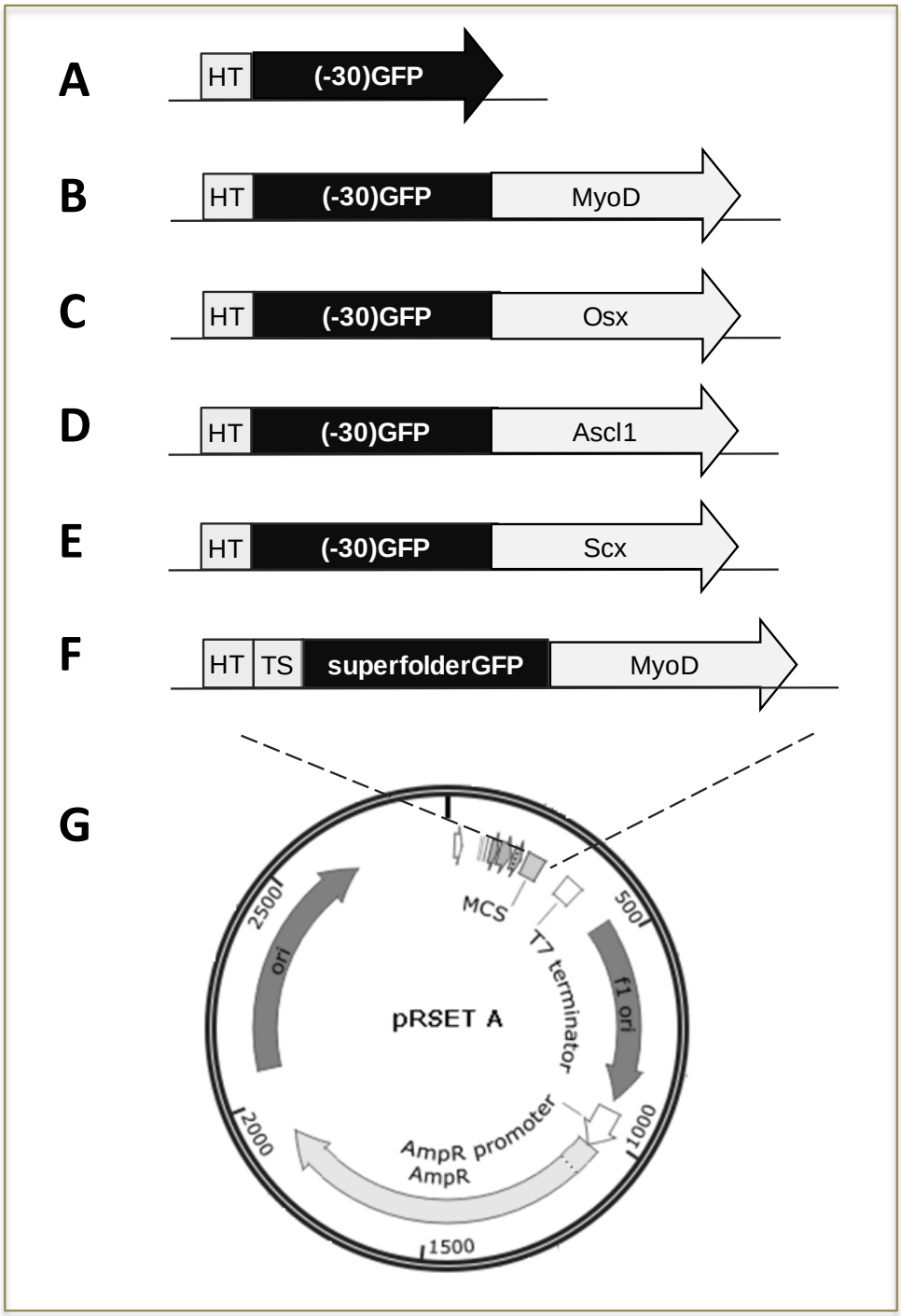

Suppl. Fig. 2.1.1 Schematic reproduction of the procariotic DNA vectors codifying for the purified fluorescent transcription factors. Each sequence inserted in the procariotic vector pRSET A (G) contains an upstream HT sequence codifying for the Histidin-Tag; (A) sequence

codifying for (-30)GFP; (B) sequence codifying for (-30)GFP-MyoD; (C) sequence codifying for (-30)GFP-Osx; (D) sequence codifying for (-30)GFP-Ascl1; (E) sequence codifying for (-30)GFP-Scx; (F) sequence codifying for Tat-superfolderGFP-MyoD. (TS: Tat Sequence**).**

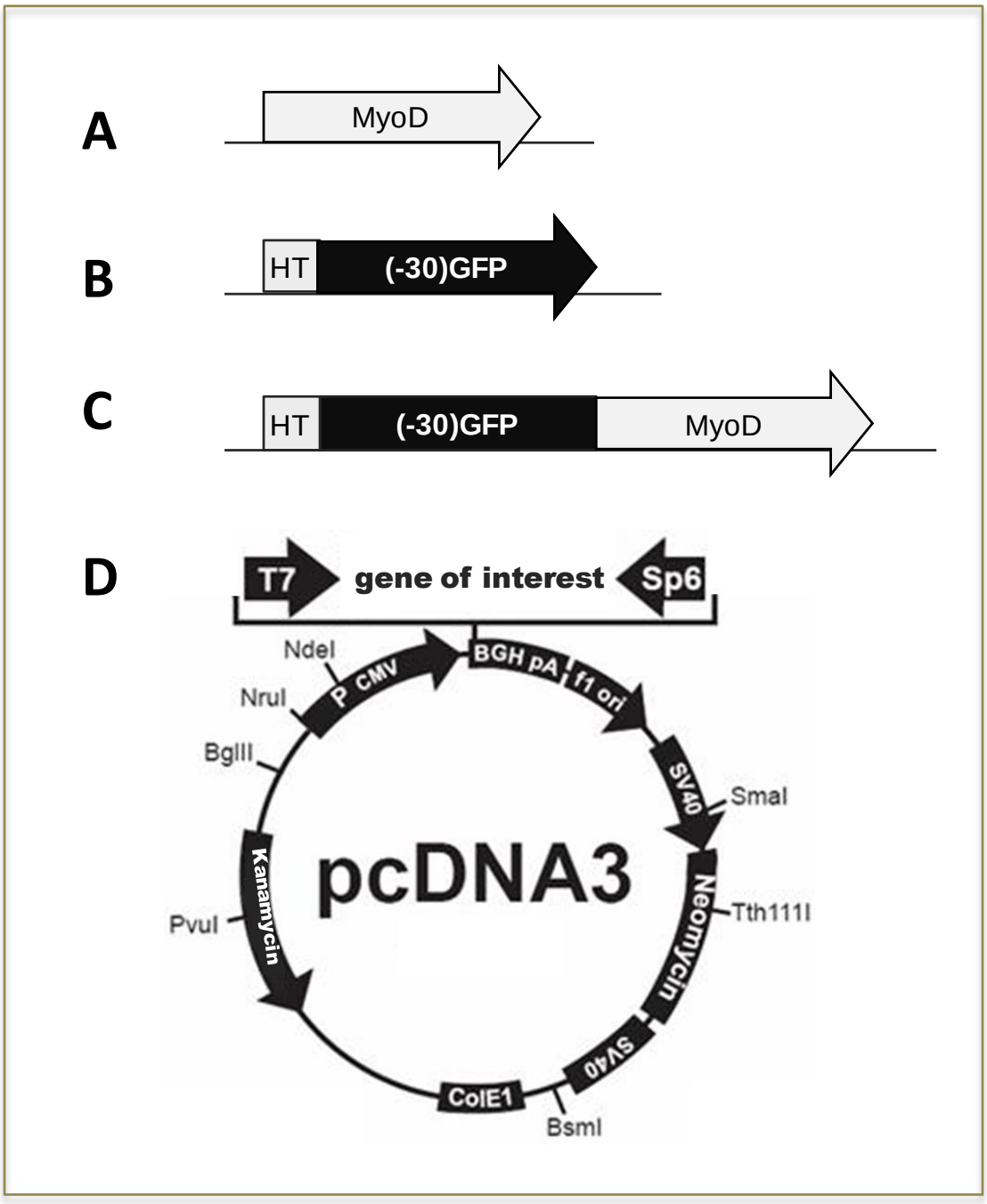

Suppl. Fig. 2.1.2 Schematic reproduction of the eukaryotic DNA vectors codifying for Myod (A), (-30)GFP (B) or (-30)GFP-MyoD (C). The vector used as backbone for the construction of the recombinant plasmid is the pcDNA3 (D). (HT=Histidin-Tag).

Transfection reagent	Manufacturer	Liposomal-based	Standard molecule delivered
Lipofectamine™ 3000	Thermo Fisher	YES	RNA/DNA
Lipofectamine™ MessengerMAX	Thermo FIsher	YES	mRNA
JetPRIME™	Polyplus transfection	NO	DNA/siRNA
Fugene® HD	Promega Corporation	NO	DNA

Suppl. Table 2.1.1 Transfection reagents properties.

24-well plate			
Transfection reagent	PROTEIN (µg/500µl)	Transfection reagent (µl)	Buffer(µl)
Lipofectamine™ 3000	8	2	/
Lipofectamine™ MessengerMAX	8	2	/
JetPRIME™	8	2.25	50
Fugene® HD	2	4	/

6-well plate			
Transfection reagent	PROTEIN (µg/ml)	Transfection reagent (µl)	Buffer (µl)
Lipofectamine™ MessengerMAX	15	10	/

Suppl. Table 2.1.2 Protein transduction procedures. The volume of plating medium is 500 µl in the case of the 24-well plate and 2 mL in the case of 6-well plate. The ratio between reagents changed depending on the type of the transfection reagents.

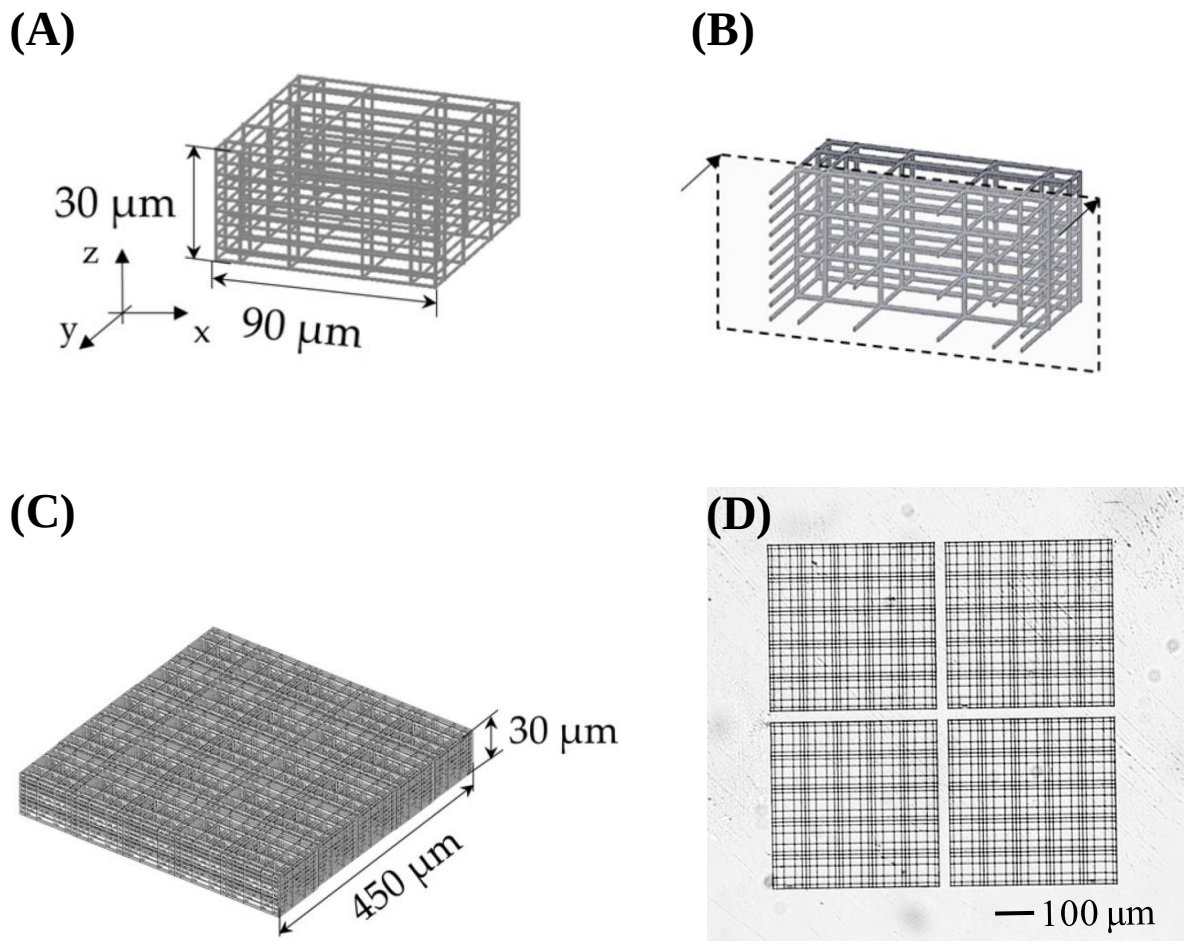

Suppl. Fig. 2.1.3 Nichoid culture substrate. (A) CAD of the nichoid unit; (B) CAD of the cross-section of the nichoid; (C) CAD of the 5 × 5 nichoid units. (D) Brightfield image acquisition (5X magnification) of four 2PP-engineered niches written on a chambered 160 µm thick cover glass (Lab-Tek™ II, Thermo Scientific-Nunc™). Adapted from ref. [7].

CHAPTER 2.2: Photosensitive MyoD variants

Summary

The most widely used approaches for nucleocytoplasmic transport are based on perturbation of optical properties of fluorescent probes. Photoactivation, photoconversion and photoswitching are three methods of monitoring the intracellular shuttling of specific molecules.
With the purpose of studying the nuclear import of the myogenic transcription factor (TF), MyoD, I developed three recombinant variants of MyoD, two photoactivatable and one photoconvertible. I fused the TF to PAGFP, PAmCherry and mEos3.2. Every photosensitive variant was transfected in mesenchymal stem cells (MSCs) and their expression was evaluated by fluorescence confocal microscopy. Acquired images showed that every recombinant variant of MyoD emitted a brilliant fluorescence and localized predominantly in the nuclear area. The protein intracellular distribution confirmed that native TF location was maintained and labels didn't interfere with MyoD physiology. Real-time PCR analyses on the transcription promoting activity of the photosensitive variant of MyoD showed that the label that interfered the least with MyoD functionality was PAGFP.
In conclusion, MyoD-PAGFP is a suitable photoactivatable tool for nucleocytoplasmic shuttling of MyoD offering different opportunities of detection. It also provides the possibility to investigate the biological effects dependent on its transcription promoting activity.

Introduction

A category of fluorescent probes (FP) used for nucleocytoplasmic shuttling is represented by photoactivatable, photoconvertible and photoswitchable FP. These probes can be activated from a non-fluorescent state, converted in their emission spectrum or switched in a reversible way (Fig. 2.2.1).

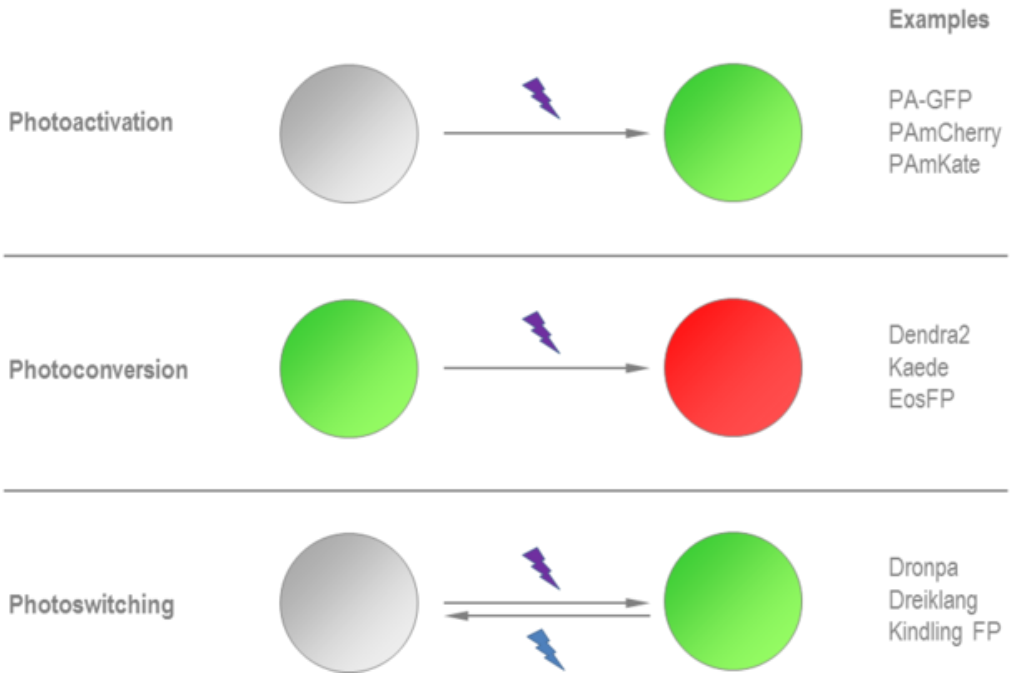

Fig. 2.2.1 Examples of photoactivation, photoconversion and photoswitching. Image adapted from www.leica-microsystems.com/science-lab/photoactivatable-photoconvertible-and-photoswitchable-fluorescent-proteins.

Photoactivation is an irreversible process by which, after the irradiation with a ultra violet A (UVA) laser (~405nm wavelength), proteins are switched from a low fluorescent state to a high fluorescent emission state. The excitation (Ex) and the emission (Em) wavelength do not change. Examples of photoactivatable FP are PAGFP, that switches its fluorescence emission in a bright green light, and PAmCherry, that emits bright red wavelengths [1,2].

Photoconversion is easier to detect respect to photoactivatable FP because they emit fluorescence even in their non-converted state. Photoconversion switches both Ex and Em. An example is provided by the monomeric mEoS FP which switches its fluorescence from green to red converting its Ex_{max} from 505 to 569 nm and Em_{max} from 516 to 581 nm [3].

Photoswitching is a reversible conversion of a non-fluorescent state into a fluorescent state and viceversa. Irradiation at 405 nm causes photoactivation and on the contrary, excitation at 488 nm causes return to non-fluorescent state. Dronpa is an example of photoswitchable FPs [4].

The use of photosensitive FP in nucleocytoplasmic transport allows to the perturbation of the fluorescent state of selected FP and follows the movement inside the cell. Photoactivation/conversion/switching constitute different perturbation-based approaches as FRAP method. Photoswitchable/convertible FP can be exploited to combine their optical properties and unfold complex mechanisms. A pioneering work is represented by the study of Ando and colleagues that investigated Erk (extracellular signal-regulated kinase) protein regulation. They used a Dronpa-based variant of Erk protein to activate or erase the fluorescence of the molecule [5].

Photoactivatable FPs have been used to investigate several processes such as binding/dissociation dynamics or nucleocytoplasmic kinetics [6-8]. An example is provided by the study of Schmierer and colleagues published in 2005 [8]. They investigated the kinetics of Smad nucleocytoplasmic shuttling and they used photoactivation approach in combination with FRAP technique in order to quantify Smad2 shuttling.

In this work I designed, developed and assessed three recombinant variants of the myogenic transcription factor fused to photosensitive FP. I selected two photoactivatable FP, PAGFP and PAmCherry, and the photoconvertible mEOS3.2. With the aim to validate them for nucleocytoplasmic transport detection, I transfected the constructs into mesenchymal stem cells and verified the protein localization by fluorescence confocal microscopy. In order to assay the effect of the photosensitive FP on the MyoD functionality, I evaluated gene expression levels of target genes of MyoD by real-time PCR. PAGFP resulted the FP that best maintained the native features of MyoD adding photosensitive optical properties for nucleocytoplasmic shuttling detection.

Results

Engineering and expression of constructs

I subcloned MyoD sequence into three plasmids coding for the monomeric photoactivatable PAGFP, PAmCherry or the monomeric photoconvertible mEos3.2. I used TOP10 *E.coli* cells for gene cloning and plasmid amplification. From the gene fusion I obtained pMyoD-PAGFP, pMyoD-PAmCherry, pMyoD-mEos3.2 (Fig. 2.2.2).
In order to compare the activity of photosensitive variant of MyoD with the native functionality, I subcloned MyoD into an empty pcDNA3 and I also amplified pPAGFP, pPAmCherry, pmEos3.2 and pEGFP as specific negative controls for each MyoD variant.

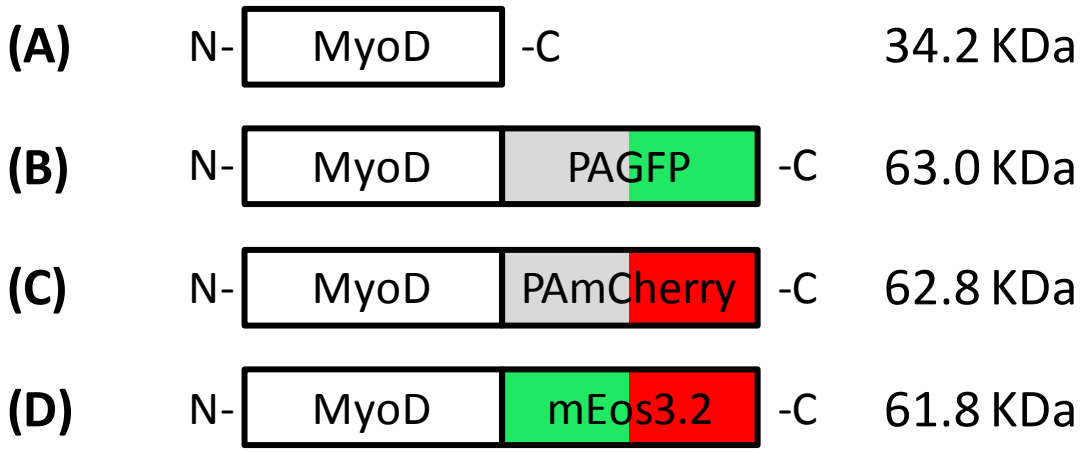

Fig. 2.2.2 Schematic representation of photosensitive variants of MyoD. (A) Native MyoD (MW=34.2 kDa); (B) MyoD-PAGFP (MW=63.0 kDa) can be activated from a non-fluorescent state to a green fluorescent state; (C) MyoD-PAmCherry (MW=62.8 kDa) can be activated from a non-fluorescent state to a red fluorescent state; (D) MyoD-mEos3.2 (MW=61.8 kDa) can be converted from a green fluorescent state to a red fluorescent state.

I transfected the recombinant constructs in rat bone marrow MSCs by standard DNA transfection procedures.

Protein expression and localization

In order to evaluate MyoD variants localization we first tested the photosensitivity of the construct by fluorescence confocal microscopy.
We started from photoactivatable variants (PAFP), thus MyoD-PAGFP and MyoD-PAmCherry.
MSCs overexpressing PAFP did not emit fluorescence until photoactivation. In order to switch their fluorescence state, we irradiated with a single cell with light in the violet spectrum.
MyoD-PAGFP is a PAFP that, after photoactivation with UVA light, shows a strong increase in green light fluorescence emission (maximum Ex ~504 nm and maximum Em ~515nm) (Suppl. Table 2.2.1). We used the spectra detection filters of standard EGFP (Ex 489/Em 510) to acquire the protein fluorescence. As shown in Fig.

2.2.3C, MyoD-PAGFP resulted well expressed in the whole cell with a predominantly localization in the nucleus that corresponds to the physiological location of MyoD.

MyoD-PAmCherry is a PAFP that, after photoactivation, shows a strong increase in bright red light emission (Suppl. Table 2.2.1). To detect its fluorescence we used optical filters to of standard mCherry detection (Ex 580/Em 610). Fig. 2.2.3D shows MSCs overexpressing a brilliant MyoD-PAmCherry distributed predominantly in the nuclear region, confirming that, as in the case of MyoD-PAGFP, MyoD guided the localization of the recombinant proteins and that the PAGFP and PAmCherry did not alter the physiological localization of the myogenic transcription factor.

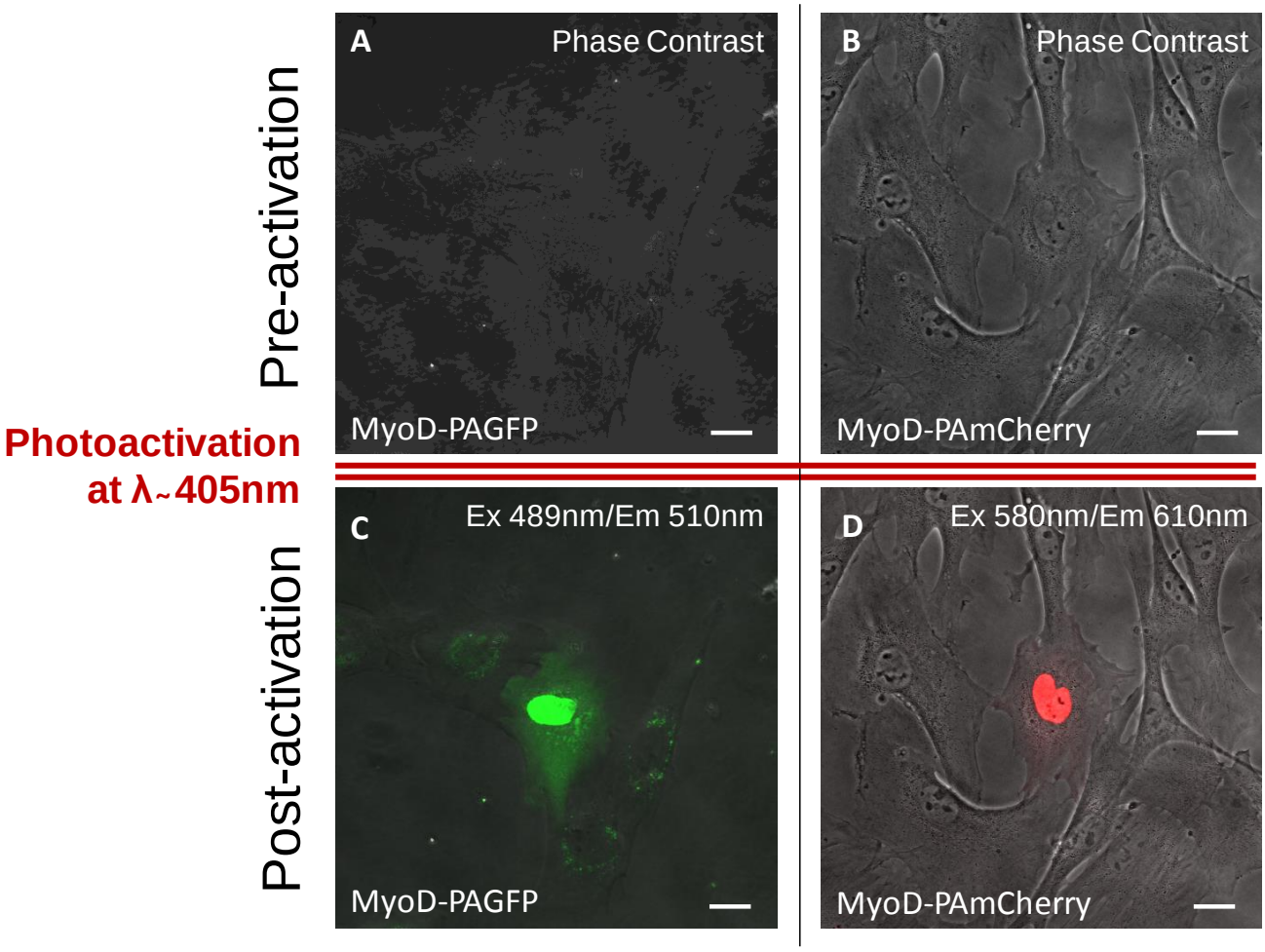

Fig. 2.2.3 Photoactivation of MSCs transfected with pMyoD-PAGFP (A-C) or pMyoD-PAmCherry (B-D). A and B represent the pre-activation state of MSCs expressing the recombinant proteins. C and D represent MSCs expressing the form of the construct photoactivated. Images were acquired by fluorescence confocal microscopy. Scale bar: 20 μm.

In order to test protein expression and localization of MyoD-mEos3.2 the procedure was similar to the PAFP. MyoD-mEos3.2 could be converted from a fluorescent state (green) to another fluorescent state (red). We irradiated MSCs overexpressing MyoD-mEos3.2 with a 405 nm laser light triggering the conversion of green fluorescence into red fluorescence. To detect the photoconversion, we acquired images in the green and red channel simultaneously (spectra parameters of both mCherry (Ex 580/Em 610) and EGFP (Ex 489/Em 510) dyes). As shown in Fig. 2.2.4, MyoD-mEOS3.2 was well expressed into MSCs. The photoconversion showed an increase in red fluorescence (Fig. 2.2.4B,D) and a decrease in green fluorescence (Fig. 2.2.4A,C). Photoconvertible MyoD localized in the whole cell with a major abundance in the nucleus.

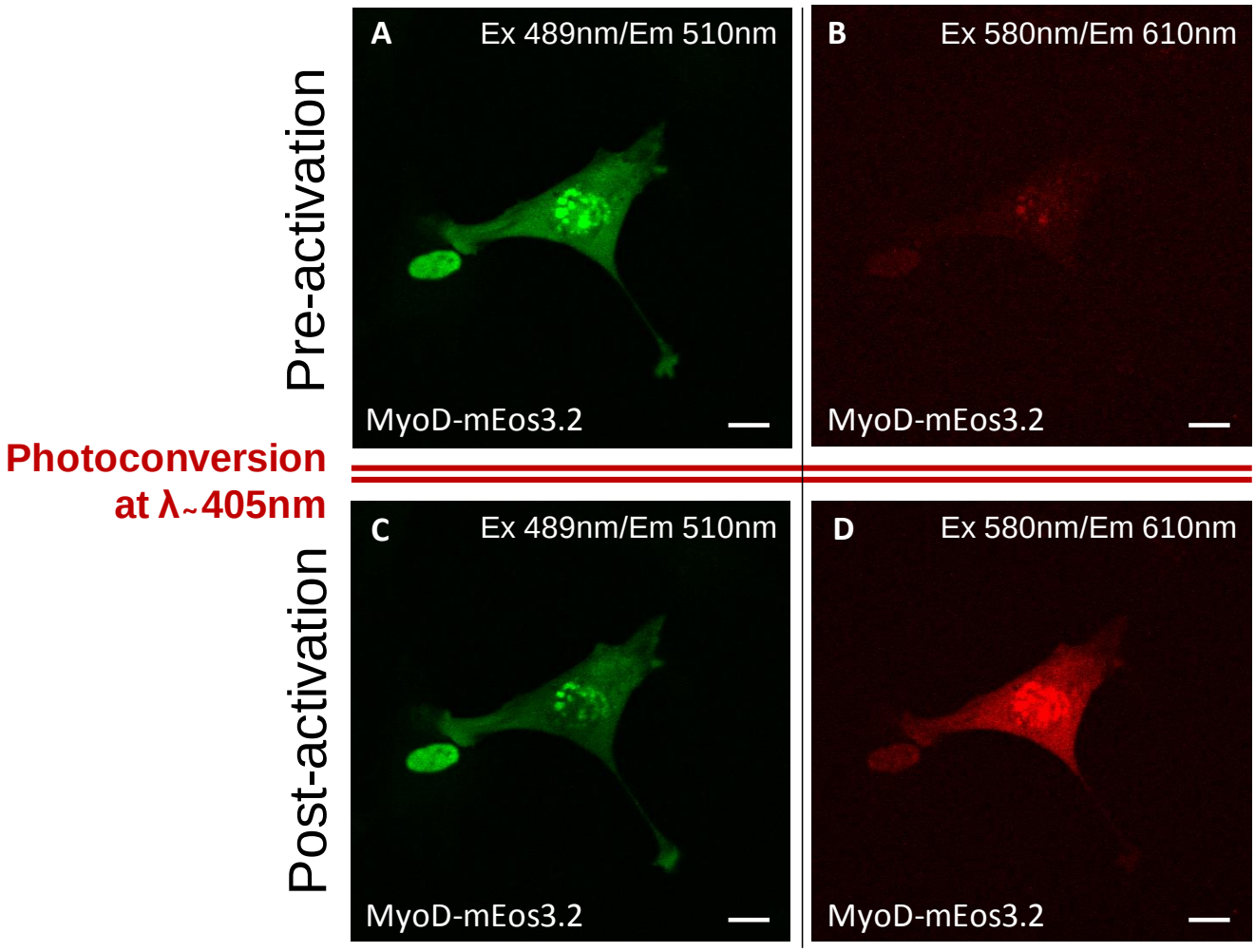

Fig. 2.2.4 Photoconversion of MSCs transfected with pMyoD-mEos3.2. A, B, C and D represent the same cell subjected to different collection ranges: A and C to Ex 489nm/ Em 510nm; B and D to Ex 489nm/ Em 510nm. A and B show the pre-activation state of MSCs expressing the recombinant protein. C and D represent MSCs expressing the form of the construct photoconverted. Images were acquired by fluorescence confocal microscopy. Scale bar: 20 μm.

Transcription promoting activity assay

Once I validated the protein expression and the maintenance of MyoD properties in terms of intracellular localization, I assessed the influence of the photosensitive labels on the transcription factor transcription promoting activity. To do so, I evaluated the gene expression levels of target genes of MyoD by real-time PCR.

I transfected MSCs with pMyoD, pMyoD-PAGFP, pMyoD-PAmCherry and pMyoD-mEos3.2. MSCs transfected with pEGFP, pPAGFP, pPAmCherry and pmEos3.2 were used as calibrators for MyoD variants, respectively. I extracted total mRNA at 72 hours after DNA transfection. cDNA was synthesized from mRNA and processed for relative quantification by real-time PCR. I analyzed the expression levels of Myogenin (Myog) and Creatin Kinase M-type (CKM), as previously selected (Fig. 2.1.8).

As shown in Fig. 2.2.5 the only photosensitive variant of MyoD that showed a significant increase of Myog expression with respect to its negative control is MyoD-PAGFP. In fact, MSCs transfected with pMyoD-PAGFP showed a about 60-fold increase of the transcription of the target gene respect to MSCs transfected with PAGFP without MyoD. The other two recombinant variants of MyoD showed a weak positive transcription promoting activity but with low reproducibility and, consequently, high standard deviation. Overall, Myog expression promotion by MyoD-PAmCherry and MyoD-mEos3.2 was negligible, when compared to mRNA Myog expression levels promoted by native MyoD and MyoD-PAGFP.

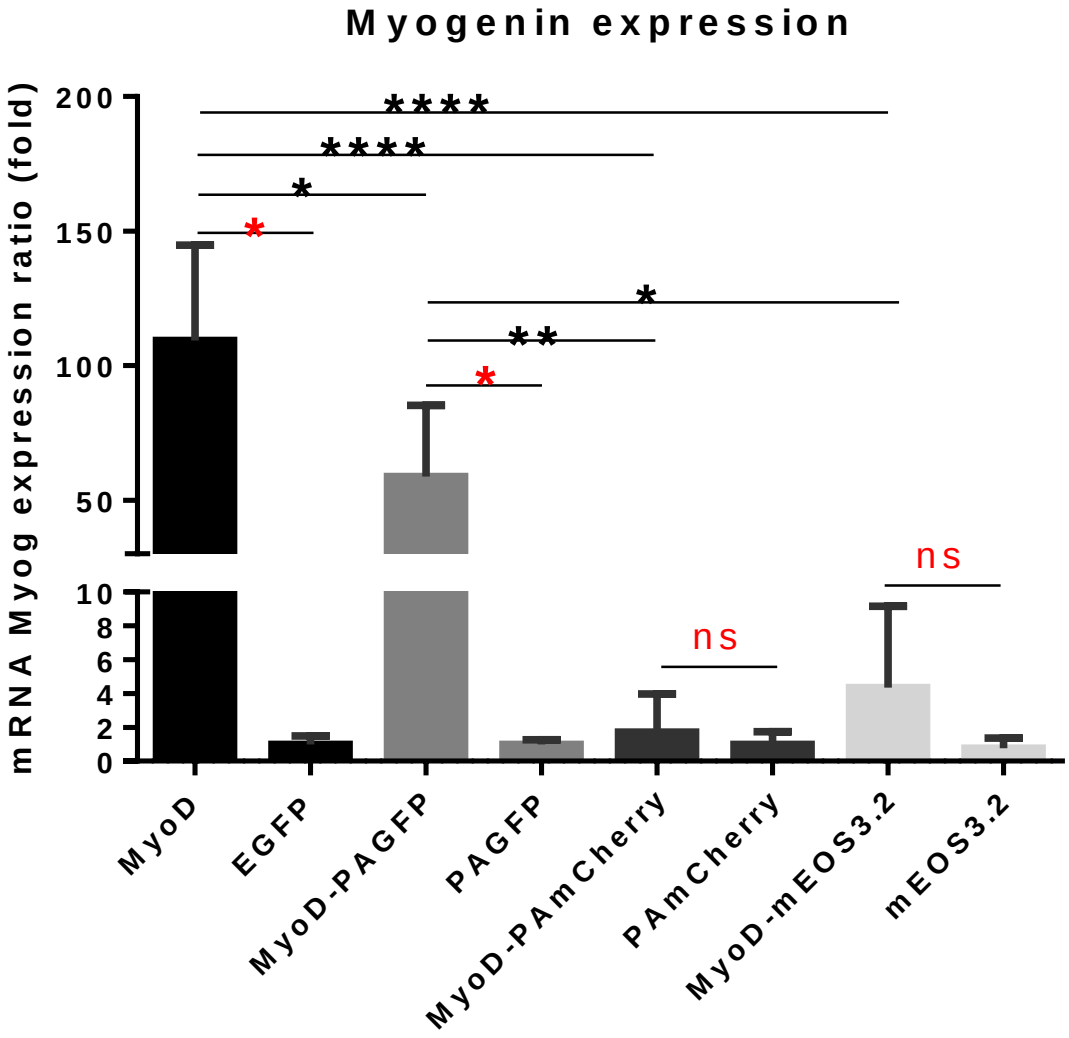

Fig. 2.2.5 Myogenin (Myog) transcription promotion by photosensitive variants of MyoD. MSCs were transfected with DNA plasmids: pMyoD, pMyoD-PAGFP, pMyoD-PAmCherry and pMyoD-mEos3.2. MSCs transfected with pEGFP, pPAGFP, pPAmCherry and pmEos3.2 were used as technical calibrators for MyoD variants, respectively. Data were assessed by one way-ANOVA test followed by Tukey's multiple comparisons test and by Student's t-test for comparison between two groups. Data are expressed as mean ± SD. Significance symbols highlighted in red refer to Student's t-test. Significance symbols in black refer to one way-ANOVA test.

Analyzing mRNA CKM expression in Fig. 2.2.6, we can see that the transcription promotion pattern is the same of Myog expression but with a weaker effect. In fact, MSCs transfected with pMyoD-PAGFP

showed a significant 2-fold increase in the mRNA CKM expression level respect to MSCs transfected with pPAGFP.

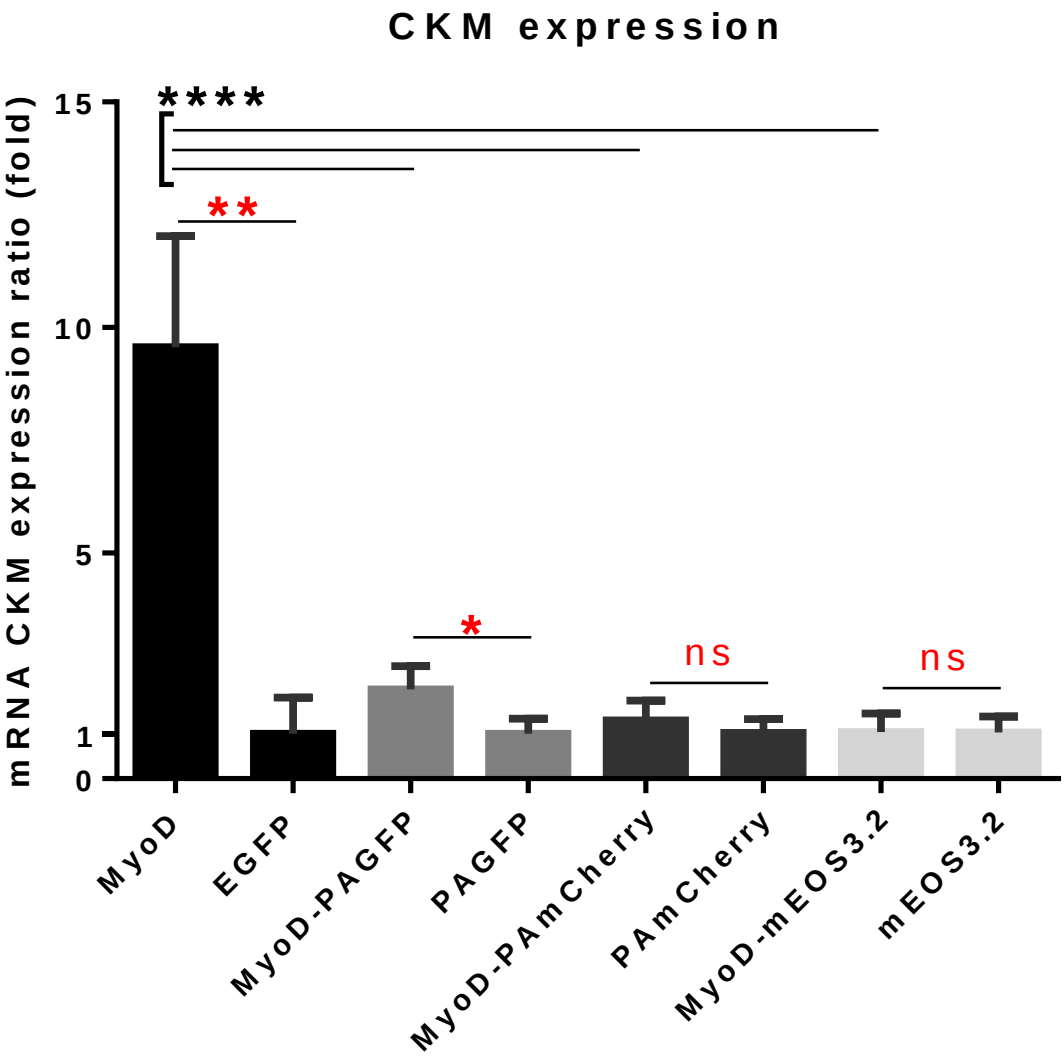

Fig. 2.2.6 Creatin Kinase M-type (CKM) transcription promotion by photosensitive variants of MyoD. MSCs were transfected with DNA plasmids: pMyoD, pMyoD-PAGFP, pMyoD-PAmCherry and pMyoD-mEos3.2. MSCs transfected with pEGFP, pPAGFP, pPAmCherry and pmEos3.2 were used as technical calibrators for MyoD variants, respectively. Data were assessed by one way-ANOVA test followed by Tukey's multiple comparisons test and by Student's t-test for comparison between two groups. Data are expressed as mean ± SD. Significance symbols highlighted in red refer to Student's t-test. Significance symbols in black refer to one way-ANOVA test.

Since MyoD-PAmCherry and MyoD-mEos3.2 showed not significant transcription promotion activity in both mRNA Myog and CKM expression levels, MyoD-PAGFP resulted the best photosensitive variant of MyoD to resemble the native functionality.

Discussion

Recent advancements in optical microscopy and molecular engineering have contributed to generate perturbation-based methods to quantify nucleocytoplasmic shuttling, including photobleaching techniques (i.e FRAP), photoactivation (switch from a non-fluorescent state to a fluorescent state), photoconversion (switch to a different spectrum of fluorescence) or photoswitching (reversible process of photoactivation).

With the purpose to measure the nuclear import rate of the myogenic transcription factor (TF) MyoD, in this work I generated three variants of the TF, two photoactivatable and one photoconvertible. Differently than the previous fluorescent tools developed with the same purpose (see Chapter 2.1), these photosensitive variants lack protein transduction domains and follow classic DNA transfection procedures for intracellular delivery.

Photoactivation and photoconversion were performed by fluorescence confocal microscopy. Live-cell imaging showed a protein intracellular localization corresponding to the physiological location of MyoD. This common behavior suggested that MyoD was able to guide each recombinant protein to the nucleus without interference of the labels.

Real-time PCR assay to assess transcription promotion activity highlighted some limitation of the photosensitive variants of MyoD.

CKM and Myog expression levels suggested an inhibitory effect of PAmCherry and mEos3.2 on MyoD activity (Fig. 2.2.5-2.2.6). This effect could be partially justified also by an observed reduced transfection efficiency compared to standard pEGFP transfection procedures (data not shown). On the contrary, PAGFP-MyoD showed a significant increase of both target genes in comparison to MSCs transfected with pPAGFP without MyoD. Analyzing the structures of the three photosensitive labels, a secondary structure prediction study (using PSI-blast based secondary structure PREDiction (PSIPRED) server) does not highlight evident differences showing a similar beta barrel organization for all the photosensitive GFP. On the contrary, comparing the sequences of the PAmCherry or mEos3.2 with PAGFP, the sequence alignments show important differences in aminoacidic composition. In fact, PAmCherry is identical to PAGFP just for 30% of residues (47% positives) and mEos3.2 is identical to PAGFP for 28% of residues (52% positives). It could be interesting a deepening to understand if this difference in aminoacidic composition could influence the recombinant protein stability and functionality.

Comparing the PAGFP-MyoD transcription promotion activity to the native MyoD functionality, the assays showed a significantly low level of activity. This difference could be attributed to the different biochemical characteristic of the proteins: MyoD is 34.2 kDa while MyoD-PAGFP is 62.0 kDa. This two-fold molecular weight and steric hindrance could justify the difference in transcription promotion activity from different aspects. First, this two-fold dimension could slow the intracellular movement of the proteins and also their kinetic. Second, it could alter the stability of the protein and its interaction with the cofactors in triggering transcription. Third, the shorter amino acidic sequence of MyoD (316 aa) is translated faster by MSC translational machinery than MyoD-PAGFP amino acidic sequence (574 aa). The

combination of these aspects could be transduced into more protein product and kinetically faster in the case of MyoD respect to MyoD-PAGFP at the same time point. Further analyses could deepen the trend of MyoD-PAGFP activity in time. For instance, Western Blotting, a protein immunoblot technique, could be used to provide information about the recombinant protein expression.

In summary, MyoD-PAGFP is the photosensitive fluorescent variant of MyoD that best represent the properties of MyoD and that could be used for nucleocytoplsmic transport studies. As part of the photoactivatable FP, this fluorescent tool offers different possibilities of monitoring its nucleocytoplasmic shuttling. An approach is based on the use of the fluorescence confocal microscopy and on the photoactivation process to selectively switch “on” molecules in a ROI and follow their intracellular movement. This approach was previously used to study the nuclear import of several proteins. Examples are provided by STAT3 transcription factor and Protein Kinase D3 (PDK3) [9-10]. In both cases, STAT3 and PDK3 were fused to PAGFP and once photoactivated, their nuclear import/export was evaluated.

Another approach widely used with photoactivatable FP is based on super-resolution microscopy that overcome the diffraction barrier [11]. Photoactivation localization microscopy (PALM) is a technique that exploits the optical properties of the photoactivatable FP to precisely localize them determining the center of the fluorescence emission. Recent advancements combined PALM with single particle tracking (sptPALM) to monitor single particle movement after photoactivation [12, 13]. SptPALM could represent an advanced perturbation-based technique useful to monitor nucleocytoplasmic shuttling of MyoD-PAGFP collecting single particle tracking information.

Methods

Gene cloning. MyoD sequence was amplified inserting in the primers specific enzyme sites: *BglII* (AGATCT) at 5' of the forward primer and *EcorI* (GAATTC) site at 5' of the reverse primer. The amplified sequence was subcloned into pPAGFP-N1 (Suppl. Fig. 2.2.1), pPAmCherry-N1 (Suppl. Fig. 2.2.2) and pmEOS3.2-N1 (Suppl. Fig. 2.2.3). I used TOP10 *E.coli* strain for gene cloning procedures.
pMyoD engineering details can be found in Chapter 2.1, "Methods", "Gene cloning" section.
pEGFP was kindly provided by Professor Alessandro Negro (Dept. Biomedical Sciences, University of Padua).

Cell culture. Rat bone marrow mesenchymal stem cells (rBM-MSCs) were kindly provided by Professor Andrea Remuzzi (Department of Bionengineering, Institute of Pharmacological Research Mario Negri, Bergamo, Italy). Cells were cultured using α-MEM supplemented with 20% fetal bovine serum (v/v) (Gibco), penicillin 100 IU/mL/ streptomycin 100 µg/mL (Invitrogen) and 0.5 mM L-glutamine (Invitrogen). Cells were seeded in a 6-well plate at a density of $35 \cdot 10^3$/well for genetic assays. For fluorescence imaging analyses, instead, cells were seeded in a 24-well plate at a density of $8.5 \cdot 10^3$/well or into 8-well Nunc® Lab-Tek® at a density of $5 \cdot 10^3$/well.

DNA transfection. DNA vectors were transfected using FuGENE® HD transfection reagent (Promega Corporation) according manufacturer's instructions. Cells were plated 24 hours before transfection into a 6-well plate at a density of $35 \cdot 10^3$/well. I selected 3:1=FuGENE:DNA as the optimal transfection ratio. After 3 hours from DNA transfection, the transfection medium was replaced with supplemented growth medium.

Fluorescence microscopy and image analysis. Cell fluorescence was detected using a FluoView FV10i confocal laser scanning microscope (Olympus America). Live cell imaging was performed at 37 °C, 5% CO_2. The following collection ranges were adopted: 489– 510 nm (EGFP), 580-610 nm (mCherry). Images were analyzed with imageJ software.

Photoactivation and photoconversion. Photoactivation and photoconversion were performed by fluorescence confocal microscopy (FluoView FV10i, Olympus America) (See Suppl. Table 2.2.1).
Since photoactivatable FP switch from a non-fluorescent state to a fluorescent state, the procedure to reach photactivated MSCs required a time-consuming step involving cell-by-cell irradiation.
Photoactivation of MyoD-PAGFP and MyoD-PAmCherry was perfomed by single cell irradiation with a 405 nm light laser enhancing respectively the green and red light fluorescence emission.
Photoconversion is easier to perform because it switches a fluorescent state to a different fluorescent state (meaning in color and other optical properties). Thus, MSCs transfected with photoconvertible FP were detectable and easy to photoconvert. Photoconversion of MyoD-mEos3.2 was performed by irradiation with a single cell light in violet spectrum (a 405nm laser light) switching the Ex_{max} from 507 to 572 nm and the Em_{max} from 516 to 580 nm.

Gene expression analysis. In order to evaluate the gene expression levels of mRNA target genes of MyoD, MSC culture samples were lysed for RNA extraction after 72 hours from DNA transfection. RNA was extracted from the MSC culture samples using miRNeasy Mini Kit (Qiazol™) following manufacturer's instructions. The quantity and

purity of extracted RNA was measured via spectrophotometry (ND-1000; NanoDrop™). cDNA was synthesized from total RNA using the High-Capacity cDNA Reverse Transcription Kit (Applied Biosystems™). Relative mRNA expression levels of Myogenin (Myog), Creatin Kinase M-Type (CKM) were measured via quantitative real-time polymerase chain reaction (qRT-PCR), normalized to 18s rRNA, using TaqMan™ Reagents (Applied Biosystems™) on an 7900HT Fast Real-Time PCR System (Applied Biosystems™). For further details see Chapter 2.1, “Methods”, “Gene expression analysis” section.

Statistical analyses. The experimental data were analyzed by one-way analysis of variance (ANOVA) and Tukey’s post-hoc test or with Student’s t-test for a direct comparison of two groups. Associations with $p < 0.05$ were considered significant. Statistical tests were done using GraphPad Prism 7.0 software. ns P >0.05; * P <0.05; ** P <0.01; *** P <0.001; **** P <0.0001.

References

1. Patterson GH, Lippincott-Schwartz J. A photoactivatable GFP for selective photolabeling of proteins and cells. Science. 2002 Sep 13;297(5588):1873-7.
2. Subach FV, Patterson GH, Manley S, Gillette JM, Lippincott-Schwartz J, Verkhusha VV. Photoactivatable mCherry for high-resolution two-color fluorescence microscopy. Nat Methods. 2009 Feb;6(2):153-9.
3. Zhang M, Chang H, Zhang Y, Yu J, Wu L, Ji W, Chen J, Liu B, Lu J, Liu Y, Zhang J, Xu P, Xu T. Rational design of true monomeric and bright photoactivatable fluorescent proteins. Nat Methods. 2012 May 13;9(7):727-9. doi: 10.1038/nmeth.2021.

4. Habuchi S, Ando R, Dedecker P, Verheijen W, Mizuno H, Miyawaki A, Hofkens J. Reversible single-molecule photoswitching in the GFP-like fluorescent protein Dronpa. Proc Natl Acad Sci U S A. 2005 Jul 5;102(27):9511-6.
5. Ando R, Mizuno H, Miyawaki A. Regulated fast nucleocytoplasmic shuttling observed by reversible protein highlighting. Science. 2004 Nov 19;306(5700):1370-3.
6. Bergeland T, Haugen L, Landsverk OJ, Stenmark H, Bakke O. Cell-cycle-dependent binding kinetics for the early endosomal tethering factor EEA1. EMBO Rep. 2008 Feb;9(2):171-8.
7. Deryusheva S, Gall JG. Dynamics of coilin in Cajal bodies of the Xenopus germinal vesicle. Proc Natl Acad Sci U S A. 2004 Apr 6;101(14):4810-4.
8. Schmierer B, Hill CS. Kinetic analysis of Smad nucleocytoplasmic shuttling reveals a mechanism for transforming growth factor beta-dependent nuclear accumulation of Smads. Mol Cell Biol. 2005 Nov;25(22):9845-58.
9. Cimica V, Chen HC, Iyer JK, Reich NC. Dynamics of the STAT3 transcription factor: nuclear import dependent on Ran and importin-β1. PLoS One. 2011;6(5):e20188.
10. Rey O, Papazyan R, Waldron RT, Young SH, Lippincott-Schwartz J, Jacamo R, Rozengurt E. The nuclear import of protein kinase D3 requires its catalytic activity. J Biol Chem. 2006 Feb 24;281(8):5149-57.
11. Shcherbakova DM, Sengupta P, Lippincott-Schwartz J, Verkhusha VV. Photocontrollable fluorescent proteins for superresolution imaging. Annu Rev Biophys. 2014;43:303-29.
12. Manley S, Gillette JM, Patterson GH, Shroff H, Hess HF, Betzig E, Lippincott-Schwartz J. High-density mapping of single-molecule trajectories with photoactivated localization microscopy. Nat Methods. 2008 Feb;5(2):155-7.
13. Das S, Yin T, Yang Q, Zhang J, Wu YI, Yu J. Single-molecule tracking of small GTPase Rac1 uncovers spatial regulation of membrane

translocation and mechanism for polarized signaling. Proc Natl Acad Sci U S A. 2015 Jan 20;112(3):E267-76.

Supplementary Figures

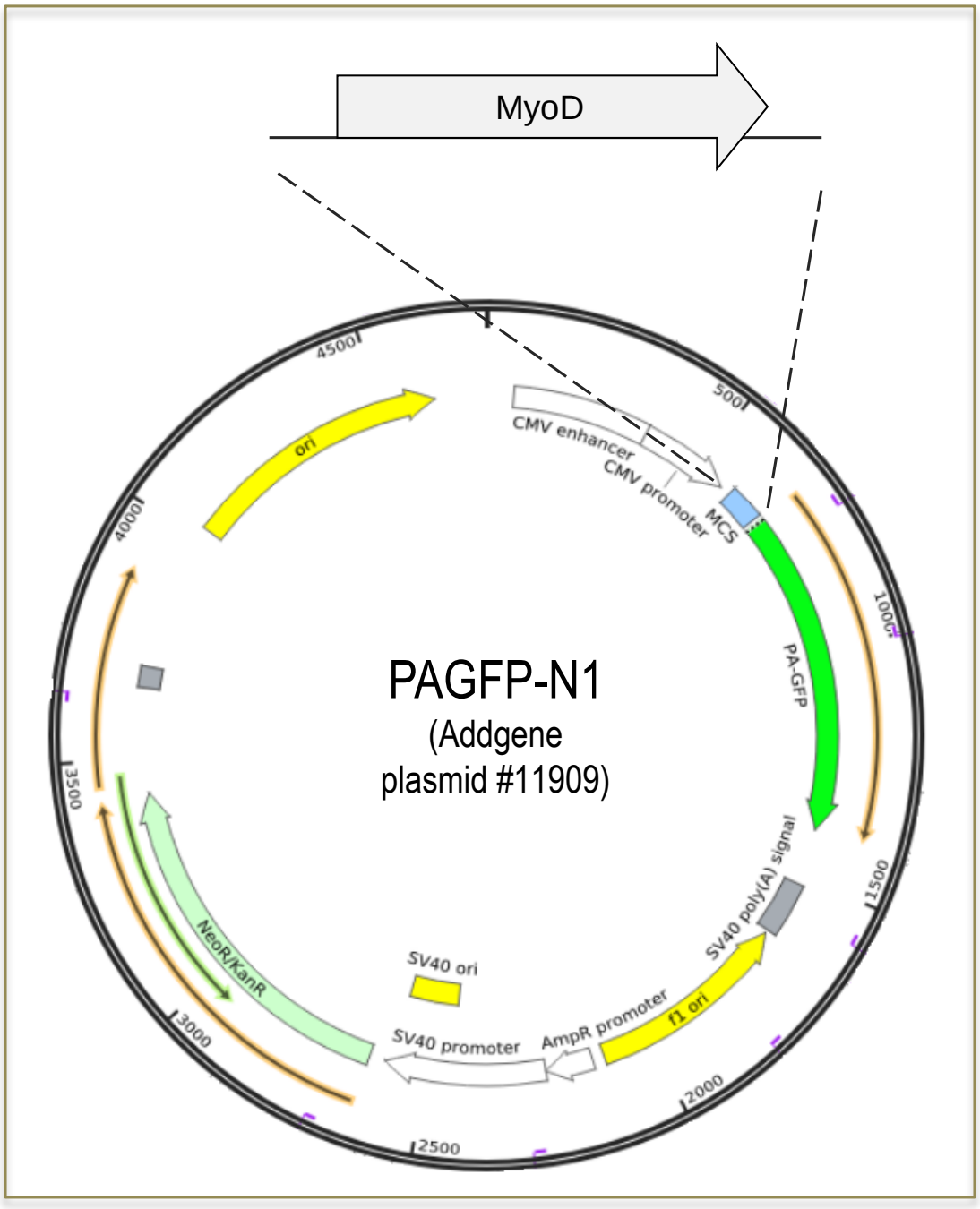

Suppl. Fig. 2.2.1 Schematic representation of the plasmid pMyoD-PAGFP. The gene MyoD was inserted at N-terminus pf PAGFP in the pPAGFP-N1 (Addgene, plasmid #11909). This plasmid is identical to the Clonotech pEGFP-N1 except for four mutations in the PAGFP sequence (L64F/T65S/V163A/T203H).

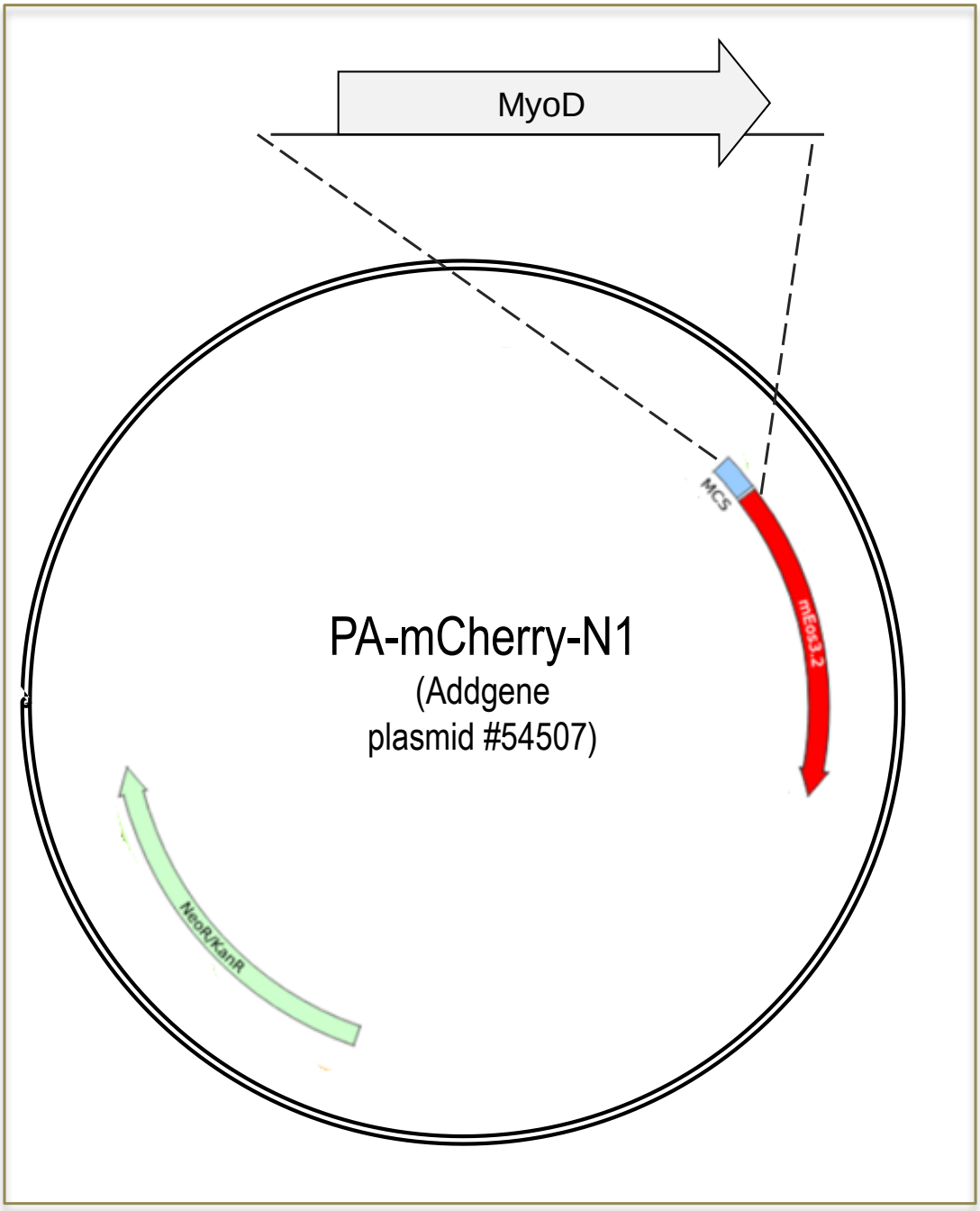

Suppl. Fig. 2.2.2 Schematic representation of the plasmid pMyoD-PAmCherry. The gene MyoD was inserted at N-terminus of PAmCherry in the PAmCherry-N1 (Addgene, plasmid #54507). Full plasmid sequence is not available but depositor provided the following information: bacterial and mammalian antibiotic resistance are against Kanamycin and neomycin, respectively; the vector is classified as high copy number plasmid.

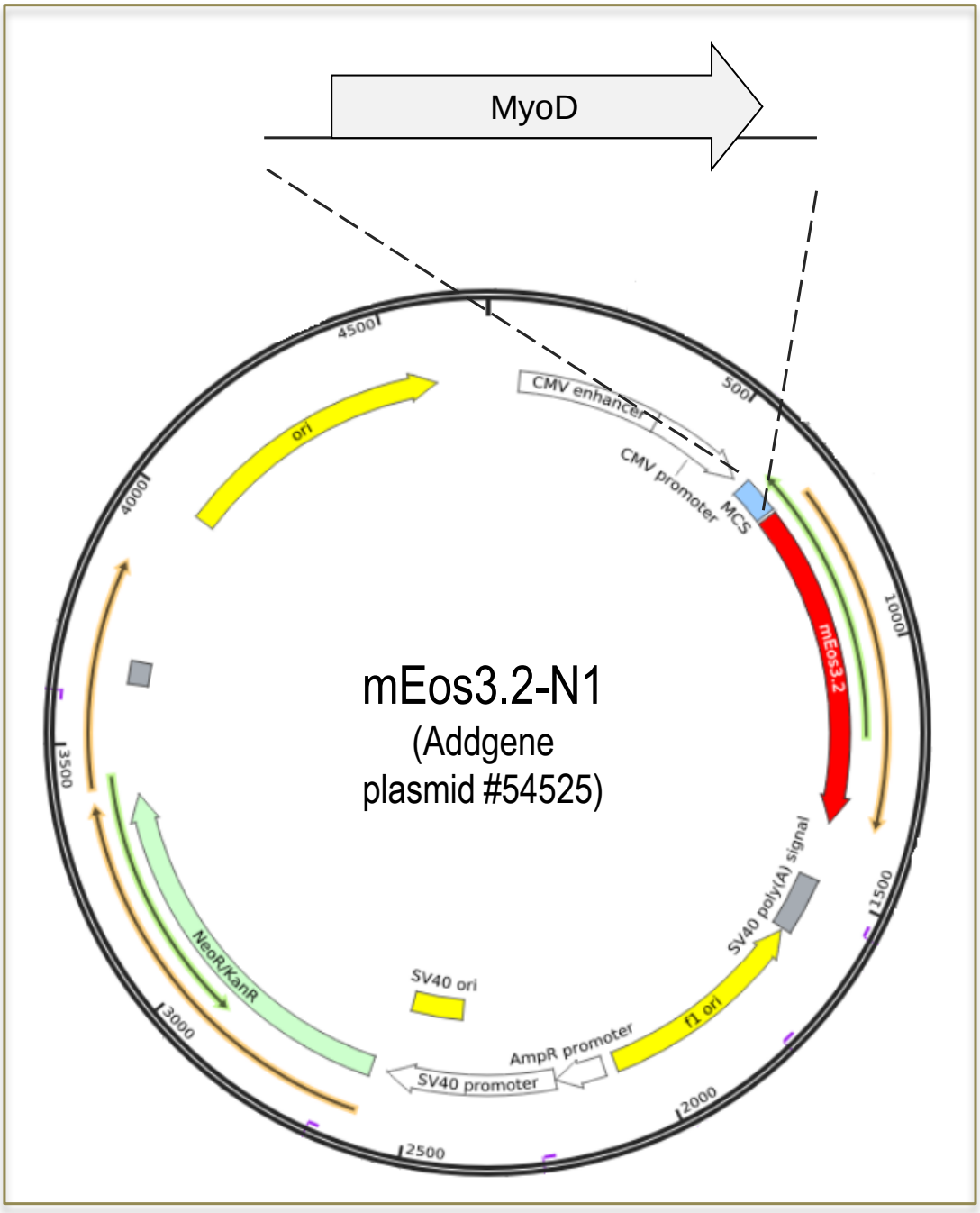

Suppl. Fig. 2.2.3 Schematic representation of the plasmid pMyoD-mEos3.2. The gene MyoD was inserted at N-terminus of mEos3.2 in the mEos3.2-N1 (Addgene, plasmid #54525).

FP	Condition of perturbation		Ex_{max}	Em_{max}
PAGFP	405 nm		504	517
PAmCherry	405 nm		564	595
mEOS3.2	405 nm	**Pre**	507	516
		Post	572	580

Suppl. Table 2.2.1 Optical properties of photosensitive fluorescent proteins.The table shows changes in Ex_{max} and Ex_{max} pre- and post-activation/conversion. Ex_{max}:Excitation maximum; Em_{max}: Emission maximum.

CHAPTER 3: Molecular Dynamics characterization of fluorescent transcription factors

Summary

In order to generate a fluorescent tool for nucleocytoplasmic shuttling study, the supernegative (-30)GFP has been fused to the myogenic transcription factor (TF) MyoD. The fluorescent complex resulted able to pass the plasmatic membrane when complexed with cationic lipids showing high protein internalization efficiency and great nucleocytoplasmic shuttling. Unexpectedly, (-30)GFP inhibited the activity of MyoD and the engineered complex resulted completely inactive. The aim of the present work was to deepen the observed inhibitory effect by a molecular dynamics approach. I generated a model of the molecular complex, (-30)GFP-MyoD, characterized by the (-30)GFP and the MyoD Basic Helix Loop Helix (BHLH) domain, that represents the functional core of the TF. I compared the complex with a control model, PAGFP-MyoD, composed by a photoactivatable GFP (PAGFP) and the MyoD BHLH domain. For each model I created four configurations interfacing the BHLH domain in different position respect to the fluorescent protein. Thus, I analyzed structural rearrangements, trajectories and interaction energies between the two molecules forming the complex. Computational results showed stronger interaction energies between (-30)GFP and MyoD domain respect to the interaction between PAGFP and MyoD. Overall, (-30)GFP-MyoD MD simulations suggested a charge-guided interaction mechanism that could alter the BHLH domain and consequently the MyoD transcriptional activity.

Introduction

In the design and development of fluorescent molecules for nucleocytoplasmic shuttling detection, the experimental validation could be not enough to provide a complete overview of the molecule behavior. Molecular dynamics (MD) simulations support the experimental analysis by modeling molecules at a nanoscale levels considering information about structures, atomic properties and interaction energies. This computational approach is widely used for molecular docking-based screening and also for inter-molecular interface analysis (protein-protein and protein-DNA) [1-4].
Previous experimental studies on the development of fluorescent variants of the myogenic transcription factor (TF) MyoD arouse concerning aspects mainly related to the influence of the label on the TF functionality. In my Ph.D. thesis project, I developed five recombinant variants of MyoD fused to different fluorescent probes (FP): Tat-GFP, (-30)GFP, PAGFP, PAmCherry, mEos3.2. Analyzing the transcription promoting activity of the recombinant TF, PAGFP was the only label that, when fused to the TF, significantly promoted the transcription of target genes of MyoD (Fig. 2.2.5, 2.2.6). On the opposite, (-30)GFP was the probe that showed a total inhibitory effect on MyoD activity (Fig. 2.1.9, 2.1.10). This last fluorescent protein is a supernegative GFP that passes the membrane when complexed with cationic molecules. (-30)GFP-MyoD showed great qualities in terms of protein transduction efficiency, protein localization and nucleocytoplasmic shuttling. Thus, the total inhibitory effect resulted unexpected and required further investigations. An hypothesis for this inhibitory effect could be that the peculiar surface negative charges of the (-30)GFP interacted with positive charges characterizing the Basic Helix Loop Helix (BHLH) binding domain of MyoD and thus, interfered

with MyoD dimerization or DNA binding (Fig. 3.1). A good option to analyze the molecular behavior at the atomistic scale is represented by computational approach based on molecular dynamics methods.

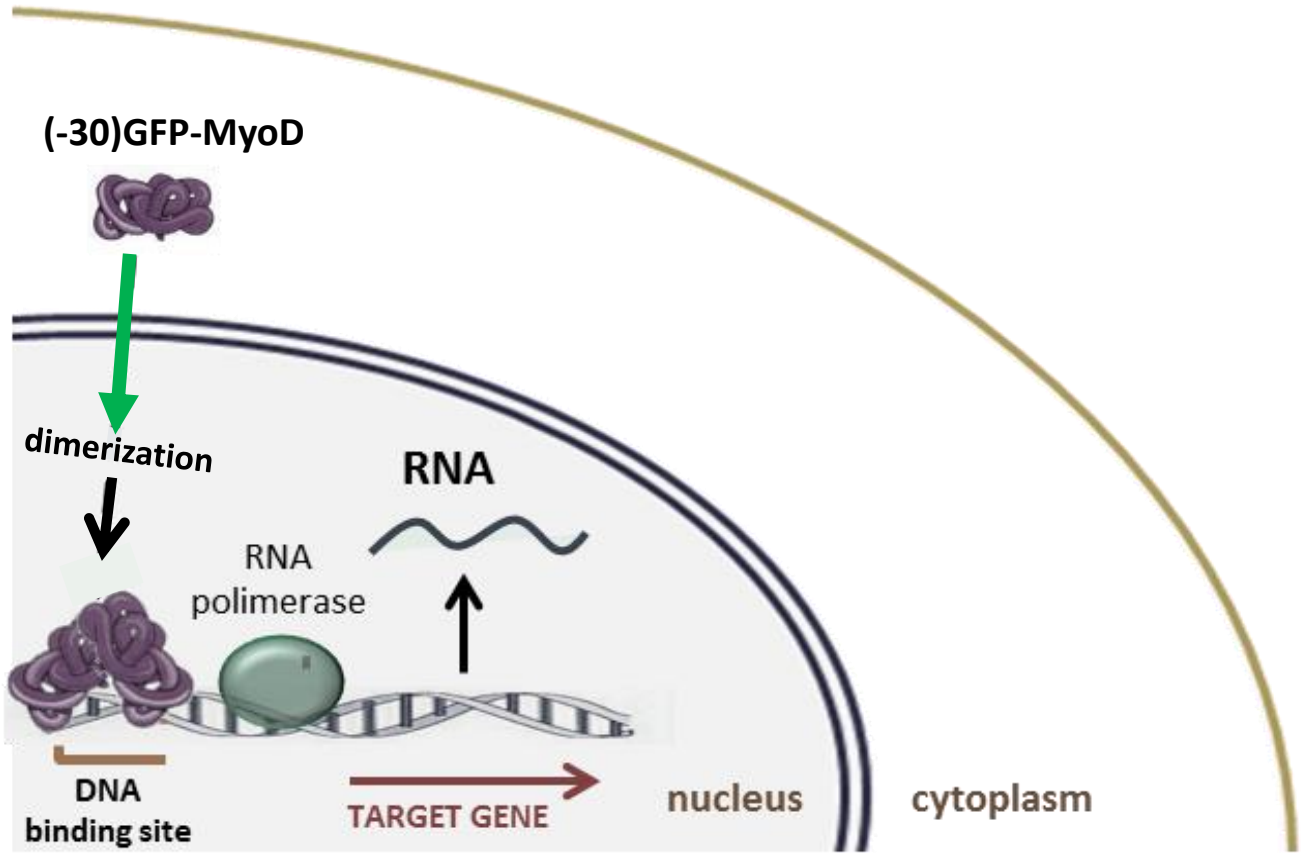

Fig. 3.1 Graphical representation of (-30)GFP-MyoD intracellular dynamics. In physiological conditions, the protein should migrate from cytoplasm to the nucleus where will form a homo- or hetero-dimer. In dimerized form, the complex (-30)GFP-MyoD will bind DNA to promote the transcription of specific target genes. Previous experiments showed efficient nuclear import of the complex but an inhibitory effect on the transcription promoting activity. This evidence suggested an interference in dimerization or DNA binding processes.

The present work consists in a molecular dynamics study of two fluorescent variants of MyoD ((-30)GFP-MyoD and PAGFP-MyoD) with the aim to investigate the causes of the inhibitory effect of (-30)GFP on MyoD activity. I generated two molecular models, one characterized by MyoD BHLH domain and (-30)GFP and the second by MyoD domain

and PAGFP. Since MyoD-PAGFP was the fluorescent variant of MyoD that experimentally showed a positive transcription promoting activity, the second computational model was used as control. I examined molecular dynamics simulations by analyzing structural rearrangements and stability and by evaluating non-bonded interaction enegies between the two molecules involved in the complex formation.

Molecular Dynamics

In molecular dynamics (MD) simulations atoms move according to classical Newton's equation of motion (3.1)

$$m_a \vec{r}_a = -\frac{\partial U_{tot}}{\partial \vec{r}_a} \tag{3.1}$$

where m_a is representative of the mass of the atom a and the r_a is the atomic position. U_{tot} represents the total potential energy that depends on all atomic positions and all atomic motions. Since U_{tot} describes all the interactions between atoms, it defines the relationship part of the MD simulation, the force field.

Force field mathematical function (3.2) describes the interaction energies dividing them into bond and non-bonded terms.

$$U_{tot} = U_{bond} + U_{angle} + U_{dihedral} + U_{VdW} + U_{Coulomb} \tag{3.2}$$

U_{bond}, U_{angle}, $U_{dihedral}$ describe bonded interactions while the last two terms describe non-bonded interaction energies.

Bond energy terms

The first three terms define the characteristics related to the covalent bonded interactions, such as bond length, angle and torsion.

U_{bond} describes energy of the covalent bond between two atoms. It is represented by the covalent bond energy function (3.3)

$$U_{bond} = \sum_{bonds} k_r(r - r_0)^2 \tag{3.3}$$

where r is the bond length between atoms, r_0 is the bond length at the moment when all the other force field terms are equal to zero and k_r is the harmonic oscillator constant.

U_{angles} represents the angles between two pairs of covalent bonds unified by a single atom at the vertex. The angle energy function is described by a harmonic function (3.4)

$$U_{angle} = \sum_{angles} k_\theta(\theta - \theta_0)^2 \tag{3.4}$$

where θ is the current angle, θ_0 is bond angle value when all other force field terms are equal to zero and k_θ is the force constant specific to each triplet of atoms.

$U_{dihedral}$ defines angles between four atoms covalently bonded. The central bond is subjected to a torsional angle φ described by dihedral angle energy function (3.5)

$$U_{dihedral} = \sum_{dihedral} k_n \cos(\varphi)^n \tag{3.5}$$

where k_n is the constant specific of the covalent bonds, and n is the number of energetic minima.

Non-bonded energy terms

In addition to covalent bonded interactions, atoms interact each other by non-bonded interactions. Non-covalent bonds include electrostatic interactions, hydrogen bonds, hydrophobic interactions and Van der Waals interactions. Force field mainly divide non-bonded interactions into two main components: electrostatic Coulomb forces and Van der Waals (VdW) interactions.

$UCoulomb$ is the electrostatic interaction energy and describes the interaction between atoms with opposite charge or with a permanent dipole. The interaction is described by the Coulomb energy function (3.6)

$$U_{Coulomb} = \sum_{i} \sum_{J>i} \frac{q_i q_j}{4\pi\epsilon_0 r_{ij} \epsilon_r} \tag{3.6}$$

where q is the charge of atoms i and j, ϵ_0 *and* ϵ_r are the dielectric constants of vacuum (=1) and medium (i.e. =80 for water), and r_{ij} is the distance between the atoms i and j.

U_{VdW} is the Van der Waals interaction energy and represents all the non-bonded interactions that do not involve electrostatic interactions. The Van der Waals energy function is described as following

$$U_{VdW} = \sum_{i} \sum_{j>i} 4\epsilon_{ij} \left[\left(\frac{\sigma_{ij}}{r_{ij}} \right)^{12} - \left(\frac{\sigma_{ij}}{r_{ij}} \right)^{6} \right] \tag{3.7}$$

where r_{ij} is the distance between the atoms i and j and σ_{ij} is the distance required to produce an energy equal to zero (collision parameter), ϵ_{ij} is the Van der Waals well depth (interaction energy minimum). As described by the equation, the Van der Waals forces are inversely proportional to the distance between atoms. At small

distances, repulsion between atoms leads to large positive values of U_{VdW}.

Molecular dynamics solves the classical Newton's equation of motion (3.1) integrating the forces acting on the generalized coordinates by time. Given the coordinates of atoms and the atomic topologies, MD uses an algorithm that computes the acting forces and mass distribution at each time step analyzing acceleration and velocities of the moving bodies.

Results

Homology modeling of PAGFP and (-30)GFP

To generate 3D models of the PAGFP and (-30)GFP, two of the five probes used in the experimental characterization, I first aligned each amino acidic sequence with the photoactivatable GFP 3D model deposited in Research Collaboratory for Structural Bioinformatics - Protein Data Bank (RCSB-PDB) (PDB ID: 3GJ2). The sequence alignments revealed high identity in both cases: 97% identity for PAGFP and 91% identity in the case of (-30)GFP alignments. Thus, I used 3GJ2 model as template for 3D homology modeling of both PAGFP and (-30)GFP. Surface electrostatic potential analysis of the 3D generated models of the obtained structures revealed a (-30)GFP surface charge of -28, similar to theoretical -30, and showed a weak negative charge (-6) of the PAGFP surface, biochemically similar to standard GFP [9].

The 3D structures obtained for (-30)GFP and PAGFP were then minimized and equilibrated for 1 ns in explicit water and under NPT

conditions. RMSD values calculated from equilibration trajectories are shown in Suppl. Fig. 3.1.

3D model of MyoD BHLH domain

The molecular model of MyoD was generated starting from the 1MDY.pdb available in RSCB-PDB that is a homo-dimer of MyoD BHLH domain-DNA complex. As highlighted in Suppl. Fig. 3.2A and B, from the 1MDY.pdb I extracted the monomeric BHLH domain of MyoD. Analyzing the residues of the monomeric domain, I highlighted the key amino acids involved in dimerization (Suppl. Fig. 3.2C) and in DNA binding (Suppl. Fig. 3.2D). As shown in Suppl. Fig. 3.2C and D, residues involved in dimerization are mainly hydrophobic while amino acids that interact with DNA are mainly positively charged and they belong for the most to the basic region (108-125aa) (Suppl. Fig. 3.2E).
The complete structure of the TF has not yet been crystallized and solved by X-ray diffraction, hence the 3D model of the entire structure is not available. The reasons are mainly related to the folding and structural properties. Using the protein structure prediction servers PSI-blast based secondary structure PREDiction (PSIPRED v3.3) and DISOrder PREdiction (DISOPRED3), I analyzed the structure of MyoD and I observed that, except for the BHLH domain, MyoD resulted predominantly a disordered structure (Suppl. Fig. 3.3). Suppl. Fig. 3.4 confirms the protein disorder and shows a strong prediction of two alpha-helix structures in proximity of the known BHLH domain and a weak prediction of two very short helixes in other two regions of the sequence.

MyoD-GFP complex models for MD simulations

In order to study the interactions between MyoD and (-30)GFP or the PAGFP, I generated two molecular models of the (-30)GFP-MyoD and PAGFP-MyoD complexes. Since MyoD model was characterized by the only core of the protein, I supposed different positions of the MyoD BHLH domain respect to the GFP and thus, I created four different configurations of the two models of the molecular complexes (Suppl. Fig. 3.5). MD simulations were carried out for 5 ns with NAMD (NAnoscale Molecular Dynamics) software together with the Visual Molecular Dynamics (VMD) software. For further details see "Methods", "MD configurations set-up" section.
For each configuration I analyzed structural rearrangements pre- and post-simulation and structural stability by RMSD calculation of trajectories. Furthermore, I evaluated non-bonded interaction energies to quantify the interaction between MyoD BHLH domain and the specific GFP.

Structure analysis

1st configuration
As for each configuration, I analyzed the trajectories of the MD simulations observing the complexes rearrangements in pre- and post-simulation (Fig. 3.2). At the end of the run, I highlighted the residues involved in contacts between each GFP and the MyoD BHLH domain (Fig. 3.3).
As shown in Fig. 3.2, starting from the same initial configuration, the MyoD domain showed an opposite behavior in association with PAGFP or (-30GFP). While in presence of PAGFP the domain migrated perpendicular to the FP, in the case of (-30)GFP, MyoD maintained its helix 1 longitudinal to the FP reducing the distances

between the two molecules and promoting the contact with the basic region, as shown in Fig. 3.3C.

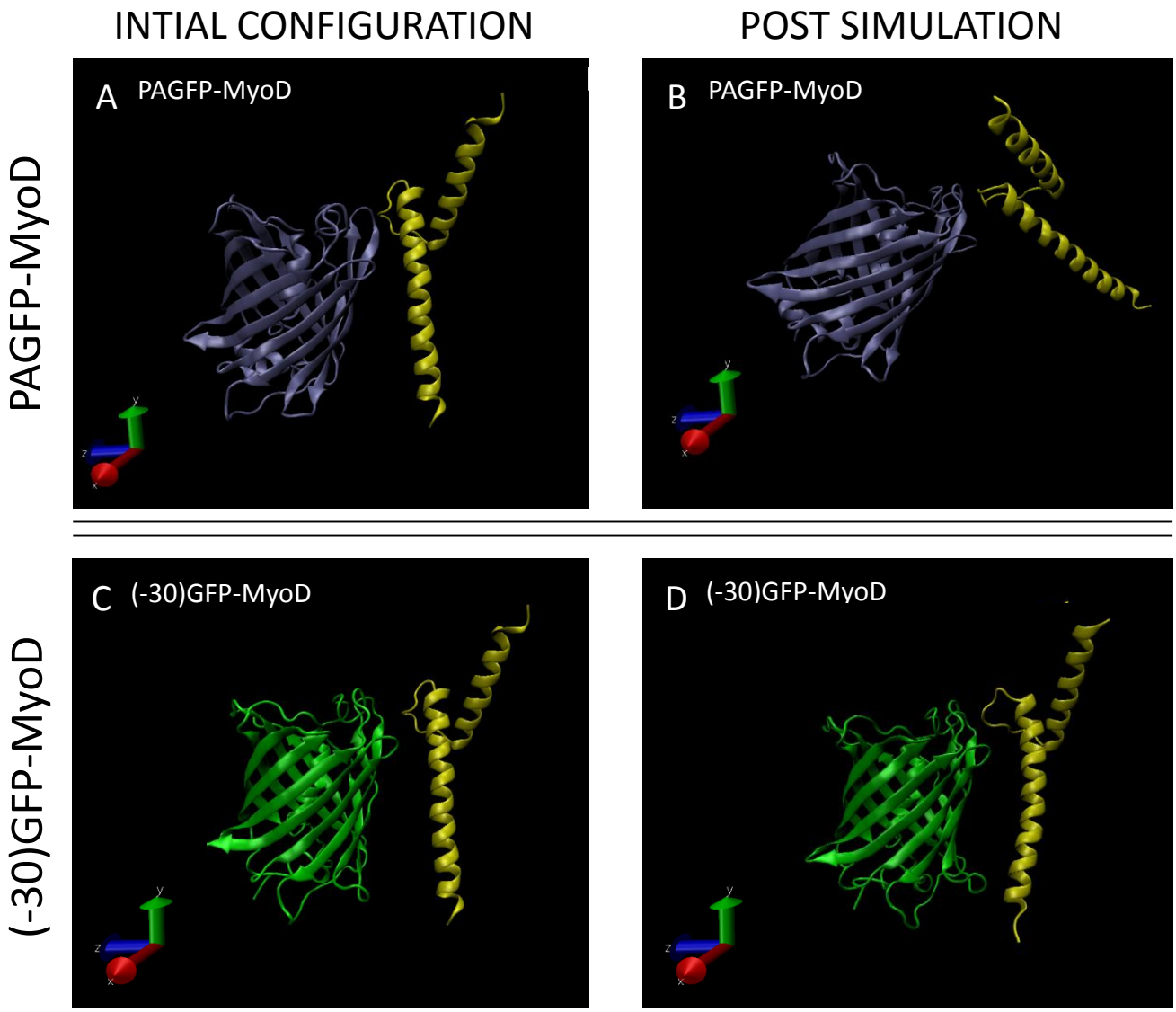

Fig. 3.2 VMD cartoon representation of pre-(A and C) and post-(B and D) simulation of 1st configuration. PAGFP is represented in iceblue, (-30)GFP in green and MyoD domain in yellow.

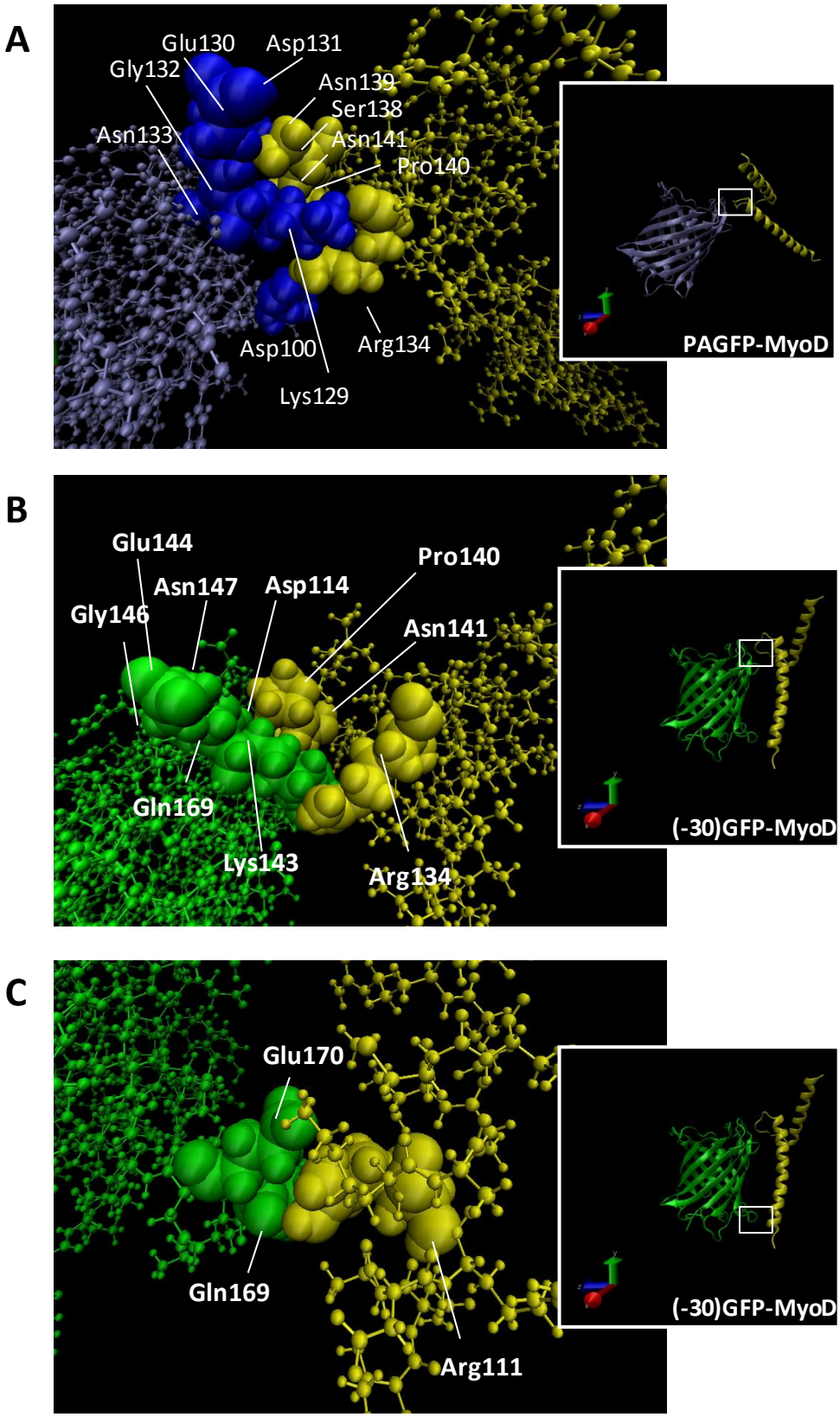
A
Glu130
Asp131
Gly132
Asn139
Ser138
Asn133
Asn141
Pro140
Asp100
Arg134
Lys129
PAGFP-MyoD
B
Glu144
Pro140
Asn147
Asp114
Gly146
Asn141
Gln169
Lys143
Arg134
(-30)GFP-MyoD
C
Glu170
Gln169
Arg111
(-30)GFP-MyoD

Fig. 3.3 VMD VDW representation of residues involved in intermolecular contacts between the fluorescent protein and MyoD after MD simulation of the 1st configuration. The inset represents the entire model highlighting the region detailed. PAGFP interacted with MyoD domain at the loop region (A). (-30)GFP interacted with MyoD domain at both the loop region (B) and the basic region (C). PAGFP is represented in iceblue, (-30)GFP in green and MyoD domain in yellow. All background residues are represented in CPK representation.

Analyzing the residues in contact between the two molecules, we can observe that both models maintained contacts with the loop of MyoD (Fig. 3.3A, B). Pro140, Asn141 and Arg134 are common residues of the MyoD loop that interacted with both PAGFP and (-30)GFP. Fig. 3.3 C instead, shows specific non-bonded interactions between (-30)GFP and MyoD domain at the basic region. In specific, the interactions involve the positively charged Arg111, the negative Glu170 and the charge-neutral Gln169. Arg111 is a key residue of the BHLH domain involved in the DNA binding.

The comparison of the RMSD calculated from trajectories confirmed what previously observed. RMSD of (-30)GFP-MyoD reached stability after about 2500 ps while PAGFP-MyoD resulted completely unstable (Fig. 3.4).

The structural analysis of MD simulations of 1st configuration suggested a charge-based attractive influence of the (-30)GFP toward MyoD basic region while PAGFP did not show any specific attractive effect leaving the monomer free to move.

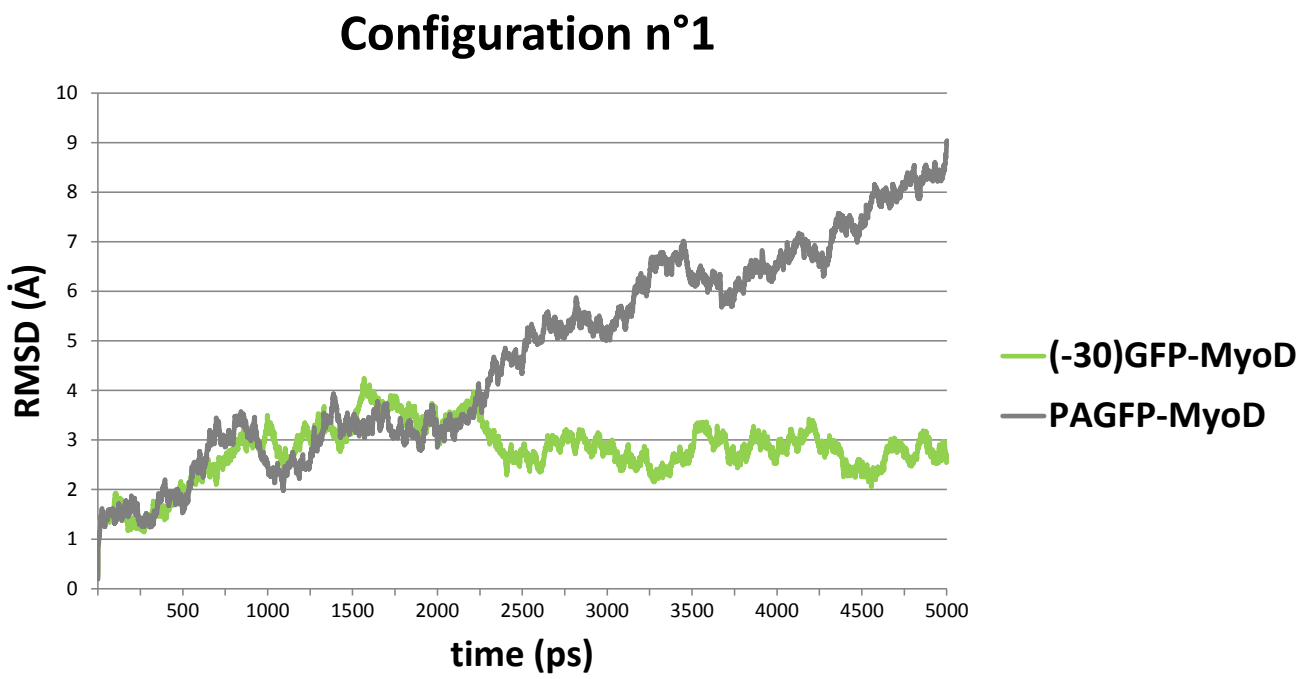

Fig. 3.4 Comparative RMSD graph of the 1st configurations trajectories. Green curve refers to (-30)GFP-MyoD while grey curve represents PAGFP-MyoD.

2nd configuration

Analyzing post-simulation models of 2nd configuration, we can observe that MyoD domain move in a stochastic way independently from the type of the FP. In the model of (-30)GFP-MyoD, the MyoD domain lost completely any contact with the FP (Fig. 3.5D). In the model of PAGFP-MyoD, the MyoD domain freely moved around the FP maintaining a single-residue contact between two positively charged residues: PAGFP-Lys24 and MyoD-Arg119 (Fig. 3.6).

RMSD comparison confirmed the instability of the GFP-MyoD complexes observed showing increasing RMSD values for both models (Fig. 3.7).

Structural analyses of the 2nd configuration simulations did not suggest any particular interaction element that could interfere with MyoD domain dynamics. MyoD is free to move in both cases.

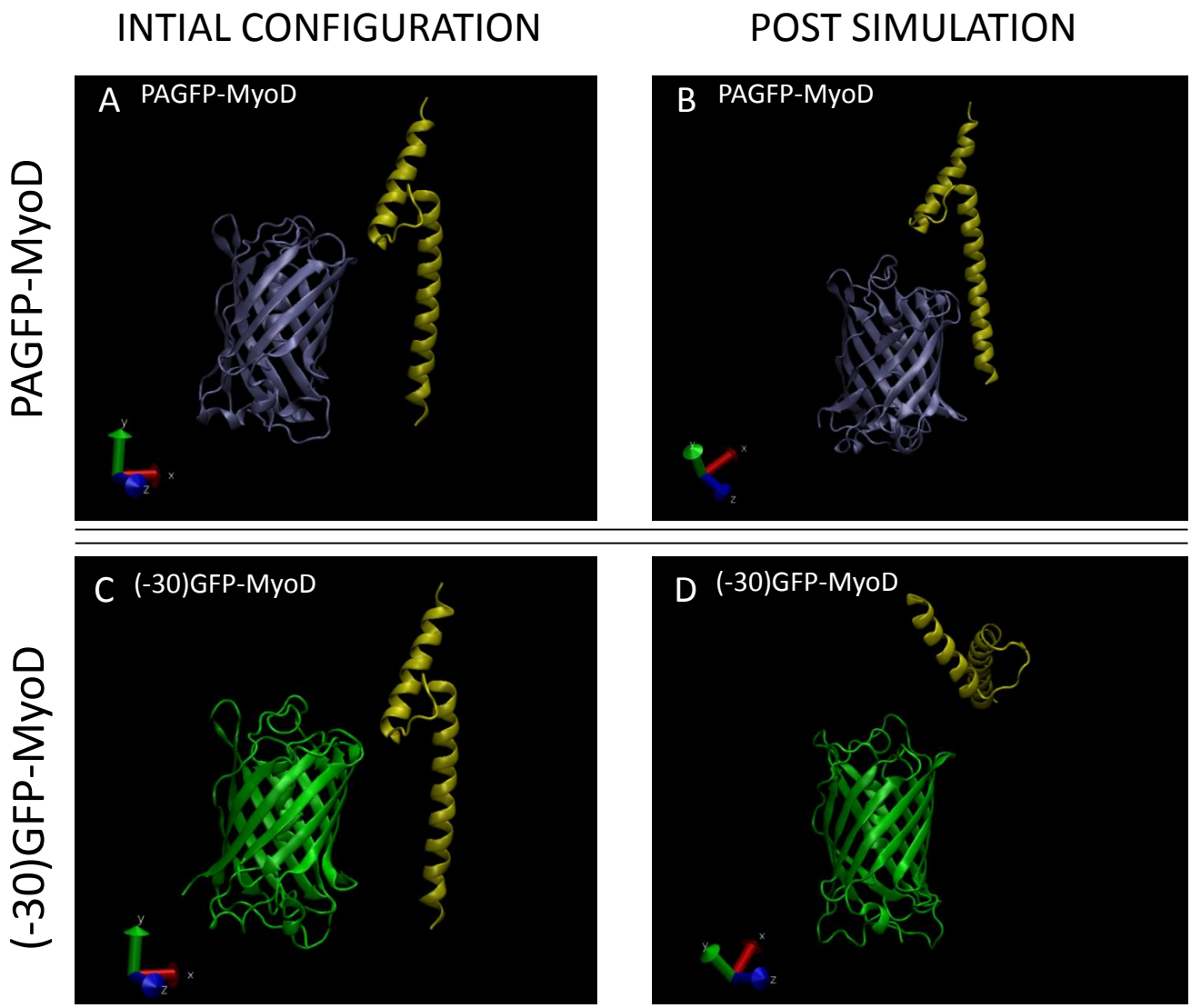

Fig. 3.5 VMD cartoon representation of pre-(A and C) and post-(B and D) simulation of the 2nd configurations. PAGFP is represented in iceblue, (-30)GFP in green and the monomeric BHLH domain in yellow.

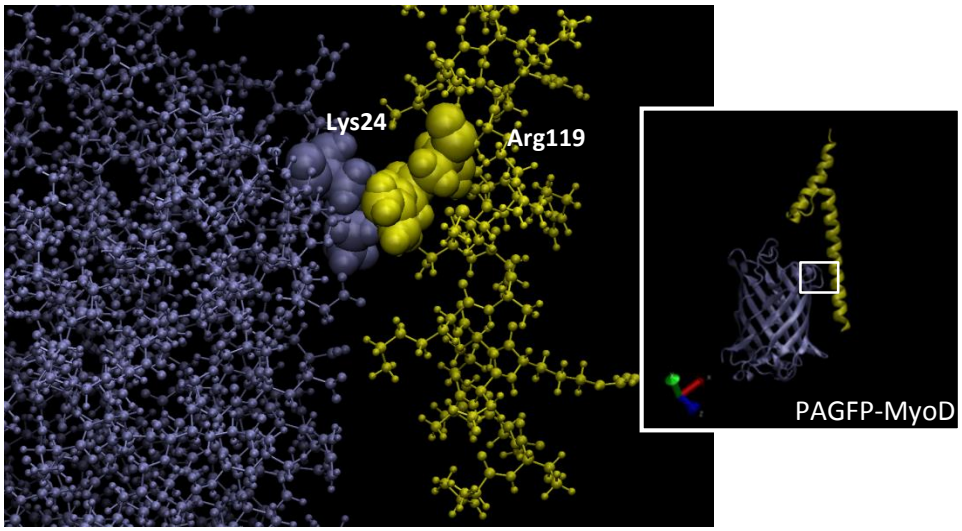

Fig. 3.6 VMD VDW representation of residues involved in intermolecular contacts between the fluorescent protein and MyoD after MD simulation of the 2nd configurations. The inset represents the entire model highlighting the region detailed. PAGFP interacted with MyoD domain with a residue of the basic region PAGFP is represented MyoD domain in yellow. All background residues are represented in CPK representation.

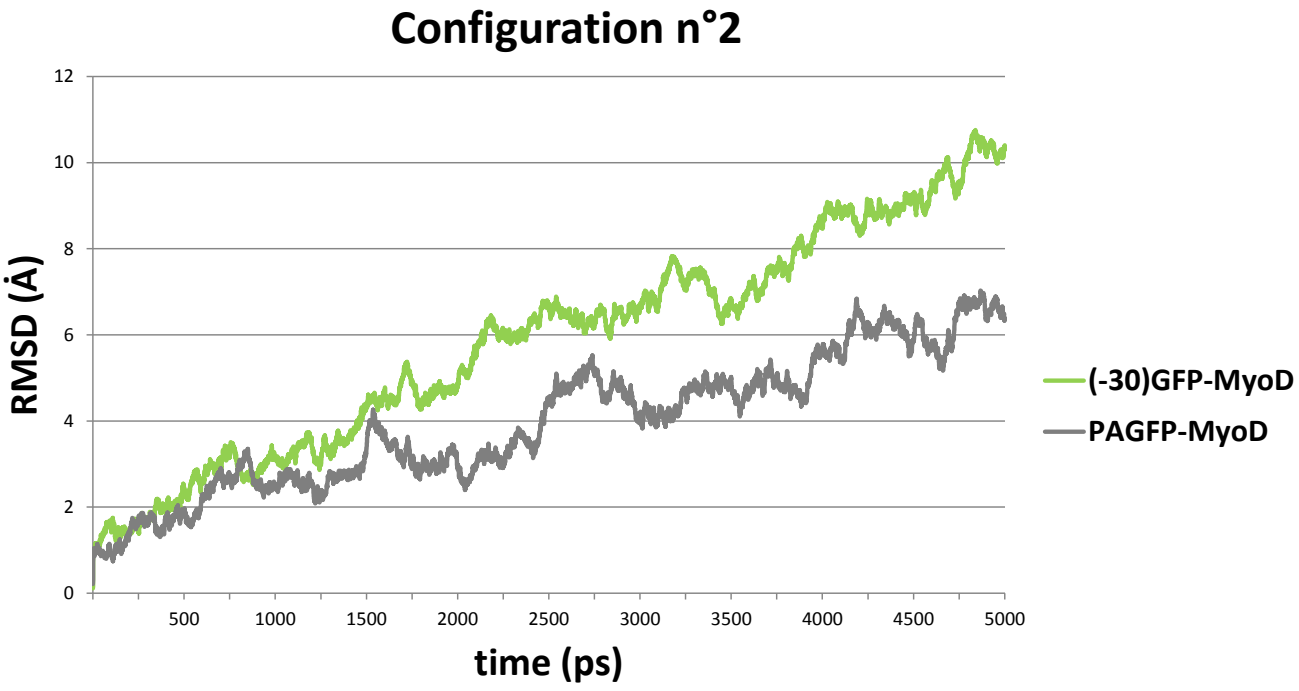

Fig. 3.7 Comparative RMSD graph of the 2nd configurations trajectories. Green curve refers to (-30)GFP-MyoD while grey curve represents PAGFP-MyoD.

3rd configuration

MD simulations of the PAGFP-MyoD and (-30)GFP-MyoD models set with the coordinates of the 3rd configuration arouse interesting considerations.

As in the PAGFP-MyoD model set in the 1st configuration, MyoD domain freely moved around the FP positioning the helix 2 far from and perpendicular to the PAGFP (Fig. 3.8). It maintained contacts with three residues of the basic region of MyoD BHLH domain. As shown in Fig. 3.9A, the interaction between MyoD and PAGFP was characterized by positive, negative, charge-neutral residues with no particular charge-dependent influence.

(-30)GFP-MyoD behaved similarly to the model of the 1st configuration, too. In fact, after an apparent stochastic free movement of the MyoD domain, it re-localized with the helix 1 longitudinal to the FP. The close proximity of the domain is confirmed by the contacts of both the basic region and the dimerization residues (Fig. 3.9B and C). It is also important to observe that the non-bonded interactions between MyoD basic region and (-30)GFP are charge-based contacts (Fig. 3.9C). (-30)GFP interacted with two negatively charged residues (Glu46 and Asp129) while MyoD offered two key positively charged amino acids involved in DNA binding (Suppl. Fig. 3.2D). It is interesting to notice that even if residues involved are different, in both configurations n°1 and n° 3, (-30)GFP interacted with basic region of MyoD BHLH domain, enforcing the hypothesis of a charge-guided mechanism.

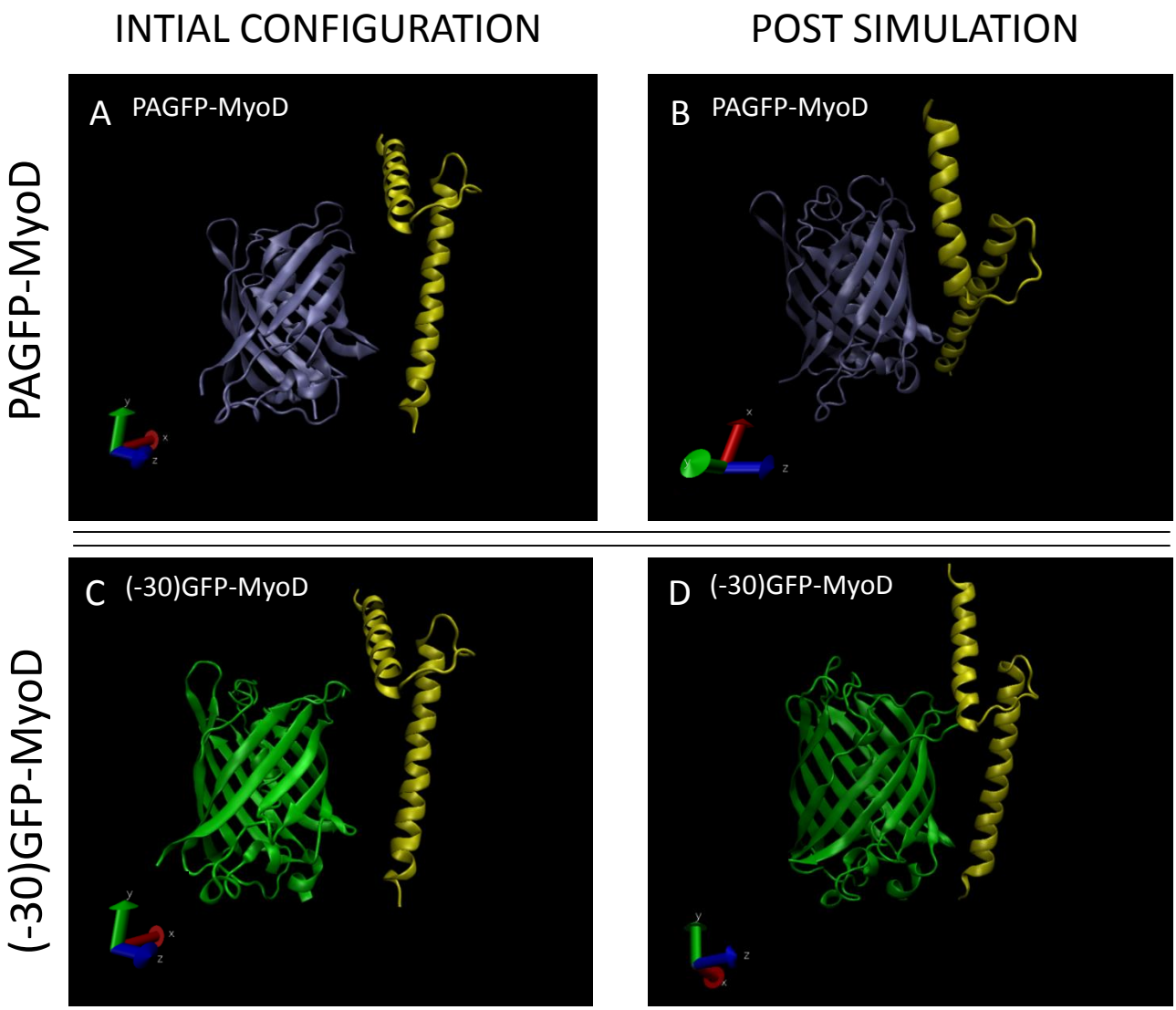

Fig. 3.8 VMD cartoon representation of pre-(A and C) and post-(B and D) simulation of the 3rd configurations. PAGFP is represented in iceblue, (-30)GFP in green and the monomeric BHLH domain in yellow.

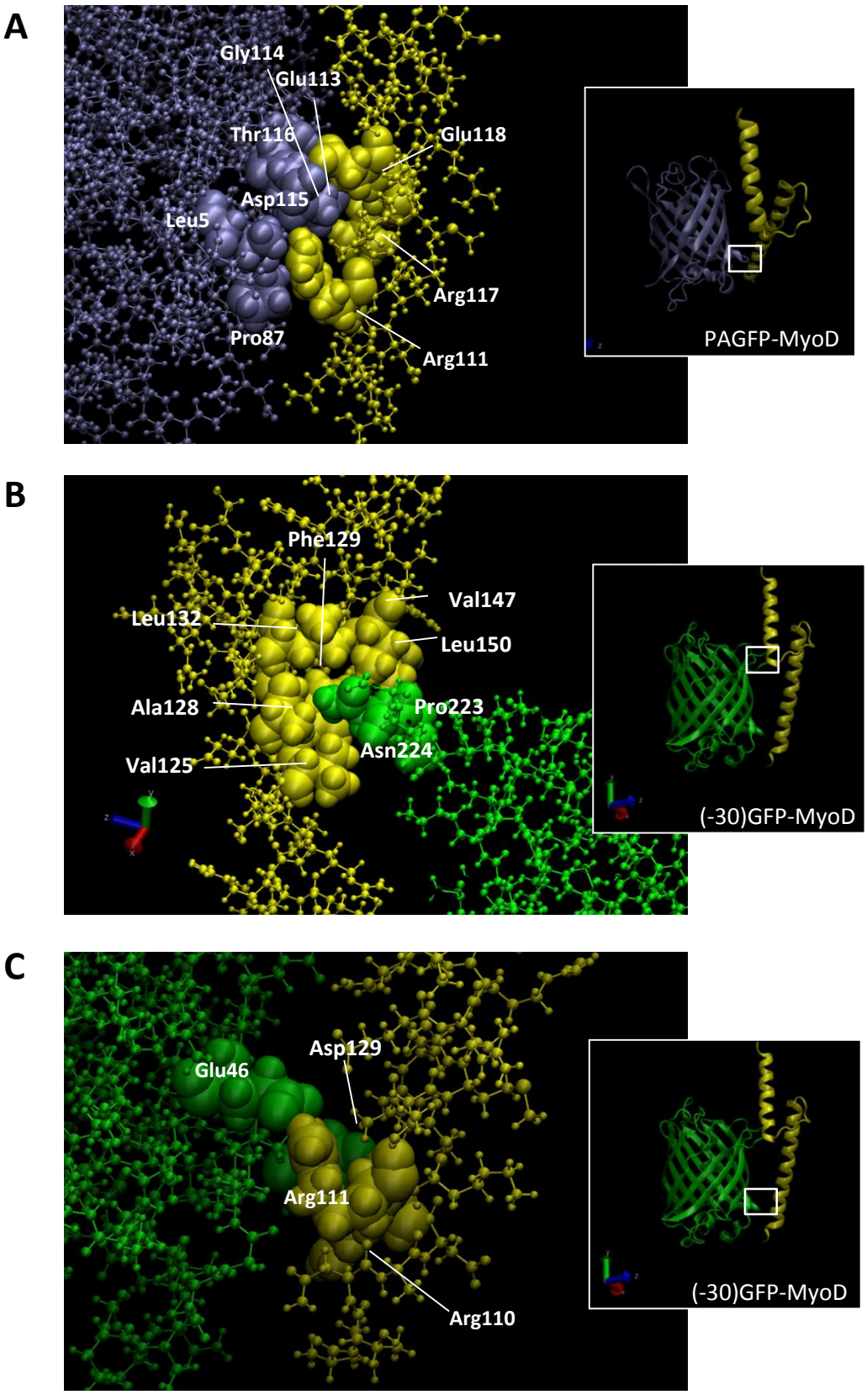
A
Gly114
Glu113
Thr116
Glu118
Asp115
Leu5
Arg117
Pro87
Arg111
PAGFP-MyoD
B
Phe129
Val147
Leu132
Leu150
Ala128
Pro223
Asn224
Val125
(-30)GFP-MyoD
C
Asp129
Glu46
Arg111
Arg110
(-30)GFP-MyoD

Fig. 3.9 VMD VDW representation of residues involved in intermolecular contacts between the fluorescent protein and MyoD after MD simulation of the 3rd configurations. The inset represents the entire model highlighting the region detailed. PAGFP interacted with MyoD domain at the basic region (A). (-30)GFP interacted with MyoD domain at both the dimerization region (B) and the basic region (C). PAGFP is represented in iceblue, (-30)GFP in green and MyoD domain in yellow. All background residues are represented in CPK representation.

The RMSD values confirmed what previously observed. In fact, PAGFP-MyoD resulted an unstable model with increasing RMSD in the last ps of trajectories. (-30)GFP-MyoD showed an initial instability that tended to stabilize during the simulation (Fig. 3.10).

The structural analysis of the models of the 3rd configuration enforced the considerations previously made on charge-based attractive influence of the (-30)GFP toward MyoD basic region. Also in this configuration MyoD BHLH domain seems to move in a stochastic way respect to PAGFP. On the contrary, (-30)GFP-MyoD interactions suggest an influence in guiding the positioning and dynamics of MyoD domain.

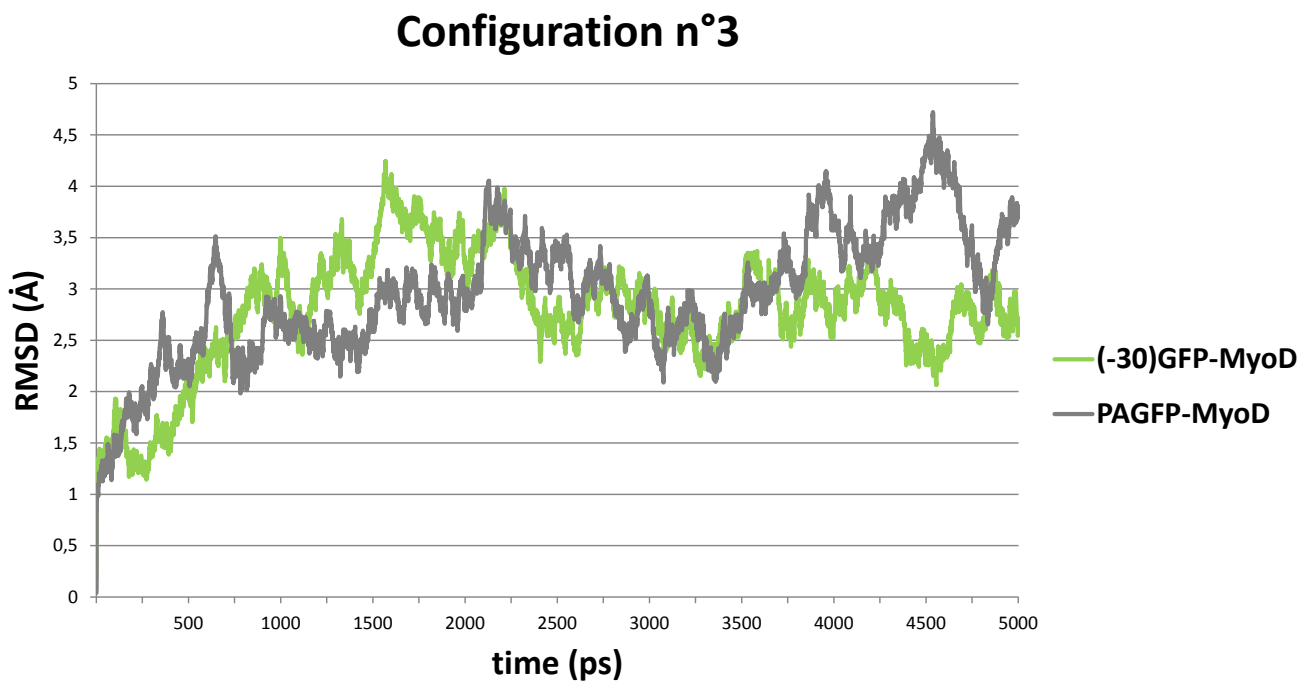

Fig. 3.10 Comparative RMSD graph of the 3rd configurations trajectories. Green curve refers to (-30)GFP-MyoD while grey curve represents PAGFP-MyoD.

4th configuration

The last configuration of PAGFP-MyoD and (-30)GFP-MyoD enforced the previous observations. As shown in Fig. 3.11B, the MyoD domain in presence of PAGFP moved again in an apparently stochastic way maintaining a weak contact with the basic region of MyoD. Analyzing the residues of the interaction, it is evident that it is not a charge-mediated interaction (Fig. 3.12A).

(-30)GFP-MyoD remained in close proximity respect to the FP maintaining the helix 1 faced to the (-30)GFP as it happened in configuration 1 and 3. It was confirmed by the interaction between the FP and the MyoD basic region that involved more residues than in the case of PAGFP-MyoD and above all comprised charged-based interactions (contact between Asp85 and two arginine residues of MyoD: Arg120 and 117) (Fig. 3.12B).

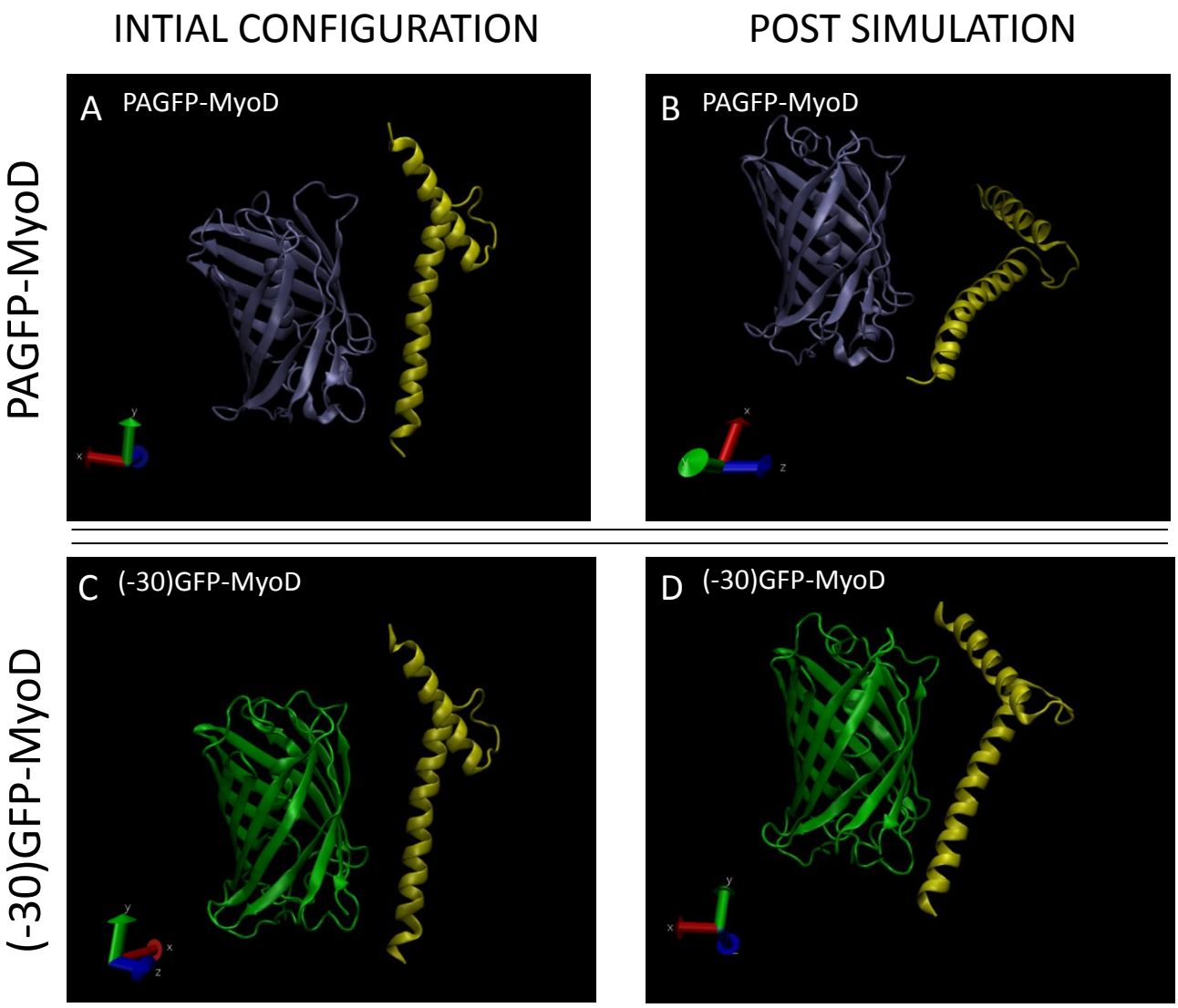

Fig. 3.11 VMD cartoon representation of pre-(A and C) and post-(B and D) simulation of the 4th configurations. PAGFP is represented in iceblue, (-30)GFP in green and the monomeric BHLH domain in yellow.

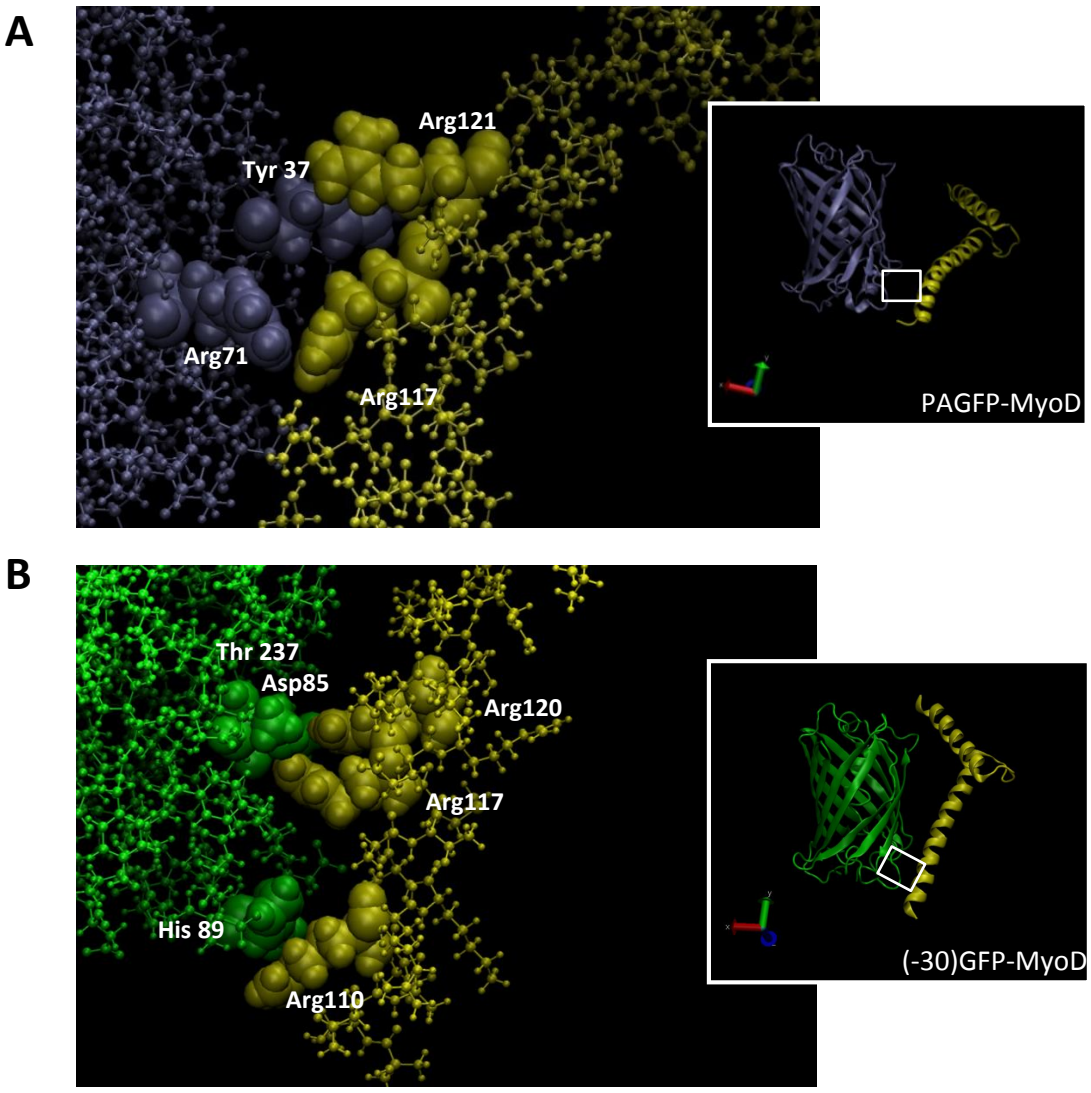

Fig. 3.12 VMD VDW representation of residues involved in intermolecular contacts between the fluorescent protein and MyoD after MD simulation of the 4th configurations. The inset represents the entire model highlighting the region detailed. Both PAGFP and (-30)GFP interacted with MyoD domain at the basic region (A and B). PAGFP is represented in iceblue, (-30)GFP in green and MyoD domain in yellow. All background residues are represented in CPK representation.

Structural stability analysis by RMSD evaluation highlighted a increasing instability of the model PAGFP-MyoD confirmed by the free movement of MyoD domain and a tendency to reach a stable complex in the case of (-30)GFP-MyoD (Fig. 3.13).

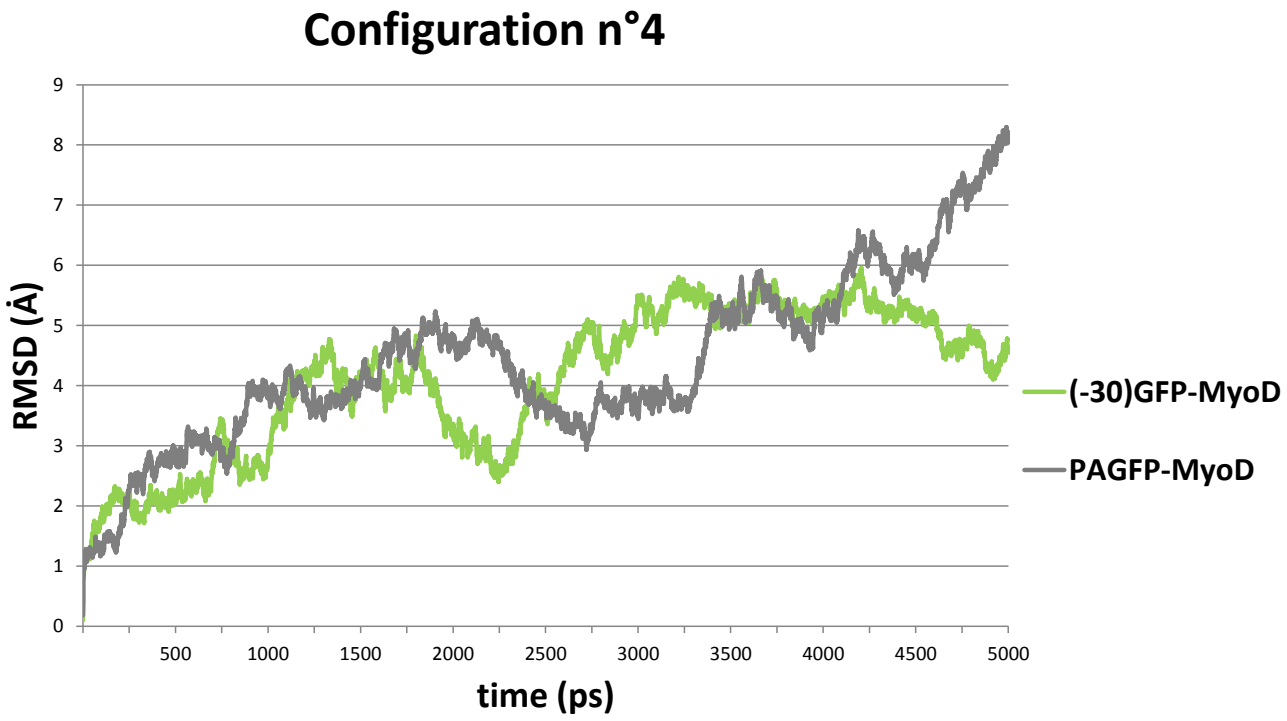

Fig. 3.13 Comparative RMSD graph of the 4th configurations trajectories. Green curve refers to (-30)GFP-MyoD while grey curve represents PAGFP-MyoD.

Structural analyses of the two models simulated starting from the 4th configuration, enforced the hypothesis by which (-30)GFP could apply a charge-based attractive force on MyoD BHLH domain and thus, potentially interfere with dimerization or DNA binding.

Structural analyses of the 4 configurations can be resumed in table 3.1. As previously shown, differently from PAGFP, (-30)GFP interacted with every key region of MyoD BHLH domain. Interactions between (-30)GFP and MyoD were mostly charge-driven contacts. The RMSD values of the last 500 ps simulation support a stronger interaction and higher stability in the case of (-30)GFP-MyoD, except in the 2nd configuration in which both models were unstable and did not show strong interactions.

		INTERACTIONS				RMSD
CONFIG.	MODEL	Loop	Dimerization domain (Helix 2)	DNA binding domain (Helix 1)	Charge-driven	(last 500ps)
1st	PAGFP-MyoD	X			X	8.08 ±1.88
	(-30)GFP-MyoD	X		X	X	2.77 ± 0.42
2nd	PAGFP-MyoD	X				6.28 ± 0.49
	(-30)GFP-MyoD					9.94 ±0.53
3rd	PAGFP-MyoD			X		3.68 ±0.49
	(-30)GFP-MyoD		X	X	X	2.68 ±0.24
4th	PAGFP-MyoD			X		7.10 ±0.67
	(-30)GFP-MyoD			X	X	4.71 ±0.29

Table 3.1 Summary table of structural analyses. For each configuration I indicated (with a X) the MyoD region that interacted with the specific GFP and if the contacts were charge-driven or not. RMSD values are expressed as mean ±SD and are calculated from last 500ps simulation.

Non-bonded interaction energies

To further support the hypothesis of a major interaction of (-30)GFP with MyoD, I evaluated the non-bonded interaction energies between MyoD domain and the specific FP. For each configuration I calculated Van der Waals energy, electrostatic energy and the sum of the two values that constitute the non-bonded interaction energies (Table 3.2).

Non-bonded interaction energies									
		Config. N°1		Config. N°2		Config. N°3		Config. N°4	
		(-30)GFP-MyoD	PAGFP-MyoD	(-30)GFP-MyoD	PAGFP-MyoD	(-30)GFP-MyoD	PAGFP-MyoD	(-30)GFP-MyoD	(-30)GFP-MyoD
First 500ps	Elec energy	-101.24 ±28.43	-70.25 ±6.33	-89.10 ±15.87	-21.18 ±19.15	-187.54 ±26.07	-188.33 ±54.06	-499.05 ±40.58	23.31 ±26.19
	VDW energy	-15.85 ±4.28	-12.25 ±5.03	-11.71 ±1.28	-8.69 ±2.32	-17.24 ±2.45	-12.15 ±2.50	-9.94 ±2.41	-20.78 ±4.10
	TOTAL energy	**-117.09** ±30.98	**-82.78** ±8.57	**-100.81** ±16.09	**-29.87** ±17.91	**-204.79** ±27.57	**-200.47** ±52.42	**-509.00** ±39.04	**2.52** ±23.37
Last 500ps	Elec energy	-189.11 ±19.25	-78.07 ±23.36	-251.23 ±38.20	-166.11 ±70.27	-278.21 ±31.16	-163.31 ±38.92	-389.16 ±71.12	-61.63 ±18.78
	VDW energy	-19.69 ±1.29	-22.17 ±2.99	-3.15 ±1.12	-8.22 ±1.56	-24.83 ±2.51	-21.25 ±2.95	-17.80 ±2.14	-10.34 ±1.93
	TOTAL energy	**-208.80** ±20.23	**-100.25** ±21.40	**-254.39** ±37.88	**-174.33** ±71.51	**-303.04** ±30.00	**-184.56** ±37.32	**-406.96** ±69.99	**-71.97** ±18.23

Table 3.2 Non-bonded interaction energies. The table shows interaction energies values calculated by NAMDEnergy plugin. The calculation considered the interactions between the fluorescent protein and the MyoD domain. For each system were evaluated Van der Waals energy, electrostatic energy and the total non-bonded energy. Data are expressed in kcal/mol and shown as mean ±SD.

Comparing the total interaction energies calculated as a mean of the interaction energies values obtained during the first 500 ps and the last 500 ps of the MD simulation is evident that in three cases of the four configurations simulated, the interactions energies are negative values in the most of the cases and are significantly lower between MyoD domain and (-30)GFP respect to PAGFP and MyoD (Fig. 3.14 and Suppl. Fig. 3.6). Considering that lower values of energies mean higher molecular attraction, Fig. 3.14 show that in each configuration MyoD interacted with (-30)GFP stronger than with PAGFP. Also in the second configuration that is apparently the worst set-up of the four from the interaction point of view, the attractive interaction between MyoD and (-30)GFP resulted greater than in the case of PAGFP-MyoD. Calculating the composition of the total non-bonded interaction energies and thus, the percentage of electrostatic energy and Van der Waals energy, it is evident that the electrostatic energy contribution is greater in (-30)GFP-MyoD respect to PAGFP-MyoD in all the configurations. These results support the hypothesis that (-30)GFP interacts with MyoD by charge-driven attractive interactions.

To better understand the intermolecular interactions, I analyzed the non-bonded interaction energies separating the MyoD peptide in the three elements characterizing the BHLH domain (Suppl. Fig. 3.2):

- ✓ Helix 1 including the residues from 105 to 136
- ✓ Helix 2 characterized by the residues from 147 to 166
- ✓ Loop including the remaining residues from 137 to 146

I calculated the Van de Waals energy, electrostatic energy and thus, the total non-bonded interaction energies between each element and the specific fluorescent protein. In Fig. 3.15 and Suppl. Fig. 3.7, I analyzed the contribution of each element to the total interaction of MyoD with the (-30)GFP or PAGFP.

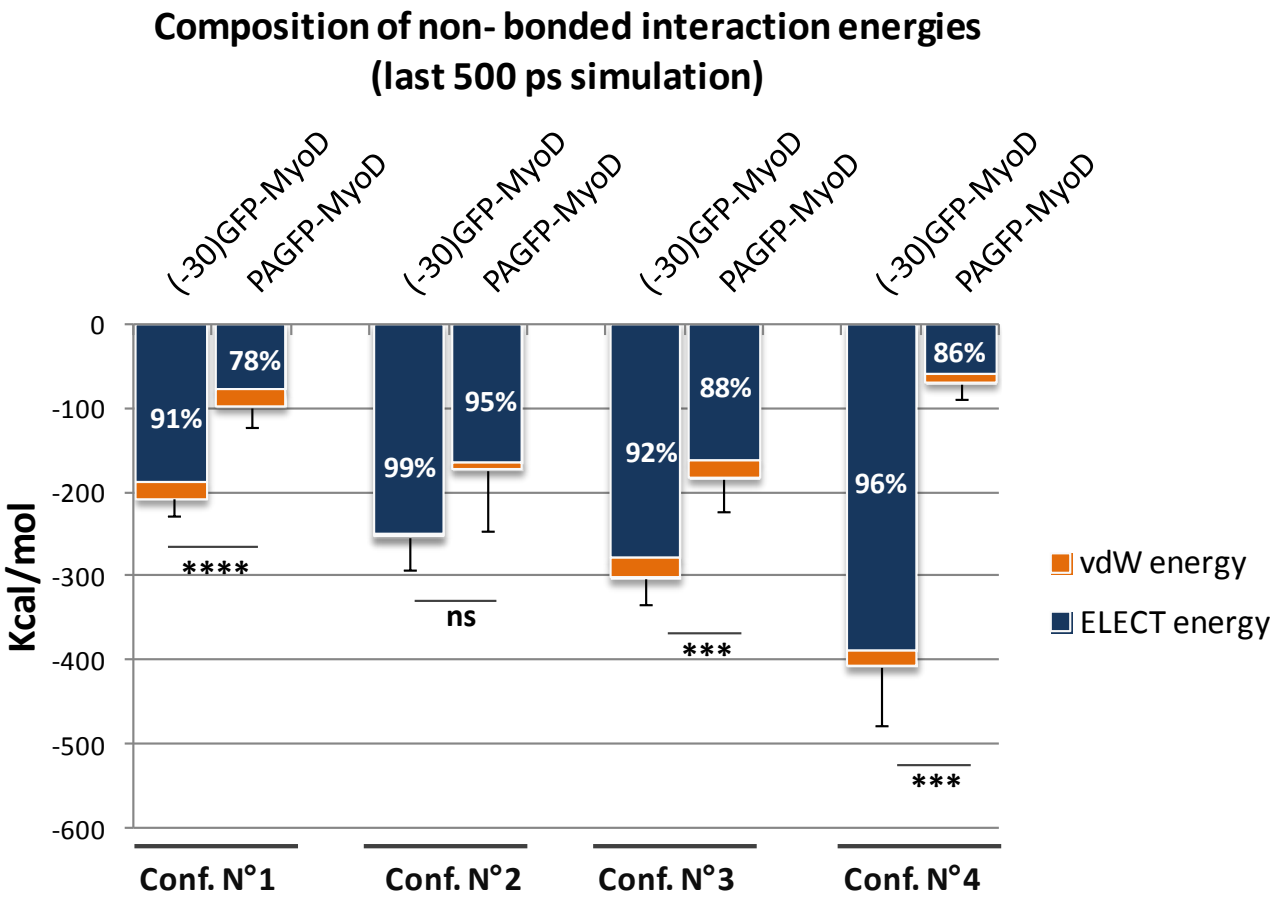

Fig. 3.14 Comparison of interaction energies extracted from the last 500 picoseconds simulation. The percentage expressed on the column represents the percentage of electrostatic energy respect to the total non-bonded energies. Groups among the configurations were analyzed by Student's t-test. Data are shown as mean ±SD.

The Fig. 3.15 clearly shows that the element that most contributed to the interaction energy values is the Helix 1 and thus the DNA binding region.

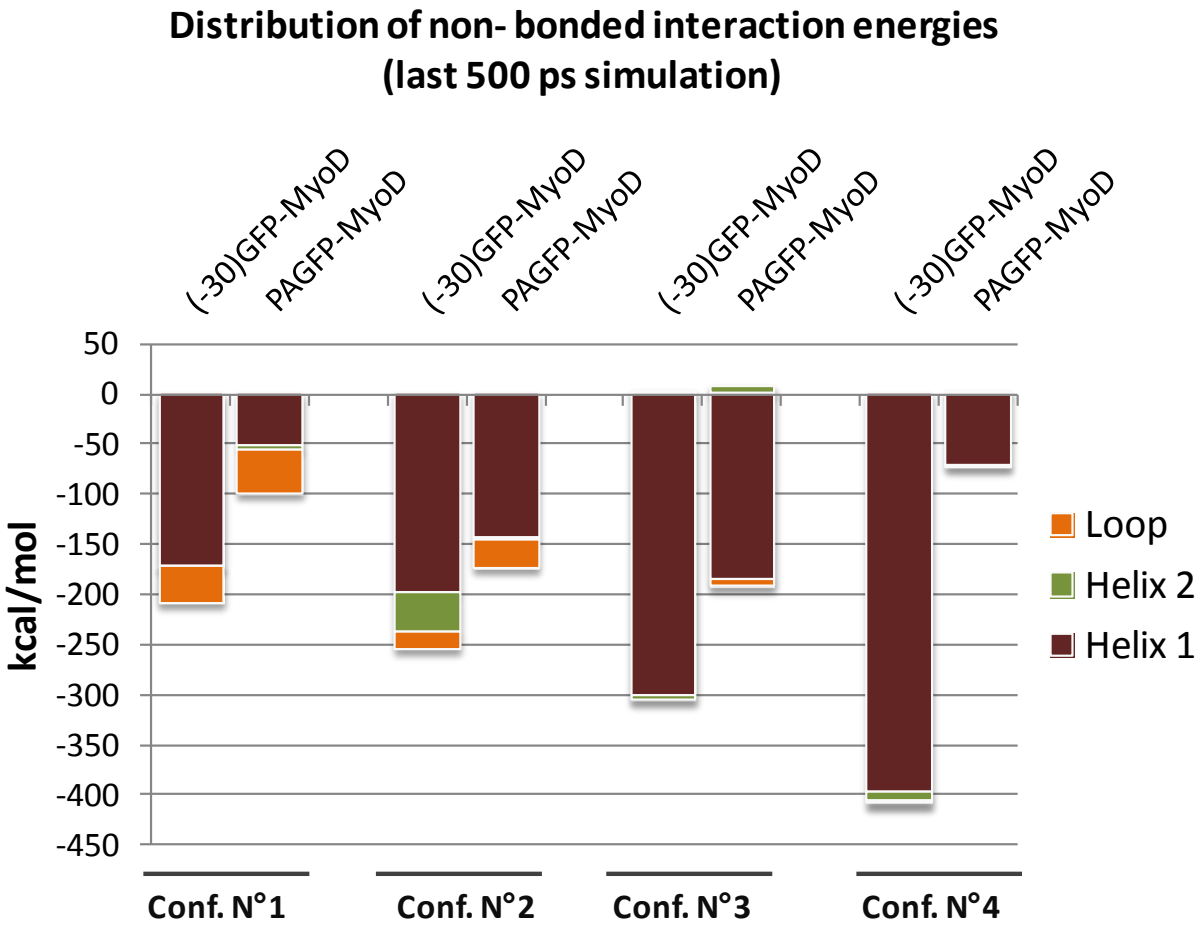

Fig. 3.15 Distribution of the non-bonded interaction energies among the three elements of the MyoD BHLH domain. Helix 1 (DNA binding domain): residues from 105 to 136; Helix 2 (dimerization domain): residues from 147 to 166; Loop: residues from 137 to 146. The energies values were extracted from the last 500 ps simulation. Data are shown as mean and the sum of the energies of the three elements correspond to the total non-bonded interaction energies between the BHLH domain and the specific FP.

Table 3.3 reports the molecules displacement calculated as the difference between the position of the molecules at the initial and final frames of the simulations. The data represent the starting distance between the two molecules ± the variation at the final ps simulation. As previously observed from RMSD data, the interactions between (-30)GFP and MyoD BHLH domain led to a molecular complex stability also in terms of distance parameters. The only exception is represented by the 2nd configuration in which the BHLH domain freely

moved around the (-30)GFP (Fig. 3.5D). On the contrary, PAGFP-MyoD showed a free movement of the three elements of the BHLH domain in each configuration with a predominant tendency to increase the intermolecular distance. In the third configuration, despite the apparent reduction of the distance between PAGFP and the BHLH domain, MyoD rotated around the PAGFP (Fig. 3.8B).

	Conf. N°1		Conf. N°2		Conf. N°3		Conf. N°4	
	(-30)GFP-MyoD	PAGFP-MyoD	(-30)GFP-MyoD	PAGFP-MyoD	(-30)GFP-MyoD	PAGFP-MyoD	(-30)GFP-MyoD	PAGFP-MyoD
Helix 1	29 **-0.30**	29 **+17.07***	31 **+9.50***	31 **-1.92**	31 **-2.74**	31 **-5.45***	26 **-0.81**	26 **+5.16***
Helix 2	45 **+0.96**	45 **-2.46***	41 **+2.16***	41 **+8.96**	37 **+1.25**	37 **-4.29***	38 **-8.65**	38 **+5.77***
Loop	30 **-0.32**	30 **+3.43***	33 **+5.22***	33 **+8.26**	41 **+0.60**	41 **-3.66***	40 **-2.18**	40 **+7.62***

Table 3.3 Molecules displacement calculated as the difference between the position of the BHLH domain elements respect to the FP at the initial and final frames of the simulations. Data represents the starting distance between the two molecules ± the variation at the final ps simulation. Boxes in red show an increasing distance in time. Boxes in green show a decreasing distance in time. * indicates a rotation event of the BHLH domain respect to the GFP. Data are expressed in Å.

Discussion

MyoD is a transcription factor and belongs to the family of muscle-specific Basic Helix Loop Helix (BHLH) proteins that can act as “master switch” for skeletal muscle differentiation [10]. The BHLH domain characterizing the protein is the core of the factor and it shows the main properties of the protein. First contains the two nuclear localization signals that guide the protein through the nuclear envelope to the nucleus where MyoD is active [11]. Second, it is characterized by an amino acidic sequence that allows the homo- or hetero-

dimerization (HLH domain), fundamental for DNA binding [6]. Third, the basic region is responsible of DNA consensus binding and triggering of the “master switch” [12].
(-30)GFP is a standard green fluorescent protein with an abnormal surface negative charge given by the substitution of 15 residues exposed on the surface. This genetic modification switched the theoretical surface electrostatic potential from -7 to -30 [9,13].
With the aim to create an engineered fluorescent version of MyoD able to pass the plasmatic membrane, I previously fused the (-30)GFP and MyoD. The recombinant protein showed great results in terms of protein delivery and nucleocytoplasmic shuttling but revealed unexpected inhibitory effects of (-30)GFP on MyoD activity (Fig. 2.1.6, 2.1.9). Analyzing the biochemical properties of the two proteins we formulated different hypotheses about the possible causes for this inhibitory mechanism. All the theories were based on the effect of the peculiar negative charges of the (-30)GFP on the MyoD structure or the DNA binding mechanism.
The present work is a computational study with the purpose to validate the hypothesis that (-30)GFP negatively influenced MyoD by its peculiar high surface negative charge.
To set and evaluate the MD simulations, I examined the state-of-the-art about the protein-protein interaction studies. Mainly, MD simulations were analyzed by a qualitative study about trajectories and conformational changes, assessment of model stability given by the calculation of RMSD and a quantitative evaluation of the interaction energies between molecules [1-2,14-16].
MyoD is a protein with a very mobile structure, excepting for the BHLH domain. In fact, only the 3D structure of this domain has been crystallized and deposited in RCSB-PDB. The protein structure prediction analyses performed on MyoD revealed a predominantly

disordered structure that ideally shuld not fold into any secondary structure except for the BHLH domain. Considering these structure predictions, I assumed that the disordered part of MyoD does not influence the BHLH domain movement and ability to interact with other proteins. Hypothesizing different possibilities of interfacing of the BHLH domain with the (-30)GFP I generated four configurations of the model. In parallel, as control, I generated the same models for MyoD with the PAGFP that is a photoactivatable variant of the GFP that experimentally maintained the activity of MyoD.

Overall, structural analyses of MD simulations suggested charge–guided interactions between (-30)GFP and MyoD BHLH domain while revealed an apparent stochastic movement of the domain toward the PAGFP. As supposed in our hypothesis most of interactions observed between MyoD and (-30)GFP involved the negative surface charges of the GFP. In 3 out of 4 configurations, the supernegative GFP interacted with the basic region of the BHLH domain suggesting a strong charge-driven attraction and a consequent interference with the DNA binding process. This interaction-based hypothesis was enforced by non-bonded interaction energies data that showed greater interaction in (-30)GFP-MyoD than in PAGFP-MyoD models. The higher percentage of electrostatic energy in the complex of (-30)GFP-MyoD confirmed a stronger charge-driven attraction between MyoD and (-30)GFP respect to PAGFP and MyoD. The interaction energies analyses performed separating the elements of the BHLH domain showed that the DNA-binding region, enriched of positive-charges, is the main element that contributes to the interaction with the fluorescent protein. Combining the first qualitative observations with the quantitative data of non-bonded interaction energies, the DNA-binding domain resulted the region that could be improperly stabilized by the (-30)GFP altering the BHLH domain functionality.

Since the MD simulations ran for 5 nanoseconds, results could be considered preliminary observations. Currently we are running longer simulations to enforce our preliminary data and to deepen other structural aspects such as the solvent accessibility area (SAS) that some authors calculated to evaluate variations in the protein-protein interface [1, 15].

Next steps could consider more complex MD simulations for the analysis of the influence of (-30)GFP in the dimerization process and then in the dimer-DNA complex formation. Starting from the current molecular systems (~45000 atoms) we could generate larger systems (until ~90000 atoms) adding a second (-30)GFP-MyoD BHLH domain to stimulate dimerization and, once the dimerization occurred, the DNA consensus sequence in order to evaluate the DNA binding process.

In conclusion, the present molecular dynamics study provided preliminary suggestions for the inhibitory effect observed in experimental validation. The abnormal interaction between (-30)GFP and MyoD BHLH domain could alter the formation of the dimer or the binding to the DNA and thus, the transcriptional activity.

Methods

Molecular Models. The 3D models of (-30)GFP and PAGFP were both obtained by homology modeling. For this purpose I first aligned amino acidic sequences with the photoactivatable GFP (3GJ2) deposited in RCSB Protein Data Bank (PDB) (PDB: http://www.rcsb.org/) [5]. The alignment was performed using NCBI-BLASTp tool, which is available on the NCBI website (https://www.ncbi.nlm.nih.gov/). For homology modeling I used SWISS-MODEL that is a protein structure homology modeling server,

accessible via the ExPASy webserver (SWISS-MODEL: https://www.swissmodel.expasy.org/). I inserted the sequences codifying for (-30)GFP and PAGFP and I asked the server to build two models using the structure of photoactivatable GFP (3GJ2) as template. 3D models obtained for (-30)GFP and PAGFP were evaluated by surface electrostatic potential analyses using APBS plugin of VMD software.
The atomic structure of MyoD BHLH domain was taken from RCSB PDB. The structure deposited in PDB (1MDY) is a homo-dimer bound to the DNA consensus sequence (see Suppl. Fig. 3.2A, B). I extracted the chain in yellow in Suppl. Fig. 3.2B corresponding to the BHLH binding domain of a MyoD monomer and I used this monomer for setting the GFP-MyoD molecular complexes [6].
Protein structure prediction was taken using PSI-blast based secondary structure PREDiction (PSIPRED v3.3) and DISOrder PREDiction (DISOPRED3) servers (http://bioinf.cs.ucl.ac.uk/psipred/) [17]. PSIPRED is a secondary structure prediction metho. DISOPRED is a predicting method for disordered regions in proteins and the confidence score of 0,5 represents the threshold above which the residues are defined as disordered.

MD configurations set-up. I set different configurations to reproduce the fusion of MyoD to the FP. I positioned the BHLH domain in 4 different positions respect to the FP. In order to generate the 4 configurations, as first, I considered the center of mass of the FP as the origin of the axes (x_{FP}, y_{FP}, z_{FP}=0,0,0). Then, respect to the specific FP, I moved the MyoD domain obtaining the following configurations:

- Configuration n°1: (x_m, y_m, $z_{m=}$ +3, +10, -30)
- Configuration n°2: (x_m, y_m, $z_{m=}$ +28, +15, 5)
- Configuration n°3: (x_m, y_m, $z_{m=}$ 0, +15, +28)

- Configuration n°4: (x_m, y_m, $z_{m=}$ -27, +10, +5)

where x_m, y_m, z_m are coordinates of MyoD domain (see Suppl. Fig. 3.5).

MD simulation parameters. MD simulations were carried out with NAMD software together with the Visual Molecular Dynamics program (VMD) software [7-8]. The Force Field used was CHARMM 36 and all of the MD simulations were performed in explicit TIP3 water molecules, applying periodic boundary conditions.
All the systems were first subjected to an energy minimization phase of 1000 steps (20 ps). (-30)GFP and PAGFP were then equilibrated for 1ns at 310 K. The obtained equilibrated structures of GFPs were used for MD configurations set-up. In order to relax the volume of the periodic boundary box, the MD simulations were carried out under constant pressure and temperature (NPT) conditions. The pressure was set to 1 atm, the temperature at 310 K, the time step was 2 fs and the non-bonded cut-off was 12 Å. In order to control the temperature, Langevin dynamics were employed, maintaining the pressure at 1 atm, a period of 100 ns and a decay of 50 fs. Trajectories were recorded every 500 fs for 2500000 steps with 5 ns.

RMSD calculation. The stability of the system was evaluated by calculating the root mean square deviation (RMSD) of the model (3.8).

$$RMSD = \sqrt{\frac{1}{n}\sum_{i=1}^{n}(x_i - x_{i0})^2 + (y - y_{i0})^2 + (z_i - z_{i0})^2} \qquad (3.8)$$

where n represent the number of atoms and x_i, y_i, z_i and x_{i0}, y_{i0}, z_{i0} describe the coordinates of the atom i at a certain instance and its reference state, respectively.

Non-bonded interaction energies. Non-bonded interaction energies were calculated by NAMDEnergy plugin. First I evaluated Van der Waals energy, electrostatic Coulomb energy and the total non-bonded interaction energy between MyoD BHLH domain and the specific FP. Then, I examined the non-bonded interaction energies of each fluorescent protein with the BHLH domain separated in three elements:

- Helix1: residues from 105 to 136
- Loop: residues from 137 to 146
- Helix2: residues from 147 to 147

The energies values were expressed in kcal/mol.

Distances analysis. I calculated the distances between the center of mass of the fluorescent protein and the center of mass of Helix 1, Helix 2 or Loop among the trajectories. Data are reported in Å.

Statistical analyses. The non-bonded interaction energies data were analyzed by Student's t-test for a direct comparison of two groups. Associations with $p < 0.05$ were considered significant. Statistical tests were done using GraphPad Prism 7.0 software. **** P <0.0001.

References

1. Aprodu I, Soncini M, Redaelli A. Interaction forces and interface properties of KIF1A kinesin-alphabeta tubulin complex assessed by molecular dynamics. J Biomech. 2008 Nov 14;41(15):3196-201

2. Latha MS, Saddala MS. Molecular docking based screening of a simulated HIF-1 protein model for potential inhibitors. Bioinformation. 2017 Nov 30;13(11):388-393
3. Etheve L, Martin J, Lavery R. Protein-DNA interfaces: a molecular dynamics analysis of time-dependent recognition processes for three transcription factors. Nucleic Acids Res. 2016 Nov 16;44(20):9990-10002.
4. Kosztin D, Bishop TC, Schulten K. Binding of the estrogen receptor to DNA. The role of waters. Biophys J. 1997 Aug;73(2):557-70.
5. Henderson JN, Gepshtein R, Heenan JR, Kallio K, Huppert D, Remington SJ. Structure and mechanism of the photoactivatable green fluorescent protein. J Am Chem Soc. 2009 Apr 1;131(12):4176-7.
6. Ma PC, Rould MA, Weintraub H, Pabo CO. Crystal structure of MyoD bHLH domain-DNA complex: perspectives on DNA recognition and implications for transcriptional activation. Cell. 1994 May 6;77(3):451-9.
7. Phillips JC, Braun R, Wang W, Gumbart J, Tajkhorshid E, Villa E, Chipot C, Skeel RD, Kalé L, Schulten K. Scalable molecular dynamics with NAMD. J Comput Chem. 2005 Dec;26(16):1781-802
8. Humphrey W, Dalke A, Schulten K. VMD: visual molecular dynamics. J Mol Graph. 1996 Feb;14(1):33-8, 27-8.
9. Zuris JA, Thompson DB, Shu Y, Guilinger JP, Bessen JL, Hu JH, Maeder ML, Joung JK, Chen ZY, Liu DR. Cationic lipid-mediated delivery of proteins enables efficient protein-based genome editing in vitro and in vivo. Nat Biotechnol. 2015 Jan;33(1):73-80
10. Tapscott SJ. The circuitry of a master switch: Myod and the regulation of skeletal muscle gene transcription. Development. 2005 Jun;132(12):2685-95.

11. Vandromme M, Cavadore JC, Bonnieu A, Froeschlé A, Lamb N, Fernandez A. Two nuclear localization signals present in the basic-helix 1 domains of MyoD promote its active nuclear translocation and can function independently. Proc Natl Acad Sci U S A. 1995 May 9;92(10):4646-50.
12. Weintraub H, Dwarki VJ, Verma I, Davis R, Hollenberg S, Snider L, Lassar A, Tapscott SJ. Muscle-specific transcriptional activation by MyoD. Genes Dev. 1991 Aug;5(8):1377-86.
13. Lawrence MS, Phillips KJ, Liu DR. Supercharging proteins can impart unusual resilience. J Am Chem Soc. 2007 Aug 22;129(33):10110-2.
14. Wang Q, Gao J, Liu Y, Liu C. Molecular dynamics simulation of the interaction between protein tyrosine phosphatase 1B and aryl diketoacid derivatives. J Mol Graph Model. 2012 Sep;38:186-93.
15. Sahihi M, Ghayeb Y. An investigation of molecular dynamics simulation and molecular docking: interaction of citrus flavonoids and bovine β-lactoglobulin in focus. Comput Biol Med. 2014 Aug;51:44-50.
16. Selvaraj C, Bharathi Priya R, Singh SK. Communication of γ phage lysin plyG enzymes binding toward SrtA for inhibition of Bacillus anthracis: protein-protein interaction and molecular dynamics study. Cell Commun Adhes. 2014 Oct;21(5):257-65.
17. Bryson K, McGuffin LJ, Marsden RL, Ward JJ, Sodhi JS, Jones DT. Protein structure prediction servers at University College London. Nucleic Acids Res. 2005 Jul 1;33(Web Server issue):W36-8.

Supplementary Figures

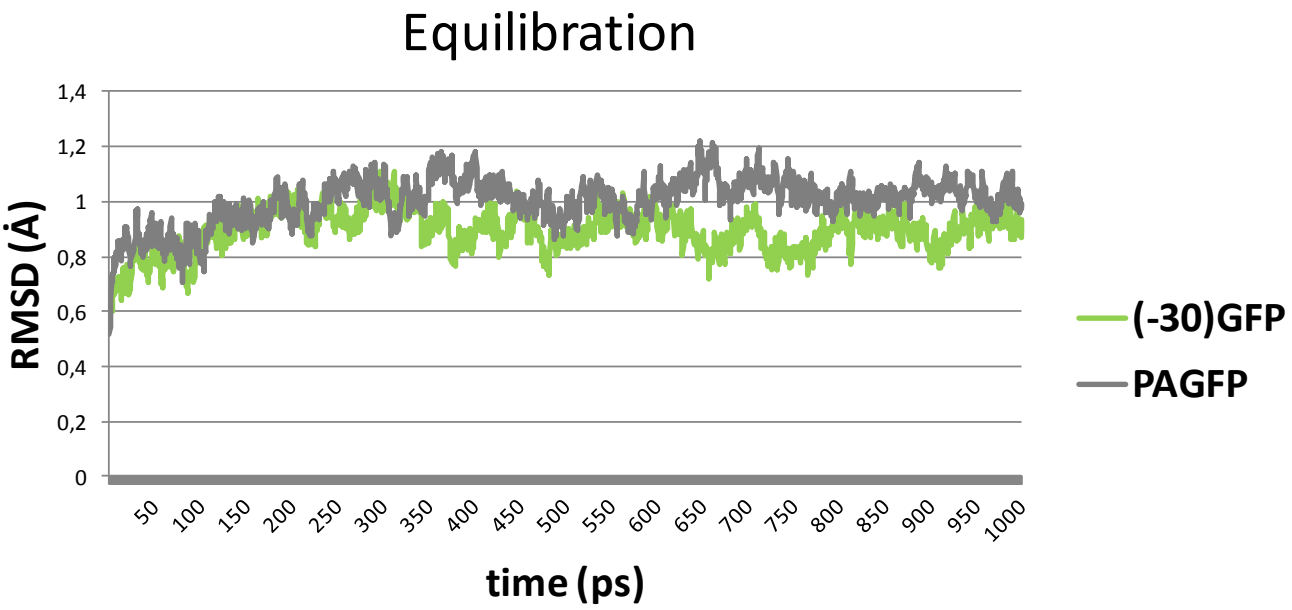

Suppl. Fig. 3.1 RMSD calculation of (-30)GFP and PAGFP after 1ns of equilibration at 310K.

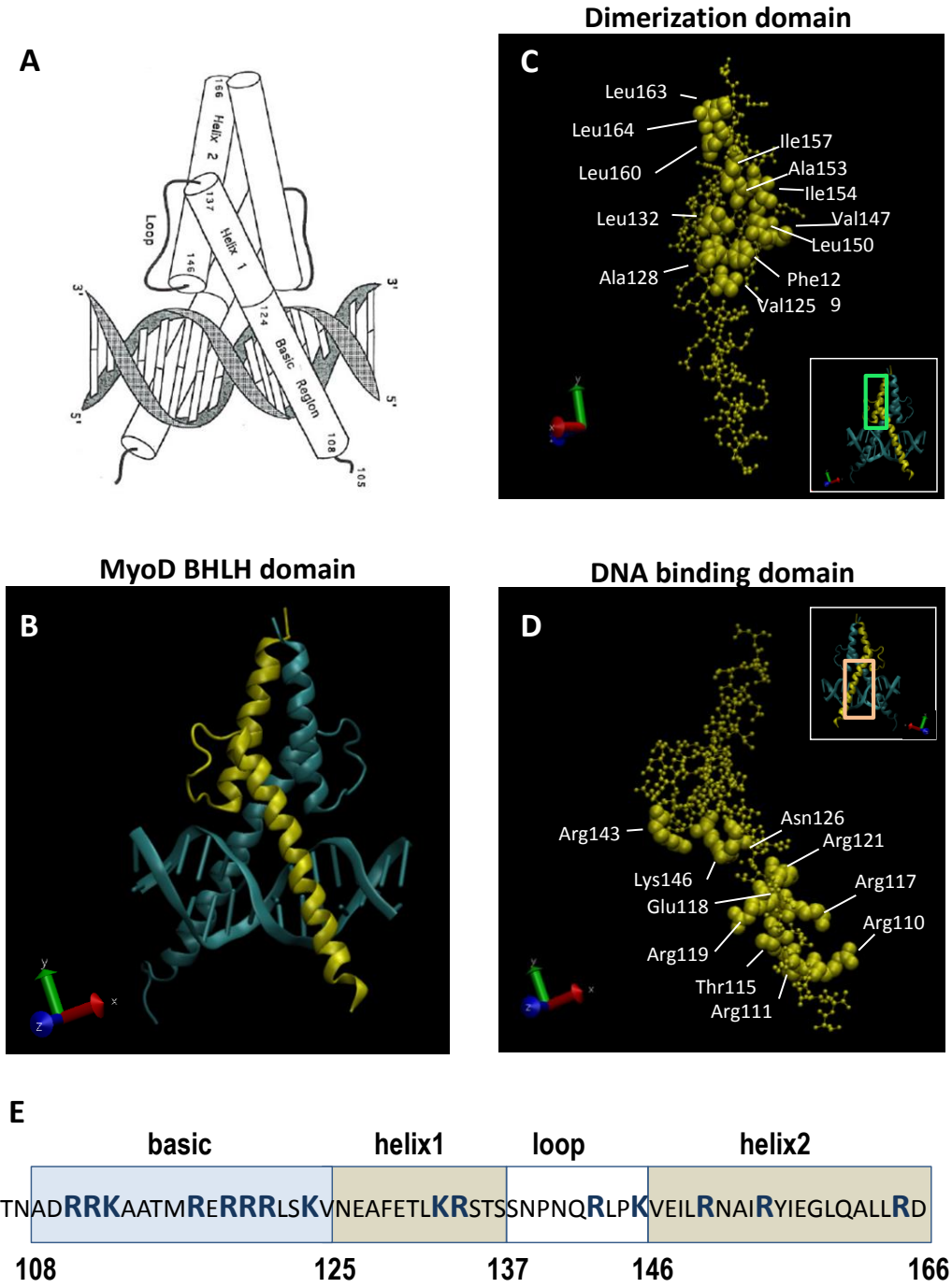

Suppl. Fig. 3.2 MyoD BHLH domain. (A) Graphical representation of the homo-dimer MyoD bound to the DNA consensus sequence. The alpha helices are represented as cylinders. Image was adapted from Ref. [6]; (B) VMD cartoon representation of MyoD-DNA complex. Helices highlighted in yellow show the BHLH domain characterizing the single monomeric BHLH domain extracted for MyoD model generation; (C) VMD representation of the monomeric BHLH domain. All residues are showed in CPK representation while residues involved in dimerization are highlighted with VDW representation; (D) VMD representation of

the monomeric BHLH domain. All residues are showed in CPK representation while residues involved in DNA consensus sequence binding are highlighted with VDW representation; (E) graphical representation of the amino acidic sequence of the monomeric BHLH domain. Residues positively charged (Arginine and Lysine) are highlighted in blue.

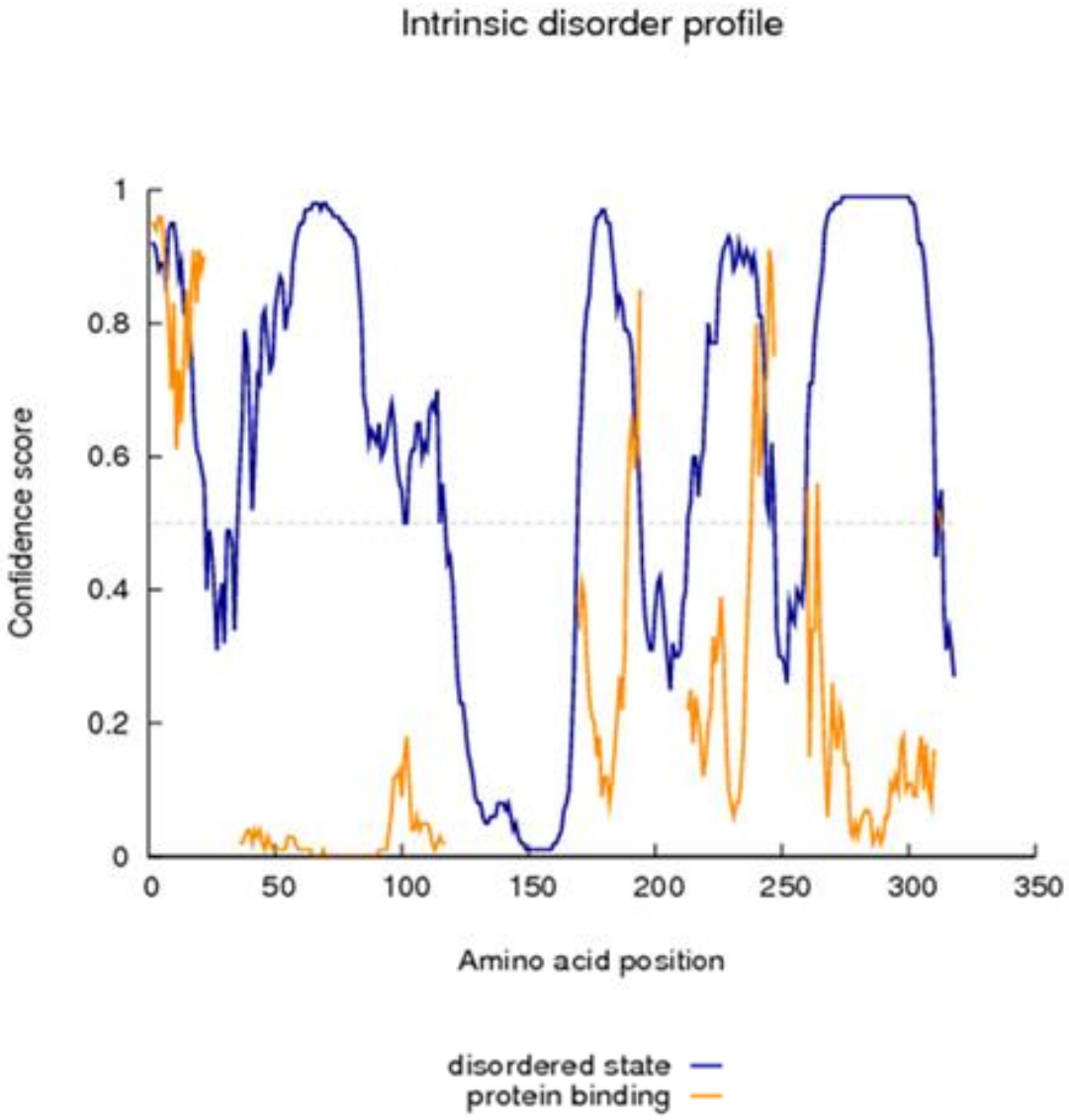

Suppl. Fig. 3.3 Disorder prediction of MyoD using the Disorder Prediction server (DISOPRED3). The confidence score of 0,5 represents the threshold above which the residues are defined as disordered.

Suppl. Fig. 3.4 Secondary structure prediction of MyoD using PSI-blast based secondary structure PREDiction (PSIPRED).

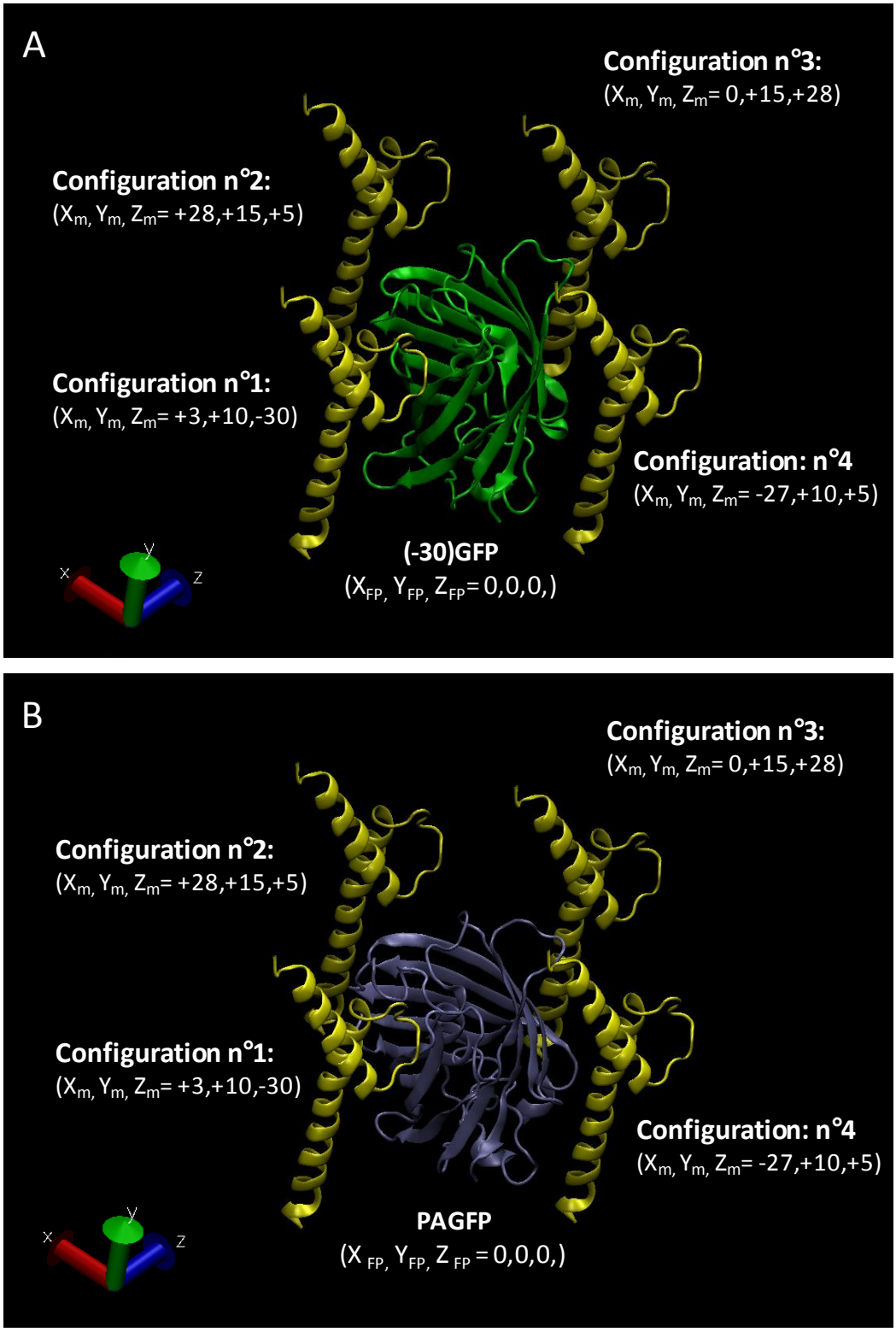

Suppl. Fig. 3.5 VMD representation of MD configurations for (A) (-30)GFP and (B) PAGFP. Considering the center of mass of the fluorescent proteins as the origin (X_{FP}, Y_{FP}, Z_{FP}=0,0,0), the monomeric BHLH domain of MyoD was translated in 4 different positions thus facing in 4 different configurations the fluorescent proteins.

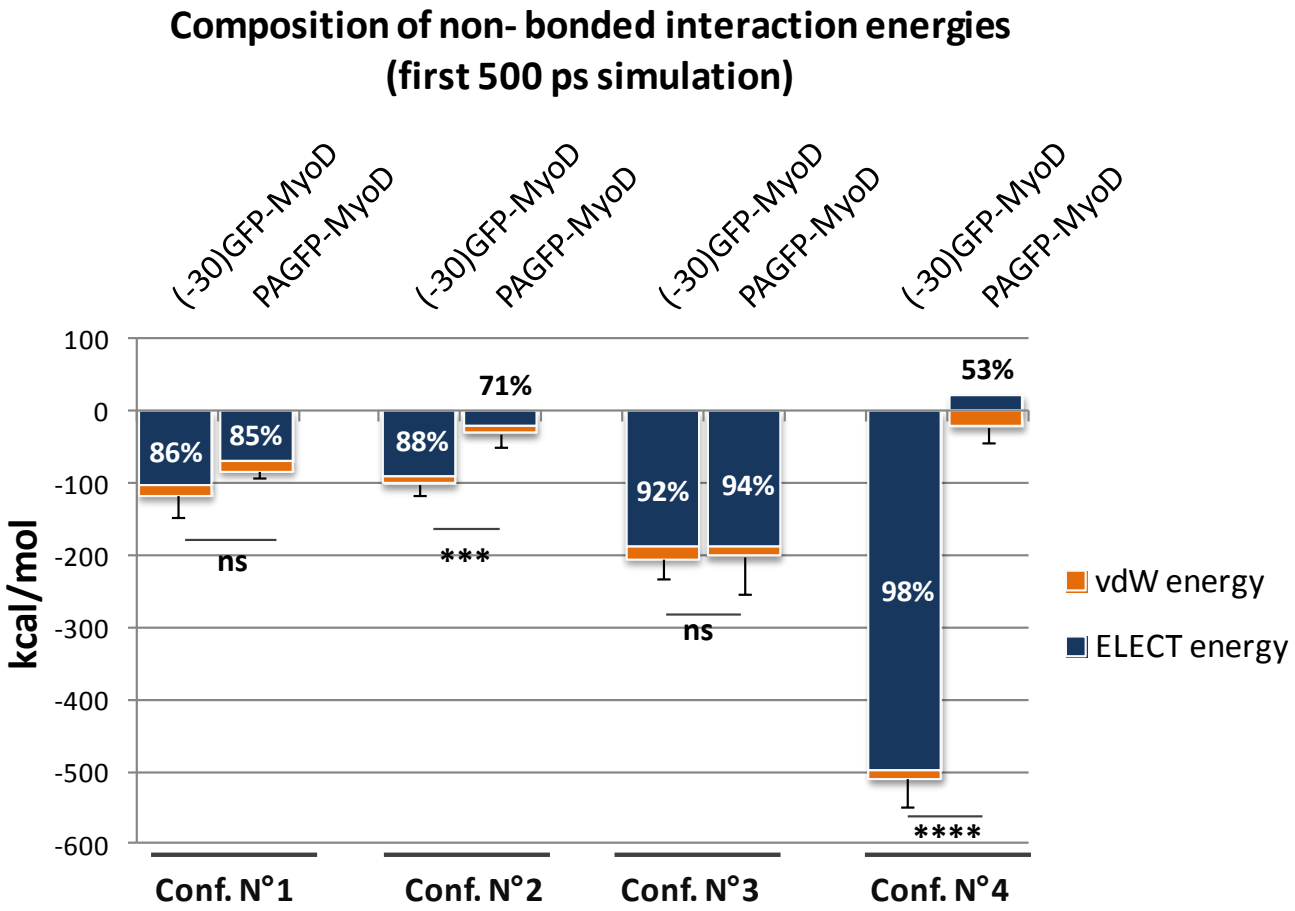

Suppl. Fig. 3.6 Comparison of interaction energies extracted from the first 500 picoseconds simulation. The percentage expressed on the column represents the percentage of electrostatic energy respect to the total non-bonded energies. Groups among the configurations were analyzed by Student's t-test. Data are shown as mean ±SD.

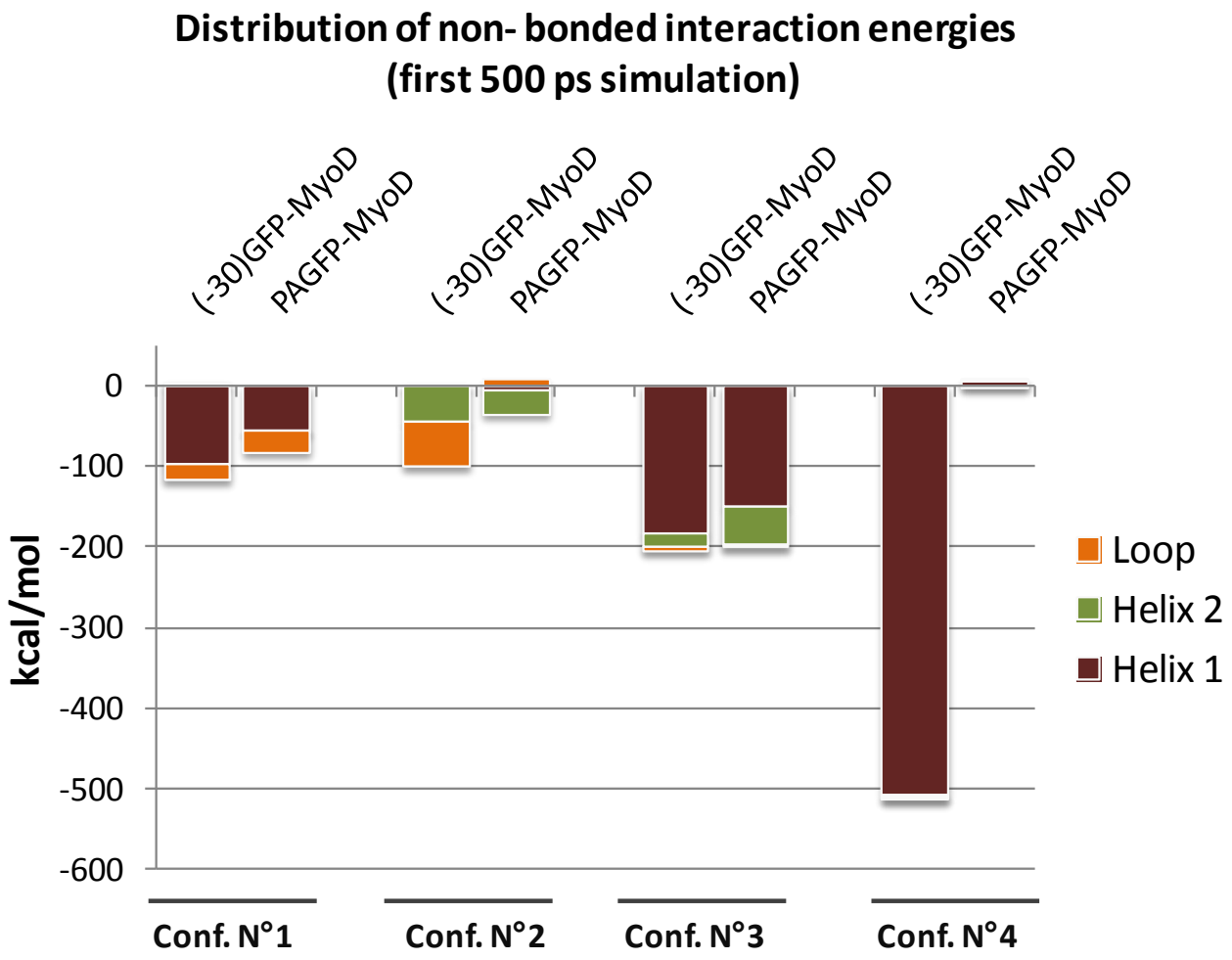

Suppl. Fig. 3.7 Distribution of the non-bonded interaction energies among the three elements of the MyoD BHLH domain. Helix 1: residues from 105 to 136; Helix 2: residues from 147 to 166; Loop: residues from 137 to 146. The energies values were extracted from the last 500 picoseconds simulation. Data are shown as mean and the sum of the energies of the three elements correspond to the total non-bonded interaction energies between the BHLH domain and the specific FP.

CHAPTER 4: General Conclusions and Outlook

The clinical application of MSC-based therapy showed extraordinary advancements in the last years. Despite the huge progress achieved, the knowledge about stem cell fate control still remains a challenge.
In this respect, recent studies highlighted the importance of mechanical inputs of cell environment. They demonstrated that cells are able to propagate a mechanical signal started by physical forces and transduce the input into a biochemical response. This mechanism, known as mechanotransduction, mediates many cellular processes, such as cell migration, proliferation and differentiation. The comprehension of this mechanism could contribute in improving MSC fate control and consequently MSC-based therapy, for instance by allowing huge expansion of undifferentiated MSCs *in vitro*. In this context, little is known about the role of NPC. It is a structural element that has not yet been investigated in the mechanotransduction and the reasons are mainly related to the structural complexity and the difficulty in studying the fluxes of biologic material (proteins, DNA or RNA) through the NPC.

The NICHOID project started with the aim to study the NPC in response to mechanical stimuli. The NICHOID hypothesis is that the nuclear envelope and the NPC are mechano-sensitive elements that respond to mechanical signals re-arranging their structure and altering the nuclear transport. In order to validate this hypothesis, both experimental and computational approaches were considered.
The experimental validation required the molecular engineering of fluorescent transcription factors able to migrate from the cytoplasm to the nucleus through the NPC and the measurement of their

nucleocytoplasmic shuttling under different mechanical stress conditions.
With the aim of engineering the fluorescent molecules necessary for the nuclear import measurement (see Chapter 2), I developed several fluorescent tools with improved and peculiar characteristics in comparison to standard fluorescent probes (e.g. GFP or YGP).

Deepening the available literature of fluorescent probes, I found that to the best of my knowledge, protein transduction technologies have never been used for intracellular shuttling studies. Considering the advantages of these fluorescent tracers featuring a reduced time of intracellular protein delivery and the control of cell loaded fluorescent molecules, I designed and validated two fluorescent variants of the transcription factor MyoD able to be delivered as purified proteins (see Chapter 2.1). Images of failed protein internalization of Tat-GFP-MyoD, suggested that in this system Tat-mediated transduction is unsuitable for nucleocytoplasmic transport studies. On the contrary, (-30)GFP-based variant of MyoD localized into the nucleus within 3 hours and was suitable for protein localization analysis and nucleocytoplasmic shuttling measurement. Unexpectedly, when analyzing the transcription promoting activity of this fluorescent recombinant factor, some limitations arouse concerning the inhibitory effect of (-30)GFP on MyoD functionality.

In chapter 2.2 I described the development of a different approach aimed at obtaining fluorescent tracers for nucleocytoplasmic shuttling measurement. This strategy is based on photosensitive variants of MyoD. Differently from protein transduction technologies, photoactivatable, photoconvertible and photoswitching proteins are tools very often used in nucleocytoplasmic transport assays. They offer

the possibility to selectively photoactivate the fluorescence signal and monitor the movement of the activated proteins. Furthermore, they avoid issues typical of classic fluorescent probes, such as the impossibility to distinguish from newly synthesized molecules and proteins re-entering the ROI. As a matter of novelty, despite numerous advancements in the field of photosensitive proteins, these fluorescent probes have never been studied in association with the myogenic transcription factor MyoD. I developed and analyzed three photosensitive probes fused to MyoD, two photoactivatable and one photoconvertible. The recombinant protein that showed both optimal intracellular localization and transcription promoting activity was the photoactivatable MyoD-PAGFP. In fact, while every photosensitive variant was able to reach the physiological nuclear localization, only PAGFP showed a conserved MyoD functionality.

On the basis of the experimental results, in Chapter 3 I deepened some aspects of the fluorescent tool action. To this purpose, I used molecular dynamics to study the inhibitory effect of (-30)GFP on MyoD activity. I have recreated a molecular model of the fluorescent protein with the (-30)GFP and the Basic Helix Loop Helix (BHLH) domain of MyoD. I compared the (-30)GFP-MyoD model with a control model characterized by PAGFP and MyoD BHLH domain. I analyzed the structural rearrangements and the non-bonded interactions between the fluorescent protein and the MyoD BHLH domain. The computational analyses suggested a charge-driven interaction between MyoD and (-30)GFP that could alter the key mechanisms for MyoD transcription promoting activity: dimerization and DNA binding.

In conclusion, both my experimental and computational analyses performed highlighted the importance of the design and the validation

of fluorescent tools for intracellular shuttling study. Each tool requires specific analyses that depend from the type of factor fused to the fluorescent probe. In our case, the protein of interest was a transcription factor promoting MSC differentiation. Thus, experimental and computational analyses should mainly evaluate the ability to migrate into the nucleus and the transcription promoting activity. Keeping native properties of the protein of interest would ensure the dynamics of intracellular shuttling and minimize the possible alterations given by the presence of the fluorescent probe. In the NICHOID project context background, this Ph.D. thesis provided a suitable photoactivatable fluorescent tool for the study of the influence of mechanical stimuli on nuclear import. MyoD-PAGFP respected all the aspects required in the starting design, as it resulted suitable for both biological and mechano-physical investigations. Furthermore, as photoactivatable factor, nucleocytoplasmic transport could be measured through several techniques based on fluorescence confocal microscopy or super-resolution imaging.

The next step will be the measurement of the nuclear import of MyoD-PAGFP in MSCs cultured under different mechanical stress conditions, as well as comparing the experimental measurements with a multiscale computational model of transcription factor flow, in order to verify the hypothesis of the NICHIOID project about the role of NPC in mechano-response.
Preliminary FRAP measurements based on (-30)GFP-MyoD in MSCs cultured in different morphological configurations revealed encouraging results (see Chapter 2.1). In fact in line with the NICHOID hypothesis, the nuclear import rate resulted lower in MSCs cultured in isotropic adhesion conditions (3D nichoid cell culture) respect to 2D cell culture (stretched condition). Fluorescence recovery curves revealed that

nuclear import in roundish nuclei was slower than in spread nuclei, suggesting a mechano-dependent mechanism. Despite (-30)GFP-MyoD was transcriptionally silent, FRAP measurements provided important preliminary data for further analyses with MyoD-PAGFP, the fluorescent tool validated for both nuclear localization and transcription promoting activity.

CHAPTER 5: List of Publications and Conference Proceedings

PUBLICATIONS

ARTICLES

1. Paracchini L, Beltrame L, Boeri L, Fusco F, Caffarra P, Marchini S, Albani D, Forloni G. Exome sequencing in an Italian family with Alzheimer's disease points to a role for seizure-related gene 6 (SEZ6) rare variant R615H. Alzheimers Res Ther. 2018 Oct 12;10(1):106. (IF: 5.015)
2. Albani D, Marizzoni M, Ferrari C, Fusco F, Boeri L, et al Plasma Aβ42 as biomarker of prodromal AD progression in patients with amnestic mild cognitive impairment: evidence from the PharmaCog/E-ADNI study. Journal of Alzheimer's Disease. 2018 Aug DOI: 10.3233/JAD-180321 (IF: 3.731)
3. Chierchia A, Chirico N, Boeri L, Raimondi I, Riva GA, Raimondi MT, Tunesi M,Giordano C, Forloni G, Albani D. Secretome released from hydrogel-embedded adipose mesenchymal stem cells protects against the Parkinson's disease related toxin 6-hydroxydopamine. Eur J Pharm Biopharm. 2017 Dec;121:113-120. (IF: 4.159)

ABSTRACTS

4. Boeri L, Jacchetti E, Negro A, Albani D, Raimondi MT. Fluorescence live detection of protein nuclear import in mesenchymal stem cells adhering to the “nichoid” nanoengineered culture substrate. European Cells and Materials Vol. 33 Suppl. 2, 2017 (0062). ISSN 1473-2262
5. Boeri L, Chierchia A, Chirico N, Raimondi MT, Giordano C, Forloni G, Albani D. Secretome released from adipose mesenchymal

stem cells protects SH-SY5Y cells from oxidative stress and increases sirtuin 3 expression. Clinical Neuropathology, Vol. 36 No. 3/2017: 123. ISSN 0722-5091

6. Boeri L, Tunesi M, Giordano C, Albani D, and Raimondi MT. Engineered in vitro model to assess the neuroprotective effect of mesenchymal stem cell secretome on SH-SY5Y neuroblastoma cells exposed to 6-hydroxydopamine. European Cells and Materials Vol. 31. Suppl. 1, 2016 (page 50) ISSN 1473-2262.

CONFERENCE PRESENTATIONS

1. Boeri L, Jacchetti E, Negro A, Albani D, Raimondi MT. Live Detection of a Fluorescent Myogenic Factor to estimate its Nuclear Import Flow in Mesenchymal Stem Cells growing in the 3D “nichoid” culture substrate. Poster presentation at Termis World Congress 2018, Kyoto, Japan, 4th -7th September 2018.

2. Boeri L, Tunesi M, Fusco F, Giordano C, Albani D, and Raimondi MT. Molecular insights into the neuroprotective effect of mesenchymal stem cell secretome on an in vitro Parkinson’s disease model by using a 3D cell culture system. Poster presentation at FENS 2018, Berlin, Germany, 7th -11th July 2018.

3. Boeri L, Jacchetti E, Negro A, Albani D, Raimondi MT. An engineered supernegative GFP to track the nuclear import of transcription factors in mesenchymal stem cells. Poster presentation at GNB 2018, Milan, Italy, 25th -27th June 2018.

4. Boeri L, Jacchetti E, Negro A, Albani D, Raimondi MT. Fluorescent variants of a myogenic factor to estimate its nuclear import flow in mesenchymal stem cells. Poster presentation at Phd students meeting 2018, Milan, Italy, 14th-15th June 2018.

5. Boeri L, Chierchia A, Chirico N, Raimondi MT, Tunesi M, Giordano C, Albani D. Hydrogel-embedded adipose mesenchymal stem cells for secretome controlled delivery in a Parkinson's disease in vitro model. Poster presentation at AAT-ADPD 2018, Turin, Italy, 15th - 18th March 2018.
6. Boeri L, Jacchetti E, Negro A, Albani D, Raimondi MT. Fluorescence live detection of protein nuclear import in mesenchymal stem cells adhering to the "nichoid" nanoengineered culture substrate. TERMIS European Chapter Meeting 2017, Davos, Switzerland, 26th - 30th June 2017. (**Oral presentation**)
7. Boeri L, Chierchia A, Chirico N, Raimondi MT, Giordano C, Forloni G, Albani D. Secretome released from adipose mesenchymal stem cells protects SH-SY5Y cells from oxidative stress and increases sirtuin 3 expression. 53rd Congress AINPeNC – 43rd Congress AIRIC, Padua, Italy, 18th -20th May 2017. (**Oral presentation**)
8. Boeri L, Jacchetti E, Negro A, Albani D, Raimondi MT. Molecular approaches to develop protein fluorescent tracers for live detection of nuclear import fluxes. Nanoengineering for Mechanobiology symposium, Camogli, Italy, 26th -29th March 2017. (**Oral presentation**)
9. Boeri L, Tunesi M, Giordano C, Albani D, and Raimondi MT. Engineered in vitro model to assess the neuroprotective effect of mesenchymal stem cell secretome on SH-SY5Y neuroblastoma cells exposed to 6-hydroxydopamine. TERMIS European Chapter Meeting 2016, Uppsala, Sweden, 28th June – 1st July 2016. (**Oral presentation**)
10. Boeri L, Tunesi M, Giordano C, Albani D, and Raimondi MT. A miniaturized in vitro 3D model to assess the neuroprotective effect of mesenchymal stromal cell secretome on neuroblastoma cells exposed to oxidative stress. Poster presentation at GNB 2016, Naples Italy, 20th -22nd June 2016.

Acknowledgements

First, I would like to thank my advisors to have guided me through this weird adventure. I thank Prof. Raimondi for having thought me to never give up and to think out of the box. I sincerely thank Diego for the continuous scientific and human support. But a particular gratitude goes to Emanuela for being an example and a stimulus to do always my best.

Besides my advisors, I would like to sincerely thank Prof. Soncini and Prof. Negro who patiently showed me tips and tricks of molecular dynamics and molecular engineering.

Thanks to my labmates of Politecnico and Mario Negri for having been amazing teams.

Last but not least, I would like to thank my husband and my family for believing in me every single day.

Thank you, you made this possible.

This project has received funding from the European Research Council (ERC) under the European Union's Horizon 2020 research and innovation program (grant agreement n° 646990 - NICHOID).